THE UNIVERSITY OF CHICAGO

PHASE TRANSITIONS AND CORRELATION IN MANY-BODY QUANTUM SYSTEMS

A DISSERTATION SUBMITTED TO
THE FACULTY OF THE DIVISION OF THE PHYSICAL SCIENCES
IN CANDIDACY FOR THE DEGREE OF
DOCTOR OF PHILOSOPHY

DEPARTMENT OF CHEMISTRY

BY
SAMUEL WARREN

CHICAGO, ILLINOIS
AUGUST 2025

Copyright © 2025 by Samuel Warren

The best laid plans o' Mice an' Men

Go oft awry

Robert Burns

TABLE OF CONTENTS

LIST OF FIGURES vi

ACKNOWLEDGMENTS x

ABSTRACT xii

1 INTRODUCTION 1
1.1 Brief Overview of Reduced Density Matrices 1
1.2 Phase Transitions 4
1.3 Mixed Fermion Boson Systems 8
1.4 Quantum Computing 11

2 QUANTUM SIMULATION OF QUANTUM PHASE TRANSITIONS USING THE CONVEX GEOMETRY OF REDUCED DENSITY MATRICES 13
2.1 Abstract 13
2.2 Introduction 14
2.2.1 Theory 16
2.2.2 Convex Hull of Ground-State Set of 2-RDMs 19
2.3 Results 22
2.4 Discussion and Conclusions 27
2.5 Methodology 28
2.5.1 Circuit Details 28
2.5.2 RDM Reconstruction 31

3 QUANTUM PHASE TRANSITIONS IN A MODEL HAMILTONIAN EXHIBITING ENTANGLED SIMULTANEOUS FERMION-PAIR AND EXCITON CONDENSATIONS 33
3.1 Abstract 33
3.2 Introduction 34
3.3 Theory 36
3.3.1 RDM Signatures of Condensation 36
3.3.2 Fermion-Exciton Condensate Hamiltonian 37
3.3.3 Geometry of the Set of 2-RDMs 38
3.4 Results 39
3.4.1 Finite Particle 40
3.4.2 Thermodynamic Limit 47
3.5 Discussion and Conclusions 49
3.6 Appendices 50
3.6.1 Appendix A 50

4 TOPOLOGICAL PHASE TRANSITIONS CAPTURED IN THE SET OF REDUCED DENSITY MATRICES 53
4.1 Abstract 53
4.2 Introduction 53
4.3 Theory 55
4.4 Results 59
4.4.1 SSH Model 61
4.4.2 Kitaev Chain 64
4.5 Discussion and Conclusions 69

5 EXACT ANSATZ OF FERMION-BOSON SYSTEMS FOR A QUANTUM DEVICE 71
5.1 Abstract 71
5.2 Introduction 71
5.3 Theory 73
5.4 Results 79
5.5 Conclusions 81

6 QUANTUM ALGORITHM FOR POLARITONIC CHEMISTRY BASED ON AN EXACT ANSATZ 82
6.1 Abstract 82
6.2 Introduction 82
6.3 Theory 84
6.3.1 Contracted Schrödinger Equation 84
6.3.2 Pauli-Fierz Hamiltonian 86
6.3.3 Pauli-Fierz Contracted Quantum Eigensolver 88
6.4 Results 90
6.5 Conclusions 96

LIST OF FIGURES

1.1 Hartree-Fock Slater determinate with example single and double excitations . . 2

1.2 Ising Model and its First and Second-Order Phase Transitions. The first-order phase transition occurs at T = 0, where the transverse field, h, is modified causing a sudden change in the magnetization $\langle M \rangle$ (average direction of spins on lattice sites). The second occurs at some finite h while the temperature is increased. The parameter J describes the nearest neighbor interaction that energetically rewards aligned neighboring spins. 5

1.3 H_4 in an optical cavity 8

2.1 The Convex Hull of the 2-RDMs of the 1000-Particle Lipkin Model. The cyan and green coloring distinguish the 2 ruled surfaces of the convex set, which contain lines parallel to the $\langle \hat{J}_z \rangle$ and $\langle \hat{J}_+^2 + \hat{J}_-^2 \rangle$ axes respectively. The line, traced by the black points, that separates the two ruled surfaces contains the set of ground-state 2-RDMs. These points are projected into the $\langle \hat{J}_z \rangle$-$\langle \hat{J}_+^2 + \hat{J}_-^2 \rangle$ plane as represented by a series of blue dots. 18

2.2 Symmetry Breaking of the $\langle \hat{J}_z \rangle$ Order Parameter in the 1000-Particle Lipkin Model. The black and grey lines show the change in $\langle \hat{J}_z \rangle$, in atomic units, as λ is changed for systems with a positive and negative value of ϵ, respectively. . . . 19

2.3 Symmetry Breaking of the $\langle \hat{J}_+^2 + \hat{J}_-^2 \rangle$ axis in the 1000-Particle Lipkin Model. The black and grey lines show the change in $\langle \hat{J}_+^2 + \hat{J}_-^2 \rangle$, in atomic units, as ϵ is changed for systems with a positive and negative value of λ, respectively. 20

2.4 The 2-RDM for the 1000-Particle Lipkin Model. The black line shows the extremal or ground state values of the 2-RDM set. The black and grey circles show the trajectory of the 2-RDM along the boundary of the set as λ is brought from infinity to zero with ϵ either being greater, for black, or less, for grey, than zero. All axes are in atomic units. 20

2.5 The Convex Hull of the 3-Particle Lipkin Model 2-RDMs. The black line outlines the edges of the exact set of 2-RDMs, while the inner shape is the convex hull of the QC results. A projection of the QC results is shown by a blue scatter plot. The cyan and green coloring distinguish the 2 ruled surfaces of the convex set. The lines along the green surface connect points of constant λ with $\pm\epsilon$ with the distance between lines decreasing for greater values of λ. Experimental results were obtained from ibmq_quito quantum computers [97] using the circuit found in Fig. 2.11. All axes are in atomic units. 23

2.6 Comparison of Experimental 2-RDMs with Exact for 3 qubits. Experimental results were obtained from ibmq_quito quantum computer [97]. λ, $\langle \hat{J}_z \rangle$, $\langle \hat{J}_+^2 + \hat{J}_-^2 \rangle$ are in reference to Eq. 2.4. All axes are in atomic units. 23

2.7 Gradient of $\langle \hat{J}_z \rangle$ for Lipkin Model on 3-Qubit Circuit. Grey shading shows one standard deviation from the average of ten experimental measurements of 2**13 shots. These results were obtained from the circuit in Fig. 2.11 on the imbq_quito quantum computer [97]. λ and $\langle \hat{J}_z \rangle$ are in reference to Eq. 2.4 and plotted in atomic units. 24

2.8 The convex hull of the 4 Particle Lipkin Model 2-RDMs. The black line outlines the edges of the exact set of 2-RDMs, while the inner shape is the convex hull of the QC results. A projection of the QC results is shown by a blue scatter plot. The cyan and green coloring distinguish the 2 ruled surfaces of the convex set. The lines along the green surface connect points of constant λ with $\pm\epsilon$ with the distance between lines decreasing for greater values of λ. Experimental results were obtained from ibmq_quito quantum computers [97] using the circuit found in Fig. 2.12. All axes are in atomic units. 26
2.9 Gradient of $\langle \hat{J}_z \rangle$ for Lipkin Model on 4-Qubit Circuit. Grey shading shows one standard deviation from the average of five experimental measurements 2**13 shots. These results were obtained from the ibmq_quito quantum computer [97] using the circuit found in Fig. 2.12. QASM results are from the IBM QASM simulator. λ and $\langle \hat{J}_z \rangle$ are in reference to Eq. 2.4 and plotted in atomic units. . 26
2.10 Comparison of Experimental 2-positive 2-RDMs with Exact for 4 qubits. Experimental results were obtained from ibmq_quito quantum computer [97]. λ, $\langle \hat{J}_z \rangle$, $\langle \hat{J}_+^2 + \hat{J}_-^2 \rangle$ are in reference to Eq. 2.4. All axes are plotted in atomic units. . . . 27
2.11 3-Qubit Experimental Circuit. Measurement of this circuit only provides the z-component of the qubit expectation value. The determination of the x or y components of the expectation value requires an application of the H gate or the $S^\dagger$ then H gates, respectively, immediately before the measurement step of the circuit. X is the X-gate, U is the traditional 2-D rotation matrix, the 2-qubit gates are CNOT gates, and the final gate is a measurement. 30
2.12 4-Qubit Experimental Circuit. Measurement of this circuit only provides the z-component of the qubit expectation value. The determination of the x or y components of the expectation value requires an application of the H gate or the $S^\dagger$ then H gates, respectively, immediately before the measurement step of the circuit.X is the X-gate, U is unitary rotation matrix (see supplemental), the 2-qubit gates are CNOT gates, and the final gates are measurements of the qubits. 30

3.1 Color map of Fermion-Pair and Exciton Condensation on the Convex Set of 2-RDMs. This scatter plot shows the resulting RDMs from a random sampling of Hamiltonian, Eq.3.3, configurations with a color map indicating the value of λ_G and λ_D for 3.1b and 3.1a respectively. Additionally, both plots contain the convex hull of the projections of the 3-D plot into the $\langle \hat{\lambda} \rangle$-$\langle \hat{G} \rangle$ and $\langle \hat{W} \rangle$-$\langle \hat{G} \rangle$ planes. In Figure 3.1b, α and β are marked to distinguish two regions of exciton condensation character. 40
3.2 Coalescing Trajectories from EC to FPC Regions. Figures 3.2a and 3.2b illustrate several dozen trajectories from the α, in black, and β, in grey, regions to the FPC. A light grey shape illustrates the extent of the convex hull of the set of 2-RDMs. Figures 3.2c and 3.2d show the normalized 'speed' of the points along the convex set for both groups of trajectories with respect to the altitude angle ϕ in radians. The coefficient of variance for the maximum speed attained along the trajectories is listed in the bottom left corner. 41

3.3 Speed of the α and β Trajectories. Figures 3.3a and 3.3b show the speed of a random trajectory from those plotted in Figure 3.2 for the 4 and 10 particle systems, respectively. χ is the parameter for the function describing the line between the starting and final Hamiltonians of the trajectories. 42
3.4 λ Values along Trajectories. Figures 3.4a and 3.4b contain a α, in black, and a β, in grey, trajectory for the 4 and 8 particle systems, respectively. The light grey dots are the result of a random sampling of ground-state 2-RDMs. 42
3.5 Derivatives of the Ground State Energy Along Trajectories. Figure 3.5a shows the second derivative of the ground-state energy with respect to χ, a parameter of a α line in Figure 3.3, for the 4, 8, and 12 particle systems. Figure 3.5b shows the first derivative of the ground-state energy along a β trajectory for the 4, 8, and 12 particle systems. 43
3.6 $\hat{\Lambda}$ Scattering. The upper most arrow shows a form of scattering that could be due to either the pair-force $\hat{G}$ term or the $\hat{\Lambda}$ term. While the lower arrow demonstrates how the $\hat{\Lambda}$ scattering is able to entangle states with large contributions to the maximal eigenstates of $\hat{W}$ with states that have large contributions to the maximal eigenstates of the pair-force term. 44

4.1 RDM acceleration through a topological phase transition in the SSH model. The acceleration is calculated using Eq. (4.1), and is divided by the system size for normalization. The results are for the ground-state RDM for a system that is tuned from [v,w]: [-2,-1]→[2,-1] (see Eq. 4.7) passing through 2 phase transitions at v=±1 60
4.2 Structural changes in the 1-RDM near topological phase transition in the SSH Hamiltonian. Subplots (a)-(c) show the matrix elements of the 1-RDMs for a 10 site system in the trivial ($100v = w$), gapless ($v = w$), and topological phases ($v = 100w$), respectively, where each matrix element is given by $\langle \hat{a}_i^\dagger \hat{a}_j \rangle$. 60
4.3 Change in the Pearson Correlation Coefficient near topological phase transitions in the SSH Hamiltonian. The Hamiltonian is tuned from [v,w]: [-2,-1]→[2,-1] (see Eq. (4.7)) passing through two phase transitions at v=±1. 61
4.4 Signatures of topological phase transitions in the structure of the 1-RDM and the 2-Particle Cumulant in the Kitaev Chain Model. Subplot (a) shows the change in the structure of the 1-RDM as it is taken through a topological phase transition at $\mu = 2$ (to emphasize the shift of population to the edges, the color scale of the RDM element is logarithmic in base 10), and subplot (b) shows how this change is reflected in the PCC. Subplot (c) shows the changes in the structure of the eigenvector of the largest eigenvalue of the 2-particle cumulant (LCE) (see Eq.(4.17)), and Subplot (d) shows the PCC of the LCE as the system is taken through the same phase transitions. All of the plots have $[\omega, \beta] = [-1, -1]$ (see Eq.(4.15)) 65
4.5 Changes in the Largest Cumulant Eigenvalue near topological phase transitions in the Kitaev Chain. The legend depicts the size of the system for 8-18 site systems as the Hamiltonian is tuned from $[\mu, \omega, \beta]$: [-4,-1,-1]→[4,-1,-1] (see Eq. (4.15)) . 66

4.6 Slice of the Convex Set of the ground-state RDMs of the Kitaev Chain Model. For this 1000 site system, the coloring of this figure is split around the grey dashed line, where the upper-half is a binary coloring with gray or black indicating that a point lies in the trivial or topological regimes respectively. In the lower-half, the coloring corresponds to the color bar to the right and depicts the value of the PCC (see Eq. (4.5)) at any point. $\langle\hat{\omega}\rangle$ and $\langle\hat{\mu}\rangle$ refer to the expectation value of Hamiltonian terms found in Eq. (4.15) 67

5.1 CSE and QED-CCSD energies for the 3 fermion Tavis-Cummings model with increasing coupling. The Hamiltonian parameters from Eq. (5.14) were fixed as $(\omega_b, \omega_f) = (2, 0.5)$ while g_c is varied as shown along the x-axis. The QED-CCSD-n methods are named according to the convention used in Ref. [51]. 78
5.2 CSE and QED-CCSD predicted ground fermionic orbital populations with increasing coupling in the 3-fermion Tavis-Cummings Model. 78
5.3 CQE and QED-CCSD ground-state energy and fermionic orbital population with increasing coupling. The y-axis of the energy shows the absolute error in mHartree. 79

6.1 Comparison of energies from QED-CC and the ACSE in the deformation of rectangular H_4 coupled to a cavity mode. $R_0 = 1.23$ Å refers to the length of the constant x-axis of H_4, while R is the variable z-axis length. λ refers to the coupling strength in the Pauli-Fierz Hamiltonian oriented along the z-axis. The embedded figures show the gradients of the potential energy surfaces produced by the ACSE and CC near the cusp. The level of theory for each method is ACSE-1, QED-CCSD-1, and QED-FCI-1. 91
6.2 HONO and LUNO orbital occupations from QED-CC and the ACSE in the deformation of H_4 coupled to a cavity mode. $R_0 = 1.23$ Å refers to the length of the constant x-axis of H_4, while R is the variable z-axis length. λ refers to the coupling strength in the Pauli-Fierz Hamiltonian oriented along the z-axis. The level of theory for each method is ACSE-1, QED-CCSD-1, and QED-FCI-1. . . 92
6.3 Dissociation Curve of H_2 coupled to a bosonic bath on an IBM Quantum Device. The coupling strength was set to $\lambda = .2$. Measurement was preformed on `ibm_cleveland` using 4096 shot per circuit. The level of theory for each method is ACSE-1 and QED-FCI-1. 93

ACKNOWLEDGMENTS

I am very grateful to the dozens of people who have made this thesis research possible throughout the years either directly through support in my research, through emotional support, or through physically supporting me from falling off a cliff. First, I would like to thank David Mazziotti, my thesis adviser, for guiding me through a vast array of research topics and helping shape me as a researcher. Similar praise goes to my first grad student mentor, LeeAnn Sager-Smith, who helped me get my sea legs so to speak. Danny Gibney is another mentor in the group, but also a good friend and fellow e-waste scavenger. Our conversations have helped guide my professional and personal interests, and while long and often during the workday, I think they have probably been a net positive for my research. Yuchen Wang has also been an immensely helpful colleague and friend, and I have greatly valued our time both discussing research and playing Go (although I believe we still have tied record to settle). Anna Schouten is another extremely valuable colleague, whose knowledge of periodic methods greatly accelerated my own research into the topic. Our conversations over lunch over the past 5 years have kept me sane. I would like to thank Irma Avdic for her critical eye and her invaluable help in numerous presentations and posters over the years and Luis Delgado Granados for his humor and for introducing me to so many interesting topics (JOJO!). Lily has been a god-send for helping me with MMT and also a hilarious friend in the group, although I think she might need to distance herself from some bad influences (cough cough Kaitlyn). Serina has been a great officemate, and has been extremely patient with Danny and my constant yammering. I have already seen her grow so much as a scientist and am excited to see her future work! I am also grateful to Michael Rose for his stimulating conversation, and contagious passion for research. I would also like to shout out Noah for teaching me that not everyone who goes to Ole' Miss is terrible ;). A final and enormous thanks goes to Carlos Riveros-Benavides for a very productive collaboration.

I would also like to thank all of my friends in the department, and my second adopted

group the Engel Group! Caitlin Bellora for not dropping me and listening to my ravings, Coco (Beiye) Li for her kindness, humor and great taste, Indranil Ghosh for making me feel like a real scientist and a fake diplomat, Joey Spellberg for stimulating conversation and helping me pass first year, Spencer Guo for his support and help with MMT and teaching me that coffee doesn't have to taste like burnt cigarettes, Olivia Wedig for making me feel bad about my climbing and Kaitlyn Feuling for teaching me how to deadlift. Jeri Beiter for bellyaches from both laughter and too much food, Kyle Beiter for humanizing finance bros, Julie Korsmeyer for introducing me to soup dumplings and taking care of the pigs, and Jesus Alvarez for convincing me to go to UChicago in the first place. To all of my friends back home, Sam, Gus, Avery, Alex, Daniel, and Aaron thanks for reminding me that I'm still an idiot and that I probably should have been an HVAC technician...

Finally, I need to thank my family for so much support and love throughout my PhD. My brother Jeff and his wife Nicole for feeding and housing me during the pandemic and undertaking the impossible task of helping me dress like an adult. My amazing, funny, and of course adorable niece and nephews, Kitty Gail, Ted, and Will for lighting up my day. My other brother Cannon and his wife Charlotte for not getting mad when I copy everything they do from rock climbing to biking to making sourdough to being a bald guy with glasses (I guess this last one is just Cannon). My parents for unconditional love and unlimited forgiveness, making me passionate and curious, and only asking me if I remember their passwords once a year. And finally, my partner Melissa. I am so grateful for her humor, which bring me out of the darkest holes, her patient wisdom when she teaches me something new for the 15th time, her bravery when I ask her to join me on some ridiculous quest, her sense of joy when we walk through the woods, play a video-game, or watch a movie, and her willingness to listen (or at least nod her head) as I talk and talk and talk.

ABSTRACT

The often disparate fields of quantum mechanics and statistical mechanics meet at the intersection of quantum phase transitions. These transitions, just like those in classical mechanics, can be found through measures of correlation in the system. These correlation functions are the workhorses of statistical mechanics, and provide a simple means of understanding phase transitions (among many other phenomena). In electronic structure theory, on the other hand, the electron density or the many-body wave function is traditionally the fundamental quantity. These measures have their benefits. The density can be scaled agnostically to the system complexity and can, given the universal functional, produce the energy. While the wave function contains all of the information about the system at the cost of combinatorial scaling. A third possible means of describing quantum systems comes in the form of reduced density matrices (RDMs). RDMs are the 2nd-quantized form of correlation functions in quantum systems, and the 2-electron RDM (2-RDM) in particular contains all the necessary correlation information to exactly reproduce the energy of an electronic system. In this text, we will explore the benefits of looking at quantum systems through the lens of the 2-RDM. The second through fifth chapters will discuss how the 2-RDM allows for a simple visualization of quantum and topological phase transitions, while also revealing the presence of strongly correlated phenomenon such as electron-electron and electron-hole condensation. The final two chapters will then discuss how the 2-RDM and methods based around it, provide an efficient and exact means of studying mixed fermion-boson systems on quantum devices.

CHAPTER 1

INTRODUCTION

It used to be that no one could graduate with a degree in chemistry without some basic understanding of German. Without it, the most cutting-edge research of the day would be inaccessible. Luckily, in order to understand the following chapters, no foreign language experience is necessary. However, unlike most electronic structure texts that use the wave function as the fundamental unit of knowledge about quantum systems, the following sections and chapters describe quantum systems using Reduced Density Matrices (RDMs). This introduction will very briefly define RDMs and create the connection between RDMs and critical phenomena like phase transitions. Additionally, there will be an introduction to the topic of polaritonic chemistry, and electronic structure methods on quantum devices.

1.1 Brief Overview of Reduced Density Matrices

The main goal of (non-relativistic) electronic structure theory is to find approximate solutions to the electronic Schödinger equation or equivalently approximate eigenvectors/values for the electronic Hamiltonian, which is written below to emphasize the importance of the last and trickiest term, the electron-electron repulsion.

$$H = T + U_{en} + U_{nn} + \sum_{i<j} \frac{e^2}{4\pi\epsilon_0 r_{ij}} \tag{1.1}$$

where T contains the kinetic energy terms for the electrons and nuclie, U_{en} contains the electron-nuclear interactions, U_{nn} contains the nuclear-nuclear interactions, and in the last term r_{ij} is the electron-electron distance along with the electronic charge e and the vacuum permittivity ϵ_0. The kinetic energy is easily treated as it is a one-body term, and the other two two-body interaction terms are reduced to one-body complexity once the Born-Oppenheimer approximation is made (i.e. the nuclei are assumed stationary). Aside from

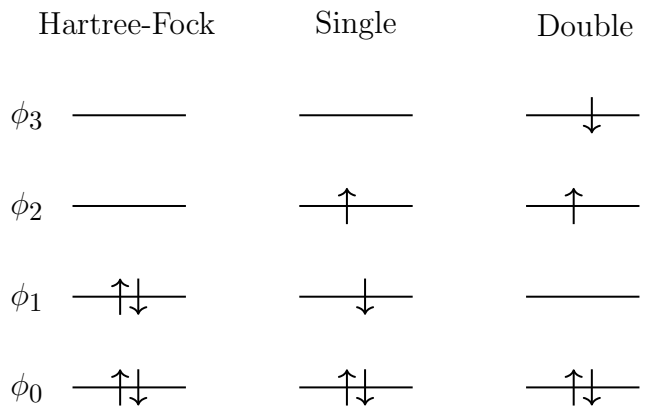

Figure 1.1: Hartree-Fock Slater determinate with example single and double excitations

hydrogenic atoms, the electron-electron repulsion term makes exactly solving for the eigenstates impossible. This can be addressed by approximating the electron-electron repulsion term by a mean-field potential. In this approximation, each individual electron is affected by a potential derived from the other electrons. The wave function will then be a product of single-particle solutions, with the additional constraint that the overall wave function should be anti-symmetric with respect to swapping particles due to the fermionic statistics of electrons. These wave functions, or Slater determinants [1] can be written as

$$|\Psi\rangle = \det \begin{vmatrix} \phi_1(1) & \phi_1(2) & .. \\ \phi_2(1) & \phi_2(2) & .. \\ : & : & \end{vmatrix} \tag{1.2}$$

where $\phi_i(n)$ describes the nth electron in the ith orbital (single-particle solution to the mean-field problem). This can be written more succinctly in second quantization as

$$= a_1^\dagger \wedge a_2^\dagger \wedge ... \, |0\rangle \tag{1.3}$$

where $\wedge$ is the Grassmann wedge product [2, 3] or the exterior product defined where $c_i \wedge d_j = -d_j \wedge c_i$, and $a_i^\dagger / a_i$ are the fermionic creation/annihilation operators for the ith orbital acting

on the vacuum state, $|0\rangle$. Solutions of this form can then be solved self-consistently (the solution can modify the mean-field potential, which in turn can result in a new solution) to find an approximation to the lowest-energy state. More formally, the Hartree-Fock ground (lowest-energy) state (seen in Figure 1.1) can be calculated by self-consistently solving the Hartree equations [4, 5, 1, 6].

However, Hartree-Fock by design ignores electron-electron correlation, which is incredibly important for a vast array of physical phenomena from superconductivity [7, 8, 9, 10, 11, 12] to photosynthesis [13, 14]. The Hartree-Fock wave function can be improved by adding more Slater determinants (these determinants can be formed by exciting electrons as shown in Figure 1.1) and variationally optimizing the linear combination, but this wave function scales combinatorially with the number of orbitals and electrons. Instead, a more compact object containing all of the information in the quantum system can be derived by returning to the Schrödinger equation written in second quantization

$$H = \sum_{ijkl} {}^2K^{i,j}_{k,l}\, {}^2\Gamma^{i,j}_{k,l} = \sum_{ijkl} {}^2K^{i,j}_{k,l} a^\dagger_i a^\dagger_j a_l a_k. \tag{1.4}$$

where ${}^2K$ is the two-electron Hamiltonian tensor and ${}^2\Gamma$ is the antisymmetric two-electron operator, which is defined in terms of creation and annihiliation operators on the right-hand side. The energy of the ground state can be found by acting on both sides of the equation with the ground state wave function $|\Psi_0\rangle$

$$\langle H\rangle = E_0 = \sum_{ijkl} {}^2K^{i,j}_{k,l} \langle\Psi_0|\, \hat{a}^\dagger_i \hat{a}^\dagger_j \hat{a}_l \hat{a}_k\, |\Psi_0\rangle = \sum_{ijkl} {}^2K^{i,j}_{k,l}\, {}^2D^{ij}_{kl} \tag{1.5}$$

where ${}^2D$ is the ground state 2-electron RDM. The 2-RDM, which scales as r^4 (where r is the number of orbitals), contains all of the two-body information in a system and was proven to uniquely map back to the wave function [15, 3]. This principle, that the minimal RDM

necessary that uniquely maps back to the ground state wavefunction is equal to the highest N-body interaction in the Hamiltonian, can be generalized for more complicated systems as discussed in later chapters.

The 2-RDM, unlike the wave function, cannot be naively variationally optimized due to the problem of N-Representability [16, 17, 18] or whether the 2-RDM can be derived from an N-particle wavefunction, but several methods have been developed which are able to produce approximations to the ground state 2-RDM such as the Variational 2-RDM method [19] and the Anti-hermitian Contracted Schrödinger Equation (ACSE) method [20, 21] and are able to capture correlation in electronic systems. The ACSE has also been extended to quantum computing, which will be discussed at length later in this text. However, the focus of the next section will be on how the 2-RDM provides a compact container of correlation information.

1.2 Phase Transitions

Phase transitions are an enormous area of research that covers topics ranging from the self-assembly of proteins [22, 23, 24] to insulator-to-metal transitions [25, 26] to collective decision making problems in social systems [27]. This breadth hints at one of the most amazing facts of phase transitions, which is their independence from system details, or in other words their universality. For example, when water boils into a vapor, its behavior is nearly indistinguishable from boiling liquid nitrogen despite the massive difference in intermolecular attractions between the materials. Perhaps an even starker example is the Ising Model (see Figure 1.2), a theoretical spin lattice, which when swapping the direction of an external field also acts like a boiling liquid. This universality allowed early scientists to predict the behavior of systems without any concept of their underlying complexity. But what is this universal "behavior"?

There are any number of observables in a system such as magnetism, viscosity, or conduc-

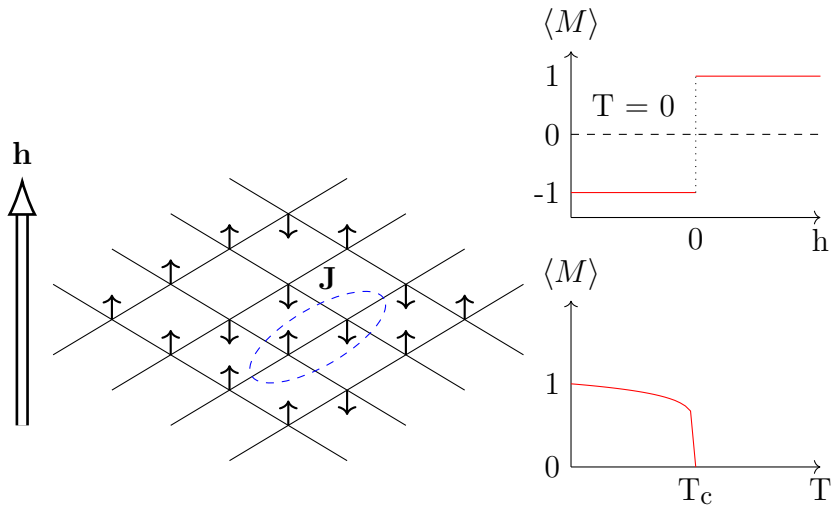

Figure 1.2: Ising Model and its First and Second-Order Phase Transitions. The first-order phase transition occurs at T = 0, where the transverse field, h, is modified causing a sudden change in the magnetization $\langle M \rangle$ (average direction of spins on lattice sites). The second occurs at some finite h while the temperature is increased. The parameter J describes the nearest neighbor interaction that energetically rewards aligned neighboring spins.

tivity, and these properties often change with temperature, such as the resistance of metals. These changes are normally smooth and can be written as some polynomial with respect to temperature. However, near a phase transition, the order parameter (resistance in the metal as an example) of the material changes to some other polynomial. This change can be discontinuous, such as the density of water as it melts or boils, or it can be continuous but have some discontinuity in the derivative. An example of this would be the magnetism of the 2-D Ising model with temperature (see Figure 1.2). Phase transitions can be classified by what order of discontinuity is observed, with the caveat that the order parameter is a 1st-derivative of the free energy of the system (meaning the water to vapor transition is a 1st-order phase transition). This explains why multiple observables may become discontinuous, because they are all derivatives in the direction of some discontinuity in the free energy surface [28].

This can be made a little more concrete with some equations and will pay dividends when

connecting phase transitions to RDMs. Suppose some order parameter x_1 is discontinuous across a phase transition (this would correspond to a first-order phase transition). The expected value of x_1 is written as

$$\langle x_1 \rangle = \frac{1}{Z} \int_{x_1, x_2, \ldots} x_1 e^{-\beta E(x_1, x_2, \ldots)} \tag{1.6}$$

where Z is the partition function $Z = \int_{x_1, x_2, \ldots} e^{-\beta E(x_1, x_2, ..)}$ (this is all in the canonical ensemble and may be missing a few constants). Imagining our Hamiltonian has a simple relationship to x_1 like $H = H(x_{i \neq 1}) + \lambda x_1$, we can rewrite the above equation as

$$\langle x_1 \rangle = \frac{-1}{\beta} \frac{\partial}{\partial \lambda} ln Z \tag{1.7}$$

This shows the location of the first derivative in a first-order phase transition. Taking the second derivative for a second-order transition

$$\langle x_1^2 \rangle - \langle x_1 \rangle^2 = \langle (\Delta x_1)^2 \rangle = \frac{\partial^2}{\partial (\beta \lambda)^2} \ln Z \tag{1.8}$$

reveals the variance of x_1. We can now clearly see the form of the higher order phase transitions and can make a connection between this and the statistical concept of a cumulant generating function

$$\Delta_i = \frac{\partial^i}{\partial t^i} \ln e^{tX} \tag{1.9}$$

where X is some random variable. These functions are incredibly important in statistics for quantitatively and uniquely describing probability distributions.

Quantum phase transitions (QPTs) diverge from their classical counter-parts, but not very far [29]. In a classical system, phase transitions arise due to competition between thermal fluctuations and the general propensity of nature to minimize the energy. Quantum phase transitions on the other hand occur at 0K, so there are no thermal fluctuations.

Instead 'quantum' fluctuations compete with energy to cause QPTs. The identification of these QPTs can also be done using order parameters. This analysis is simplified greatly due to the low temperature

$$\langle x_1 \rangle = \frac{\sum_i \langle i| \, x_1 \, |i\rangle \, e^{-\beta E_i}}{\sum_i e^{-\beta E_i}} = \frac{\langle 0| \, x_1 \, |0\rangle \, e^{-\beta E_0}}{e^{-\beta E_0}} = \langle 0| \, x_1 \, |0\rangle \tag{1.10}$$

which eliminates any contributions except from the ground state to the expectation value. Therefore, perhaps unsurprisingly, a first-order QPT should appear as a discontinuity in the ground state expectation value of some observable. The previously derived cumulant generating definition of phase transition order indicates that a second-order QPT will appear in the ground state variance of that observable.

Take a simple example, such as the spin (magnetization) of some quantum system

$$\langle m \rangle = \sum_i \langle a^\dagger_{i\alpha} a_{i\alpha} \rangle - \langle a^\dagger_{i\beta} a_{i\beta} \rangle = \mathrm{Tr}({}^1D^\alpha_\alpha) - \mathrm{Tr}({}^1D^\beta_\beta) \tag{1.11}$$

It is clear that a discontinuity in this order parameter would appear as a discontinuity in the set of 1-RDMs. However, if the QPT was second-order, a discontinuity should exist in the variance, which requires some slightly tedious fermionic algebra to arrive at

$$\langle (\Delta m)^2 \rangle = \sum_{\alpha,\alpha',\beta,\beta'} \left[{}^2D^{\alpha,\alpha'}_{\alpha,\alpha'} - {}^1D^\alpha_\alpha \, {}^1D^{\alpha'}_{\alpha'} \right] + \left[{}^2D^{\beta,\beta'}_{\beta,\beta'} - {}^1D^\beta_\beta \, {}^1D^{\beta'}_{\beta'} \right] \tag{1.12}$$

$$- 2 \left[{}^2D^{\alpha,\beta}_{\alpha,\beta} - {}^1D^\alpha_\alpha \, {}^1D^\beta_\beta \right] + {}^1D^\alpha_\alpha + {}^1D^\beta_\beta. \tag{1.13}$$

Having defined the QPT to be second order, the final two terms dealing only with the 1-RDM must be continuous, therefore the discontinuity must arise in the terms in square brackets.

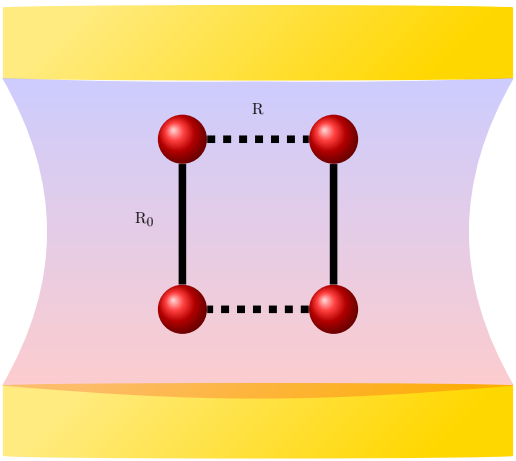

Figure 1.3: H_4 in an optical cavity

These terms are the 2-electron cumulants while the 1-RDM is the 1-electron cumulant [30]

$$\langle(\Delta m)^2\rangle = \sum_{\alpha,\alpha',\beta,\beta'} {}^2\Delta^{\alpha,\alpha'}_{\alpha,\alpha'} + {}^2\Delta^{\beta,\beta'}_{\beta,\beta'} - 2\,{}^2\Delta^{\alpha,\beta}_{\alpha,\beta} + {}^1\Delta^{\alpha}_{\alpha} + {}^1\Delta^{\beta}_{\beta}. \tag{1.14}$$

The 2-electron cumulant contains the correlation information for electronic systems (exactly the information that is left out by Hartree Fock) and has been shown to be an indicator of a vast array of correlated phenonmenon such as superconductivity [31, 9]. This demonstrates a basic principle, which is that higher-order phase transitions will manifest in higher-order cumulants. The first three chapters of this text will explore the ways in which different phase transitions, including topological transitions, which fall outside of the scheme discussed above, can be detected within the set of RDMs for a system.

1.3 Mixed Fermion Boson Systems

As discussed in the prior section, quantum phase transitions occur due to changes in external conditions, excluding temperature. One such condition could be light. These light-matter coupled systems present an interesting problem for traditional electronic structure methods due to the fact that light (a boson) obeys fundamentally different statistics from an electron

(a fermion). Generally, light is treated more as a time-dependent phenomena for pumping populations of electrons into excited states [32, 33], which has proven useful for studying light harvesting [34] or some light-initiated reaction mechanisms [35]. This can work rather well, but begins to break down in the strongly coupled limit where light can begin to modify spectra of the system. In this limit, electron-photon quasi-particles, known as polaritons [36], begin to form and can drastically change the energetic landscape of a system [37]. This has extremely interesting applications in synthesis, where different reaction pathways can be preferentially selected by modifying the photon-vacuum cavity[38].

One of the simplest examples of this light-matter coupling can be found in the Jaynes-Cummings model [39]. This model couples a single two-level fermionic system with a single bosonic mode like an idealized laser cavity

$$\hat{H} = \omega_f(\hat{a}_+^\dagger \hat{a}_+) + \omega_b(\hat{b}^\dagger \hat{b}) + g_c(\hat{a}_+^\dagger \hat{a}_- \hat{b} + \hat{a}_-^\dagger \hat{a}_+ \hat{b}^\dagger) \tag{1.15}$$

where $b^\dagger/b$ are the bosonic creation/annihilation operators, $+/-$ subscripts distinguish the excited and ground levels of the fermionic system, and $\omega_f/\omega_b/g_c$ are unitless parameters describing the strength of each term. This equation can then be broken down into a first term which gives the fermionic energy gap, a second term which gives the oscillator strength of the bosonic system (a quantum harmonic oscillator), and a final term which couples the two by exchanging excitations. The eigenenergies of this system can be written as

$$E_\pm = \omega_b(n + \frac{1}{2}) \pm \sqrt{\omega_f^2 + g_c^2(n+1)} \tag{1.16}$$

where the fermion-boson coupling, g_c, can modify the excited-state energies, demonstrating how strong light-matter interactions could be used to influence chemical dynamics by modifying potential energy surfaces. Chapter 5 discusses the Tavis-Cummings model [40, 41], which extends the Jaynes-Cummings model by considering multiple fermionic systems

coupled to a bosonic mode. This more closely resembles a ensemble of molecules inside of a cavity and brings the theory closer to something useful for polaritonic chemistry.

Clearly, however, in order to study real molecules in a cavity a new Hamiltonian needs to be derived. In Chapter 6 the Pauli-Fierz (PF) Hamiltonian [42, 43], is presented, which allows for both modeling actual chemical systems and increasing the allowed coupling strength

$$\hat{H}_{\mathrm{PF}} = \hat{H}_e + \omega \hat{b}^\dagger \hat{b} - \sqrt{\frac{\omega}{2}} \left(\vec{\lambda} \cdot \hat{\mu} \right) (\hat{b}^\dagger + \hat{b}) + \frac{1}{2} \left(\vec{\lambda} \cdot \hat{\mu} \right)^2 , \tag{1.17}$$

Where H_e is the electronic Hamiltonian found in Eq. 1.4, ω is the bosonic oscillator fundamental frequency, and $\mu/\vec{\lambda}$ are the dipole moment and dipole coupling vectors respectively. This means that the third term is the coupling of the molecular dipole to the cavity field, and the final term is the dipole self-energy. Excellent derivations of the PF Hamiltonian can be found in Refs. [44, 45], and a more in depth discussion of the various terms can be found in Chapter 6. The ground states of this Hamiltonian, unlike the Cummings models, cannot be found analytically due to the inclusion of the electronic Hamiltonain. In order to find these states, many methods from traditional electronic structure theory have been adapted for treating mixed boson-fermion systems. The basis of most of these methods, much like the traditional methods discussed in the first section of this chapter, is quantum electrodynamics (QED) Hartree Fock [46, 43, 47, 48, 49, 50]. The HF state can be written as

$$|\mathrm{QEDHF}\rangle = \sum_n c_n (b^\dagger)^n \otimes |\mathrm{HF}\rangle \, . \tag{1.18}$$

where c_n is the nth coefficient in the sum. Following the spirit of the traditional HF SCF procedure, this state can be calculated by first integrating out the bosonic contributions to the Hamiltonian, resulting in a new external mean-field potential, and then solving the now biased normal SCF procedure. This is then followed by integrating out the electronic degrees of freedom and exactly solving (with some truncation in the Fock space) the remaining

bosonic Hamiltonian under the effective electronic mean-field potential. This cycle can be done iteratively until a self-consistent solution is reached. This, however, like many self-consistent methods, can have difficulty converging to the solution. To overcome this, it can be shown that the bosonic portion of the QED-HF ground state can be exactly written as a coherent state

$$|0\rangle_{cs} = e^{z(\hat{b}^\dagger - \hat{b})} |0\rangle . \tag{1.19}$$

where $\hat{b} |n\rangle_{cs} = n$. This reduces the PF Hamiltonian, after integrating out $|0\rangle_{cs}$ on both sides of the equation, to

$$\hat{H}_{\mathrm{PF}} = \hat{H}_e + \frac{1}{2} \left(\lambda \cdot (\hat{\mu} - \langle \hat{\mu} \rangle)\right)^2 , \tag{1.20}$$

This can then be solved within the normal SCF Hartree Fock procedure. Building upon the QED-HF ground state, methods such as QED-Coupled Cluster [51, 52] or QED-V2RDM [53] have been used to study polaritonic systems. More details on these *ab initio* methods and the coherent state transformation of the PF Hamiltonian can be found in Ref. [44]. Chapters 5 and 6 discuss the development of quantum computing algorithms for studying the more general class of mixed boson-fermion systems.

1.4 Quantum Computing

Quantum computing presents a new paradigm for a huge class of problems considered intractable with classical computation. However, despite major advances in quantum computing hardware, noise and a dirth of qubits still poses a significant issue for many of the most promising algorithms like Grover's search [54] or Shor's factorization [55]. Electronic structure problems on the other hand seem to be the perfect place for noisy intermediate scale quantum (NISQ) devices with only hundreds of qubits [56, 57, 58, 59].

One of the more popular methods for solving electronic structure problems on a quantum device is the variational quantum eigensolver [60]. This class of methods, based on the

variational principle from quantum mechanics, attempts to minimize the energy of the wave function by measuring observables of the wave function on the quantum devices and constructing new gate sequences using an optimizer on a classical computer. The wave function is constructed using some anzatz like unitary coupled cluster [61], which while excellent for many systems, is unable to treat strong correlation [62, 63, 52, 64].

Chapters 5 and 6 of this work extend a different class of algorithms known as the contracted quantum eigensolvers [65, 66, 67, 68]. These algorithms minimize the wave function with respect to the 2-body residual of the Hamiltonian, which can be directly measured on the quantum device. The CQE is able to solve strongly correlated problems exactly and has demonstrated strong resistance to noise on quantum devices.

CHAPTER 2

QUANTUM SIMULATION OF QUANTUM PHASE TRANSITIONS USING THE CONVEX GEOMETRY OF REDUCED DENSITY MATRICES

Republished with permission from Samuel Warren, LeeAnn M. Sager-Smith, and David A. Mazziotti. *Physical Review A.* **106**, 1, 012434. Copyright American Physical Society 2022.

2.1 Abstract

Transitions of many-particle quantum systems between distinct phases at absolute-zero temperature, known as quantum phase transitions, require an exacting treatment of particle correlations. In this work, we present a general quantum-computing approach to quantum phase transitions that exploits the geometric structure of reduced density matrices. While typical approaches to quantum phase transitions examine discontinuities in the order parameters, the origin of phase transitions—their order parameters and symmetry breaking—can be understood geometrically in terms of the set of two-particle reduced density matrices (2-RDMs). The convex set of 2-RDMs provides a comprehensive map of the quantum system including its distinct phases as well as the transitions connecting these phases. Because 2-RDMs can potentially be computed on quantum computers at non-exponential cost, even when the quantum system is strongly correlated, they are ideally suited for a quantum-computing approach to quantum phase transitions. We compute the convex set of 2-RDMs for a Lipkin-Meshkov-Glick spin model on IBM superconducting-qubit quantum processors. Even though computations are limited to few-particle models due to device noise, comparisons with a classically solvable 1000-particle model reveal that the finite-particle quantum solutions capture the key features of the phase transitions including the strong correlation and the symmetry breaking.

2.2 Introduction

Phase transitions such as the melting of ice arise from thermal fluctuations [28]. Even at absolute zero in the absence of thermal fluctuations, transitions between phases, known as quantum phase transitions (QPTs), can occur from quantum fluctuations arising from the uncertainty relations [29, 69, 70]. Importantly, these quantum fluctuations and their associated phase transitions are significant for a range of temperatures beginning at absolute zero. An understanding of these transitions is critical to addressing outstanding problems in the study of magnetic insulators [71, 72, 73], electron gases [74, 75, 76, 77], heavy-fermion compounds [78, 79, 80], and high temperature superconductors [81, 82, 83, 84, 85, 86, 87]. Experimental realizations of QPTs often involve laser traps of individual atoms and ions [88, 89, 90, 91, 92, 93], or the synthesis of exotic materials [94, 95, 96] requiring significant investment in experimental setups and synthesis techniques. The advent of cloud-accessible quantum computing devices [97], which allow for a significant degree of control over the preparation of an experimental quantum system, provides a promising new avenue for the exploration of highly correlated systems [98, 99, 100, 101] and QPTs [102].

In this work, we present a novel quantum-computing approach to quantum phase transitions that exploits the geometric structure of two-particle reduced density matrices (2-RDMs). Traditional approaches to QPTs are typically framed in terms of the many-particle wave functions of ground and excited states [29, 69, 70], which are readily prepared on hybrid quantum-classical computers but not easily measured in their entirety due to their exponential scaling with the number of particles. Quantum computers allow us to directly probe the polynomially scaling 2-RDM by tomography [103] without classical storage of the exponentially scaling many-particle wave function [104, 100, 103], which potentially enables the treatment of significantly larger systems. A 2-RDM-based analysis for QPTs on quantum computers could enable the study of QPTs for larger system sizes than either classical 2-RDM methods [105, 106, 107, 108] or wave-function-based modeling on quantum devices.

Traditional wave function analysis of QPTs relies on finding discontinuities in the ground-state energy, but this method can miss important system symmetries. A complementary analysis based on 2-RDMs developed by Erdahl and Jin [105] and Gidofalvi and Mazziotti [106, 107] characterizes QPTs in terms of the geometric set of 2-RDMs, particularly the movement of the ground-state 2-RDM between different phases. Separate work, inspired by the link between bipartite entanglement and QPTs, found that changes in individual elements of the 2-RDM set can also indicate critical phenomenon [109]. Additional work in this field by Zauner and Verstraete [108] found that a geometric analysis of the ground-state set of 2-RDMs provides a powerful visualization of symmetry breaking and phase transitions in both classical and quantum systems, which hearkens back to the geometric approach developed by Gibbs and Maxwell by generalizing Maxwell's eponymous surface to spin systems.

In contrast to the traditional description of phase transitions, 2-RDM theory provides a generalizable geometric framework for quantum phase transitions in terms of the convex set of 2-RDMs that has two important advantages: (1) based on a quantum information perspective, the 2-RDM theory relies upon the state space of all two-body observables rather than a specific Hamiltonian to examine the transition, and (2) it reduces the analysis of an infinite space of Hamiltonians to the study of recognizable features like planes or ruled surfaces in the finite and convex set of 2-RDMs. Such a three-dimensional analysis allows for visualizing a greater swath of the space of all possible Hamiltonians than traditional single-order-parameter or energy-level analysis. While sharing many of the same observables as the conventional analysis, the geometric perspective in a reduced state space creates a powerful, general framework for studying and understanding quantum criticality.

Using the Lipkin-Meshkov-Glick (LMG) spin model [110], we show that even with Noisy Intermediate-Scale Quantum (NISQ) devices [111], the signature features of the quantum phase transition are captured from the measured set of 2-RDMs. LMG is a widely used bench marking system for many-body approximation methods [112, 113, 114] and has been

extensively studied for its phase behavior [115, 116, 117, 106, 118, 119]. Using the unitary transformations available to a quantum computer, a simulated finite-particle LMG system is manipulated through several critical regions. Tomography of the system is used to determine the ground-state set of 2-RDMs [100, 120, 104, 103], which reveals discontinuities in the system's order parameters. Additionally, the geometry of the ground-state set provides evidence of symmetry breaking on the NISQ devices [106, 121].

2.2.1 Theory

The Reduced Density Matrix

RDM mechanics is an alternative to the wave function mechanics traditionally used in quantum molecular studies [19, 122]. Because the fundamental interactions in electronic systems are pairwise, the energies and properties of such systems are computable from a knowledge of the 2-RDM. The 1- and 2-RDMs are obtained by integrating the density matrix, $|\psi\rangle\langle\psi|$, over $N-1$ or $N-2$ particles where the elements of the 1- and 2-RDMs are given in the second-quantization formalism by

$$^1D^i_j = \langle\psi|\,\hat{a}^\dagger_i\hat{a}_j\,|\psi\rangle \tag{2.1}$$

$$^2D^{ij}_{kl} = \langle\psi|\,\hat{a}^\dagger_i\hat{a}^\dagger_j\hat{a}_l\hat{a}_k\,|\psi\rangle \tag{2.2}$$

in which $\hat{a}_i$ and $\hat{a}^\dagger_i$ are the fermionic annihilation and creation operators for the spin-orbital i. These pairs of operators can be expressed as strings of Pauli matrices, which are directly measurable on the quantum computer [100]. The resulting 2-RDMs, according to Rosina's theorem, completely characterize the ground-state energy and order parameters of a system with only pairwise interactions [123, 124], circumventing the need for a full wave-function description of the system, which could require significantly more measurements on a NISQ device [125] increasing error and computational time. Discontinuities in the individual order

parameters obtained from the 2-RDM as the system's Hamiltonian is manipulated, can be used to find critical points [106, 121].

Three-dimensional graphical analysis of the set of 2-RDMs allows for the identification and classification of the system's critical points, as well as direct observation of symmetry breaking. Additionally, as these graphs are 3-D slices of the total RDM set, their construction only requires a subset of 2-RDM elements, potentially allowing for a further pruning of necessary measurements. In the thermodynamic limit, first-order QPTs appear as planes or discontinuities in the extremal or ground-state values of the 2-RDM, which can be identified with no knowledge of the Hamiltonian of the system. In systems with more than three degrees of freedom within the RDM, maximizing the size of these discontinuous regions, by changing which 3D slice is taken, will indicate the order parameter with maximum symmetry breaking, and provides a systematic way to discover symmetry breaking in a system [108]. Second-order QPTs manifest as regions where the extremal values of the 2-RDM set change rapidly with changes in the Hamiltonian parameters or the curvature becomes discontinuous [106, 108]. To solidify these concepts, we analyze the LMG system through the lens of RDM mechanics.

The Lipkin-Meshkov-Glick Model

The Lipkin-Meshkov-Glick (LMG) model system consists of two energy levels separated by ϵ each containing N-degenerate states. There are N fermions in the system, with a coupling parameter, λ, that scatters pairs of particles between the levels. A configuration of the system is characterized by two quantum numbers: $\sigma = \pm 1$ indicating the energy level and $p = \{0, ..., N\}$ specifying the state within that level [110]. In the second quantization formalism, the LMG Hamiltonian is:

$$\hat{H} = \frac{1}{2}\epsilon \sum_{p\sigma} \sigma \hat{a}^{\dagger}_{p\sigma}\hat{a}_{p\sigma} + \frac{1}{2}\lambda \sum_{pp'\sigma} \hat{a}^{\dagger}_{p\sigma}\hat{a}^{\dagger}_{p'\sigma}\hat{a}_{p'-\sigma}\hat{a}_{p-\sigma}. \tag{2.3}$$

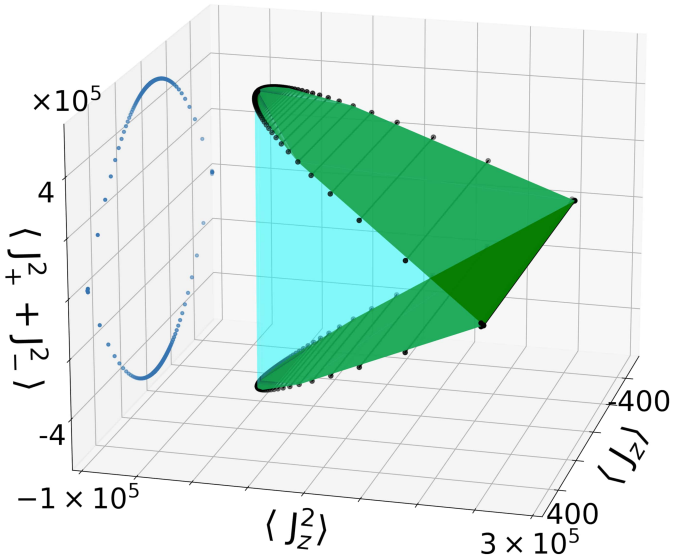

Figure 2.1: The Convex Hull of the 2-RDMs of the 1000-Particle Lipkin Model. The cyan and green coloring distinguish the 2 ruled surfaces of the convex set, which contain lines parallel to the $\langle \hat{J}_z \rangle$ and $\langle \hat{J}_+^2 + \hat{J}_-^2 \rangle$ axes respectively. The line, traced by the black points, that separates the two ruled surfaces contains the set of ground-state 2-RDMs. These points are projected into the $\langle \hat{J}_z \rangle$-$\langle \hat{J}_+^2 + \hat{J}_-^2 \rangle$ plane as represented by a series of blue dots.
The lines along the green surface, show the steps of a trajectory along the edges of the set as λ is taken from infinity to zero while $\epsilon = \pm 1$. All axes are in atomic units.

In order to solve for the LMG eigenstates exactly, it is helpful to reduce the degrees of freedom of the problem through incorporation of the system's symmetries into the Hamiltonian through a quasi-spin formalism. This formalism recognizes that the LMG two-level system is analogous to a system comprised of N two-spin-state particles, with a Hamiltonian:

$$\hat{H} = \epsilon \hat{J}_z + \frac{1}{2}\lambda(\hat{J}_+^2 + \hat{J}_-^2) \tag{2.4}$$

using the traditional spin operators

$$\hat{J}_+ = \sum_p \hat{a}_{p,+1}^\dagger \hat{a}_{p,-1}, \qquad \hat{J}_- = \sum_p \hat{a}_{p,-1}^\dagger \hat{a}_{p,+1},$$

and

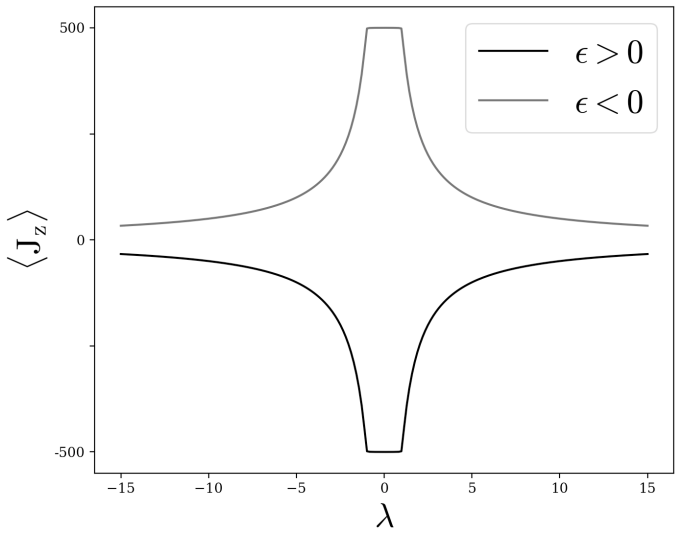

Figure 2.2: Symmetry Breaking of the $\langle \hat{J}_z \rangle$ Order Parameter in the 1000-Particle Lipkin Model. The black and grey lines show the change in $\langle \hat{J}_z \rangle$, in atomic units, as λ is changed for systems with a positive and negative value of ϵ, respectively.

$$\hat{J}_z = \frac{1}{2} \sum_{p\sigma} \sigma \hat{a}^\dagger_{p\sigma} \hat{a}_{p\sigma} \tag{2.5}$$

In this quasi-spin formalism, p and σ indicate the particle and the Z-component of its spin, respectively. Writing the Hamiltonian in the $|j, j_z\rangle$ basis, reveals a block diagonal matrix, which can be diagonalized at a much lower computational cost than the original $2^N \times 2^N$ matrix [110]. The 2-RDM for the LMG system in this formalism is completely defined by the three expectation values $\langle \hat{J}_z \rangle$, $\langle \hat{J}^2_z \rangle$, $\langle \hat{J}^2_+ + \hat{J}^2_- \rangle$ [126]. Therefore the extremal points of this set can be visualized in a space defined by these parameters.

2.2.2 Convex Hull of Ground-State Set of 2-RDMs

The convex hull of the ground-state set of 2-RDMs for the 1000-particle LMG system can be seen in Fig. 2.1, which was obtained through the exact diagonalization of the Hamiltonian. This representation gives geometric insight into both general properties of the 2-RDM and more specific properties of the LMG system, and serves as a reference in the geometric

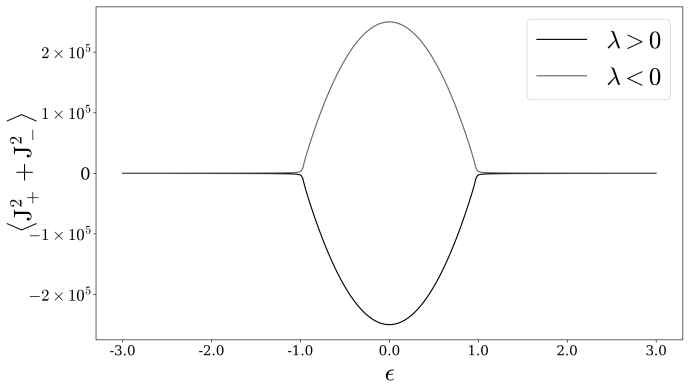

Figure 2.3: Symmetry Breaking of the $\langle \hat{J}^2_+ + \hat{J}^2_- \rangle$ axis in the 1000-Particle Lipkin Model. The black and grey lines show the change in $\langle \hat{J}^2_+ + \hat{J}^2_- \rangle$, in atomic units, as ϵ is changed for systems with a positive and negative value of λ, respectively.

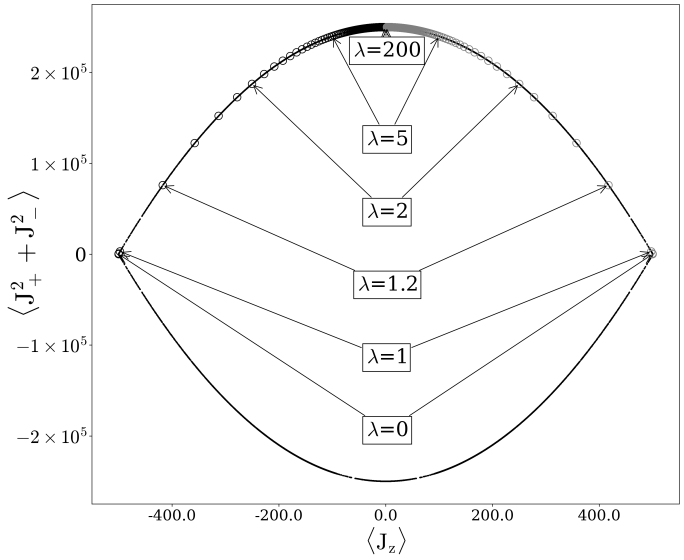

Figure 2.4: The 2-RDM for the 1000-Particle Lipkin Model. The black line shows the extremal or ground state values of the 2-RDM set. The black and grey circles show the trajectory of the 2-RDM along the boundary of the set as λ is brought from infinity to zero with ϵ either being greater, for black, or less, for grey, than zero. All axes are in atomic units.

analysis of noisier results from simulations of the LMG system on NISQ devices. The ground-state 2-RDMs lie on the boundary of the convex set while excited-state 2-RDMs generally lie inside the convex set. This plot also reveals the existence of two ruled surfaces, colored green and blue, indicating two forms of symmetry breaking in the system. Points along the lines of the ruled surfaces are ground states of the Hamiltonian with all of the same order parameters except for the parameter with an axis parallel to the lines. This indicates that there is symmetry breaking in the system [108]. The green surface has lines parallel to the $\langle \hat{J}_z \rangle$ axis, which for $\epsilon \neq 0$ indicates a breaking of the spin flip symmetry of the ground state in regions with small λ [127]. This manifests as the ground state preferring either an all up or all down spin configuration based on the value of ϵ. Figure 2.2 captures this symmetry breaking by demonstrating how the order parameter $\langle \hat{J}_z \rangle$ changes with λ for systems with positive and negative values of ϵ. These systems are identical for large λ values, but as ϵ becomes a more significant contribution to the Hamiltonian, a symmetry-breaking divergence occurs between the two systems. The blue surface with lines parallel to the $\langle \hat{J}_+^2 + \hat{J}_-^2 \rangle$ indicates another symmetry breaking, where the ground state has either a positive or negative eigenvalue for $\langle \hat{J}_+^2 + \hat{J}_-^2 \rangle$. This eigenvalue reflects the parity of the ground-state wave function. Figure 2.3 shows the divergence of the positive and negative λ symmetry invariant systems as the Hamiltonian is tuned from an ϵ- to a λ-dominated region at $\epsilon \approx 1$. Figures 2.2 and 2.3 also both contain sharp changes in the curvature at $\lambda, \epsilon \approx 1$. These sharp changes or discontinuities in the derivatives of the order parameters are signs of a second-order QPT. Signatures of these QPTs can also be found in the set of 2-RDMs.

The hull plot, Fig. 2.1, contains a projection of the 2-RDM into the $\langle \hat{J}_z \rangle$ - $\langle \hat{J}_+^2 + \hat{J}_-^2 \rangle$ plane, which is seen in more detail in Fig. 2.4. This 2D representation contains two trajectories of 2-RDMs as λ is taken from $\infty \rightarrow 0$ for positive and negative values of ϵ. The plot demonstrates that the systems start from the same symmetry invariant 2-RDM at $\lambda = \infty$, but diverge radically for infinitesimally small positive and negative values of ϵ. This graph

also shows the presence of a second-order phase transition around $\lambda = 1$. From $\lambda = 0 \rightarrow 1$ the 2-RDM barely changes, but suddenly after $\lambda = 1$ the 2-RDM begins to move very rapidly along the boundary of the set, before decelerating again near the apex of the curve. This "acceleration" of the 2-RDM is characteristic of a second-order phase transition [106, 108]. For finite-particle LMG systems, this acceleration is not as rapid as it is for the system in the thermodynamic limit, where the speed of the 2-RDM diverges, but a finite signature of this QPT is still present [128, 119, 106].

The quasi-spin formalism for the LMG system can be mapped onto the two-state qubit system of a quantum computer (QC), where the traditional computational basis is $|\uparrow\rangle = |0\rangle$ and $|\downarrow\rangle = |1\rangle$ [129]. Therefore each quasi-particle in the LMG system or equivalently each pair of pth states is represented by a qubit on the QC. Quantum computers also offer the ability to generate arbitrary interactions between particles including the two spin flip interaction of the LMG system (Circuit Details can be found in Appendix 2.5.1). Measurement of the 2-RDM can then be used to identify the presence of a QPT through the methods previously discussed.

2.3 Results

Evidence of a QPT on a quantum computer is obtained from a 3-qubit simulation of the LMG system by measuring elements of the system's ground state 2-RDMs. The system is simulated by the circuit in Appendix Fig. 2.11 for $\epsilon = \pm 1$ and $\lambda \in$ [-25,25]. The experimentally gathered convex hull for this system can be seen in Fig. 2.5, with the exact results outlining a larger, but similar hull. This contraction is typical in quantum computing experiments [104] due to systematic errors like qubit crosstalk, T1 and T2 relaxation times, and gate errors. Specifically, T1 errors greatly contribute to the contraction of the set. T1 error or bit flipping populates states with lower $\langle J_z^2 \rangle$ values as those states are mixed spin. $\langle \hat{J}_+^2 + \hat{J}_-^2 \rangle = \langle J_x^2 - J_y^2 \rangle$ values suffer from this same error. Measurement of $\langle J_{x/y}^2 \rangle$ requires

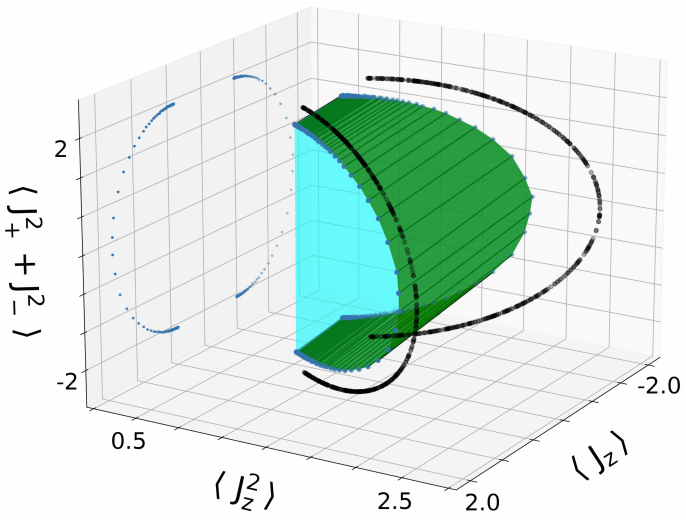

Figure 2.5: The Convex Hull of the 3-Particle Lipkin Model 2-RDMs. The black line outlines the edges of the exact set of 2-RDMs, while the inner shape is the convex hull of the QC results. A projection of the QC results is shown by a blue scatter plot. The cyan and green coloring distinguish the 2 ruled surfaces of the convex set. The lines along the green surface connect points of constant λ with $\pm\epsilon$ with the distance between lines decreasing for greater values of λ. Experimental results were obtained from ibmq_quito quantum computers [97] using the circuit found in Fig. 2.11. All axes are in atomic units.

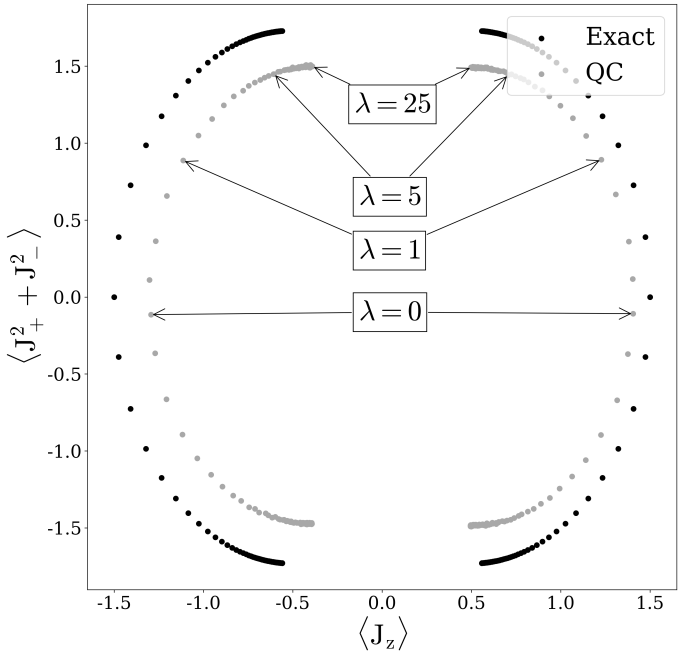

Figure 2.6: Comparison of Experimental 2-RDMs with Exact for 3 qubits. Experimental results were obtained from ibmq_quito quantum computer [97]. λ, $\langle \hat{J}_z \rangle$, $\langle \hat{J}_+^2 + \hat{J}_-^2 \rangle$ are in reference to Eq. 2.4. All axes are in atomic units.

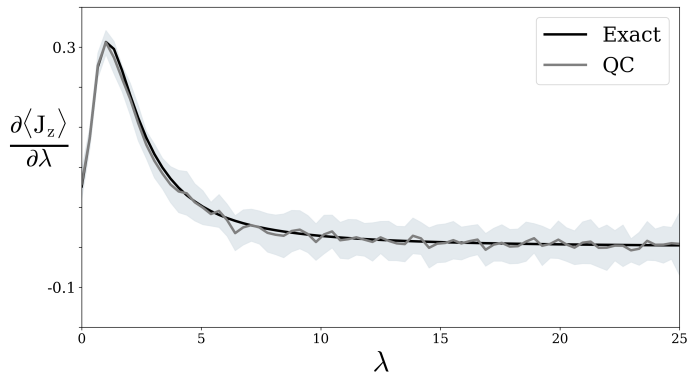

Figure 2.7: Gradient of $\langle \hat{J}_z \rangle$ for Lipkin Model on 3-Qubit Circuit. Grey shading shows one standard deviation from the average of ten experimental measurements of 2**13 shots. These results were obtained from the circuit in Fig. 2.11 on the imbq_quito quantum computer [97]. λ and $\langle \hat{J}_z \rangle$ are in reference to Eq. 2.4 and plotted in atomic units.

a rotation of the X or the Y component of the spin to the Z-axis (see Appendix B for details on measurement of the RDM), thus T1 relaxation populating mixed spin states will also decrease $\langle J^2_{x/y} \rangle$. Simulations on ideal quantum computers, which only include random noise, indicate that as systematic errors are decreased this contraction will also subside (additional analysis of the contraction of the set on multiple NISQ devices can be found in the SI). The hull, Fig. 2.5, shows many of the interesting features that were present in the infinite dimensional case, Fig. 2.1, including the two ruled surfaces that indicate symmetry breaking in the system without any reference to the underlying Hamiltonian. However, in this figure a new plane parallel to the $\langle \hat{J}_z \rangle$ - $\langle \hat{J}^2_+ + \hat{J}^2_- \rangle$ plane appears due to the finite size and odd number of particles in the system. The 4 vertices of this plane are degenerate 2-RDMs corresponding to the limits $(\epsilon, \lambda) \to [(0^+, > 0), (0^+, < 0), (0^-, > 0), (0^-, < 0)]$) which are all within the disordered phase of the Lipkin Model. This discontinuity in the order parameters between these degenerate states tells of a actual level and an avoided-level crossing as ϵ and λ, respectively, flip signs.

The plot contains lines of constant λ, which become more tightly spaced as λ goes to infinity, which suggests the presence of a finite signature of a second-order QPT. This signature can be seen in Figs. 2.6 and 2.7. Figure 2.6 demonstrates acceleration of the ground-state 2-

RDMs along the boundary of the convex set of 2-RDMs between the aligned and disordered spin regions [106]. Despite the contraction of the set in this Figure, the change in $\langle J_z \rangle$ with respect to λ is nearly identical to the exact results as seen in Fig. 2.7 showing the finite-particle signature of a second-order QPT. Note that due to the smaller particle number, the sudden acceleration at small values of λ is less pronounced than in the thermodynamic limit shown in Fig. 2.4, but the deceleration for large values of λ is the same.

The convex hull of the 4-qubit 2-RDM can be seen in Fig. 2.8. This hull differs immediately from the 3-qubit hull as it lacks the plane indicative of a first-order QPT due to the even number of qubits in the system. The lines along the hull illustrating the movement of 2-RDMs as λ is increased also appear to no longer be parallel with each other or the $\langle \hat{J}_z \rangle$ axis. This asymmetry is reflected in the 2D projection which can be seen more clearly in Fig. 2.10. The asymmetry across the $\langle J_z \rangle$ axis arises primarily due to T1 relaxation. T1 relaxation to the ground state of the qubit, $|0\rangle$, results in a shift towards larger $\langle J_z \rangle$ values due to mapping of the quasi-spin formalism to the qubits as discussed in the theory section. T1 relaxation also explains why the effect is less drastic in the 3-qubit results, as shorter circuits are less prone to this form of decoherence. This shift has an even more dramatic effect on the $\langle J_z^2 \rangle$ values as seen in Figure 2.8. The exact results in the Figure demonstrate the approach to a symmetry-invariant 2-RDM as $\lambda \to \infty$, something lacking in the 3-qubit case. The experimental results are slightly offset from one another but still seem to approach a symmetry invariant 2-RDM. The characteristic acceleration and deceleration of the 2-RDMs is also apparent in the Figure. This behavior is confirmed in Figure 2.9, where the data qualitatively matches the exact results peaking at $\lambda = 1$, indicating the finite-particle signature of a phase transition in the system.

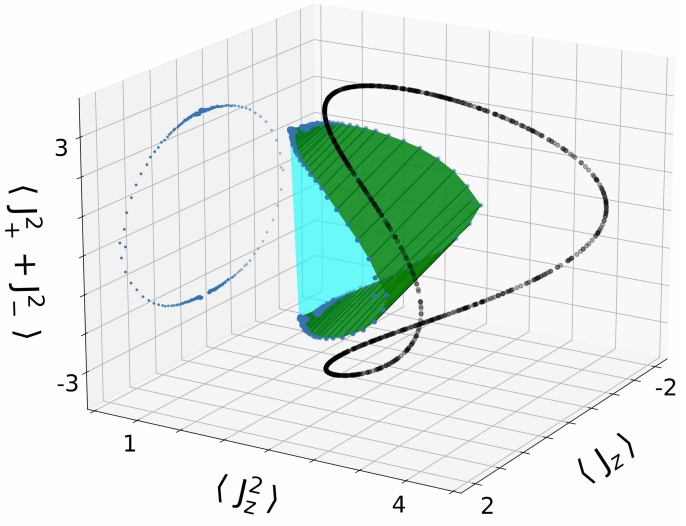

Figure 2.8: The convex hull of the 4 Particle Lipkin Model 2-RDMs. The black line outlines the edges of the exact set of 2-RDMs, while the inner shape is the convex hull of the QC results. A projection of the QC results is shown by a blue scatter plot. The cyan and green coloring distinguish the 2 ruled surfaces of the convex set. The lines along the green surface connect points of constant λ with $\pm\epsilon$ with the distance between lines decreasing for greater values of λ. Experimental results were obtained from ibmq_quito quantum computers [97] using the circuit found in Fig. 2.12. All axes are in atomic units.

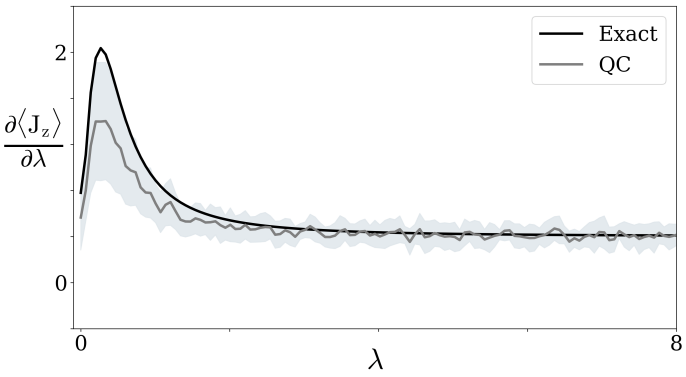

Figure 2.9: Gradient of $\langle \hat{J}_z \rangle$ for Lipkin Model on 4-Qubit Circuit. Grey shading shows one standard deviation from the average of five experimental measurements 2**13 shots. These results were obtained from the ibmq_quito quantum computer [97] using the circuit found in Fig. 2.12. QASM results are from the IBM QASM simulator. λ and $\langle \hat{J}_z \rangle$ are in reference to Eq. 2.4 and plotted in atomic units.

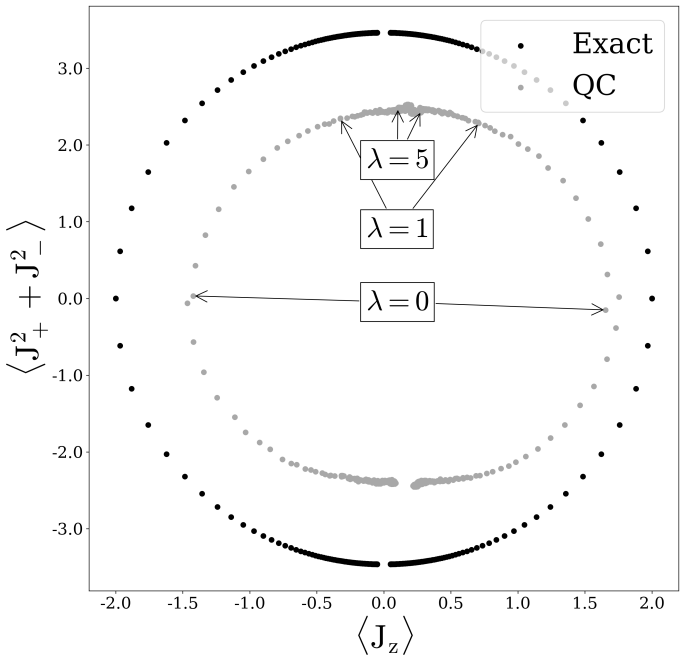

Figure 2.10: Comparison of Experimental 2-positive 2-RDMs with Exact for 4 qubits. Experimental results were obtained from ibmq_quito quantum computer [97]. λ, $\langle \hat{J}_z \rangle$, $\langle \hat{J}^2_+ + \hat{J}^2_- \rangle$ are in reference to Eq. 2.4. All axes are plotted in atomic units.

2.4 Discussion and Conclusions

Wave-function-based methods typically characterize QPTs by showing discontinuities in the energy surface, but can miss important symmetries of the system as well as require a prohibitively large number of measurements on a noisy quantum device increasing both computational time and error. In contrast, 2-RDM analysis takes advantage of the pairwise nature of interactions to decrease the number of measurements on a quantum computer necessary to describe a QPT, and utilizes the geometry of the convex set to demonstrate symmetry breaking in the system without any reference to the underlying Hamiltonian. Here we demonstrate the 2-RDM approach to QPTs on NISQ simulators and devices by computing the finite-particle signatures of the QPT in the Lipkin model.

When the scattering potential is increased in the Lipkin model, taking the system from an ordered to disordered region, the ground-state 2-RDM rapidly accelerates along the boundary of the set in the critical region. Because the 2-RDM contains information for all of

the one- and two-body operators, its movement along the boundary of the set reflects the change in order parameters of the ground state, providing signatures of a QPT. Therefore, measurements showing discontinuities in this movement allow for recovery of critical behavior without any reference to the wave function [106]. The Lipkin model, shown for the 3- and 4-particle systems, has ruled surfaces on the convex hull of the set of ground-state 2-RDMs, where the lines along these ruled surfaces connect degenerate states with different values of an order parameter reflecting symmetry breaking [108].

While the Lipkin model has exact solutions, the methodology outlined could be combined with quantum eigensolvers, in particular the variational quantum eigensolver (VQE) or the contracted quantum eigensolver (CQE) for resolving ground-state 2-RDMs [65], to arrive at solutions for systems where the exact ground states are unknown from classical computations. NISQ devices with around 50 qubits would be able to explore systems that are well beyond the exactly solvable limit of classical devices and would strain many approximate methods. Studying real systems, like potential candidates for superconductors or exciton condensates, would be possible with VQE or CQE which are able to effectively capture long-range order due to their basis in 2-RDM theory, and being quantum chemical methods they are easily transferable to different models. These results underscore the advantages of 2-RDM analysis on NISQ devices by demonstrating the reduced tomography costs relative to wave function methods and by utilizing the geometry of the ground-state set of 2-RDMs to resolve both symmetry breaking and phase transitions in the LMG model.

2.5 Methodology

2.5.1 Circuit Details

The circuits developed in this article are for the 3- and 4-particle LMG systems where the $\sigma = \pm 1$ LMG pair of spin orbitals, p (see Eq 2.4), are represented by the $|0\rangle$ and $|1\rangle$ states of

the pth qubit respectively. The experimental expectation values result from averaging 5×2^{14} and 5×2^{13} measurements of each relevant Pauli strings (see Appendix B) on the quantum devices for the 3 and 4-qubit circuits respectively. The circuit for the 3-qubit system can be found in Fig. 2.11. The first step is to rotate the state vector from the $|000\rangle$ configuration to the $|111\rangle$ or all down "spin" configuration using X-gates (following the computer science tradition in naming $|0\rangle$ the excited state) [129]. The following unitary and CNOT gates rotate the $|111\rangle$ state into

$$\alpha_1 |001\rangle + \alpha_2 |010\rangle + \alpha_3 |100\rangle + \beta |111\rangle . \tag{2.6}$$

where each coefficient is a function of the rotation angles of the unitary gates. By solving the Hamiltonian exactly, the ground-state coefficients are known, so it is possible to solve a system of equations for the rotation angles. With the correct selection of rotations for the U-gates, the resulting state is the lowest energy eigenvector of the Lipkin Hamiltonian with coefficients dependent on the parameter λ.

The 4-qubit circuit, Fig. 2.12, is constructed similarly to the 3-qubit circuit, with an initial rotation to an all "down spin" state, and a series of rotations to the lowest energy eigenstate:

$$\alpha |0000\rangle + \beta(|0011\rangle + |0101\rangle + |1001\rangle + |1010\rangle + |1100\rangle) + \gamma |1111\rangle \tag{2.7}$$

These circuits were developed with the goals of minimizing the number of CNOT gates, which are the largest sources of error in quantum computations, and satisfying the connectivity of the IBM computers ibmq_belem, and imbq_quito running on the Falcon r4T processor [97]. Unlike an ideal QC, these systems can only perform CNOT gates between a subset of their qubits. CNOT gates that are not native to the machine can be decomposed into native CNOT gates, but this process can add a significant number of extra 2-qubit gates, which

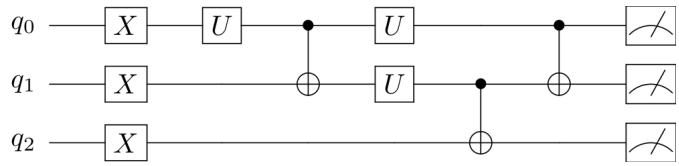

Figure 2.11: 3-Qubit Experimental Circuit. Measurement of this circuit only provides the z-component of the qubit expectation value. The determination of the x or y components of the expectation value requires an application of the H gate or the $S^\dagger$ then H gates, respectively, immediately before the measurement step of the circuit. X is the X-gate, U is the traditional 2-D rotation matrix, the 2-qubit gates are CNOT gates, and the final gate is a measurement.

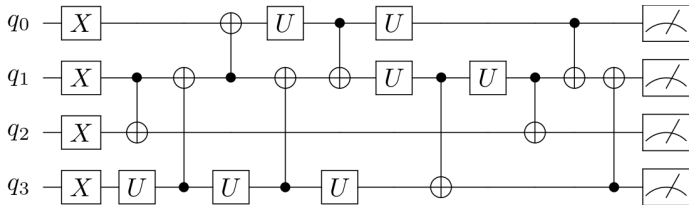

Figure 2.12: 4-Qubit Experimental Circuit. Measurement of this circuit only provides the z-component of the qubit expectation value. The determination of the x or y components of the expectation value requires an application of the H gate or the $S^\dagger$ then H gates, respectively, immediately before the measurement step of the circuit.X is the X-gate, U is unitary rotation matrix (see supplemental), the 2-qubit gates are CNOT gates, and the final gates are measurements of the qubits.

increases noise and hence the error of the results.

The unitary circuit referenced in Figs. 2.11 and 2.12, can be decomposed into the basis gates:

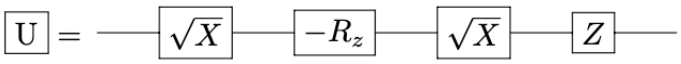

In matrix notation

$$\sqrt{X} = \frac{1}{2}\begin{bmatrix} 1+i & 1-i \\ 1-i & 1+i \end{bmatrix} \tag{2.8}$$

$$-R_Z(\theta) = R_z(\theta+\pi) = \begin{bmatrix} 1 & 0 \\ 0 & e^{\theta+\pi} \end{bmatrix} \tag{2.9}$$

$$Z = R_z(3\pi) = \begin{bmatrix} 1 & 0 \\ 0 & -1 \end{bmatrix} \tag{2.10}$$

The resulting unitary matrix has the property that

$$U^\dagger M U = R^\dagger M R \tag{2.11}$$

where

$$R = \begin{bmatrix} \cos\theta/2 & -\sin\theta/2 \\ \sin\theta/2 & \cos\theta/2 \end{bmatrix} \tag{2.12}$$

which is the classic two-dimensional rotation matrix and M is any arbitrary matrix.

2.5.2 RDM Reconstruction

The energy expectation value of the Lipkin system can be written as a function of the 1- and 2-RDMs as

$$\langle \hat{H} \rangle = \frac{1}{2}\epsilon \sum_{p\sigma} \sigma \ {}^1D_p^p + \frac{1}{2}\lambda \sum_{pq} \ {}^2D_{pq}^{pq} \tag{2.13}$$

These elements can be constructed from linear combinations of expectation values of at most pairs of Pauli strings [100] as seen below:

$${}^1D_p^p = \langle \sigma_{zp} \rangle \tag{2.14}$$

$${}^2D_{pq}^{pq} = \langle \sigma_{xp}\sigma_{xq} \rangle - \langle \sigma_{yp}\sigma_{yq} \rangle \tag{2.15}$$

Figures 2.11 and 2.12 illustrate how to determine the expectation values for z-Pauli strings, but the reconstruction of the RDM requires measurement of any combination of Pauli strings. Measuring the x and y component of a specific qubit can be accomplished by inserting a Hadamard or the adjoint phase gate ($S^\dagger$) then a Hadamard gate, respectively,

before collapsing the wave function through measurement. This allows for the measurement of any combination of pairs of expectation values.

CHAPTER 3

QUANTUM PHASE TRANSITIONS IN A MODEL HAMILTONIAN EXHIBITING ENTANGLED SIMULTANEOUS FERMION-PAIR AND EXCITON CONDENSATIONS

Republished with permission from Samuel Warren, LeeAnn M. Sager-Smith, and David A. Mazziotti. *Physical Review B.* **106**, 16, 165107. Copyright American Physical Society 2022.

3.1 Abstract

Quantum states of a novel Bose-Einstein condensate, in which both fermion-pair and exciton condensations are simultaneously present, have recently been realized theoretically in a model Hamiltonian system. Here we identify quantum phase transitions in that model between fermion-pair and exciton condensations based on a geometric analysis of the convex set of ground-state 2-particle reduced density matrices (2-RDMs). The 2-RDM set provides a finite representation of the infinite parameter space of Hamiltonians that readily reveals a fermion-pair condensate phase and two distinct exciton condensate phases, as well as the emergence of first- and second-order phase transitions as the particle number of the system is increased. The set, furthermore, shows that the fermion-exciton condensate (FEC) lies along the second-order phase transition between the exciton and fermion-pair condensate phases. The detailed information about the exciton and fermion-pair phases, the forces behind these phase, as well as their associated transitions provides additional insight into the formation of the FEC condensate, which we anticipate will prove useful in its experimental realization.

3.2 Introduction

Condensation phenomena were some of the first macroscopic-quantum effects observed in the modern physics era with the discovery of superconductivity in mercury [130] and helium-4's superfluidity[131] in the early 1900's. These exotic phases of matter continue to dominate research in fields concerned with the development of breakthrough technologies like high-temperature superconductors [132, 133, 134, 135], superconducting [136, 137] and topological [138, 139, 140] qubits, and excitonic-superconducting materials [141, 142, 143, 144]. Additionally, these efforts have lead to the creation of new theories regarding quantum phase transitions [29] and novel model Hamiltonians in order to explore these exotic forms of matter on a simplified manifold.

Recent work by Sager and Mazziotti [145] has demonstrated the existence of simultaneous exciton and fermion-fermion pair condensation or Fermion-Exciton Condensation (FEC) in a model Hamiltonian. This was achieved by combining two other model Hamiltonians that demonstrate condensation and long range off-diagonal order. The first, the Bardeen-Schrieffer-Cooper (BCS) Hamiltonian [146], was created with the express purpose of modeling, the hitherto unexplained, fermion-fermion pair condensation, earning them a Nobel prize in 1972. The second model, the Lipkin-Meleshkov-Glick (LMG) Hamiltonian [110, 147, 148], was originally constructed with the goal of testing quantum-many body approximations on an exactly solvable, but highly correlated system, and has been extensively studied for its phase transitions [119, 117, 106, 149, 150]. For the purposes of the FEC Hamiltonian, it has been observed that many of the LMG ground-states have significant exciton condensation character [100]. The model that results from combining these two systems generates states that demonstrated FEC. However, while it was demonstrated that these FEC states exist in the thermodynamic limit [10], the underlying phase behavior that gives rise to these states remains obscure.

In this work, we use quantum information techniques based on the 2-particle reduced

density matrix (2-RDM) [109, 106, 107, 108] combined with more traditional 2-RDM methods, developed to determine the condensate character of a ground-state RDM [8, 7, 151, 152, 9], to explore the FEC system. As demonstrated by Erdahl and Jin [105], Gidofalvi and Mazziotti [106], and Zauner and Verstraete [108], a geometric analysis of the ground-state set of 2-RDMs provides a visualization of symmetry breaking and phase transitions in both classical and quantum systems, which hearkens back to the geometric approach developed by Gibbs and Maxwell by generalizing Maxwell eponymous surface to discrete systems. This method provides a generalizable geometric framework for quantum phase transitions in terms of the convex set of 2-RDMS that has two important advantages: (1) based on a quantum information perspective, the 2-RDM theory relies upon the state space of all two-body observables rather than a specific Hamiltonian to examine the transition, and (2) it reduces the analysis of an infinite space of Hamiltonians to the study of recognizable geometric features like planes or ruled surfaces in the finite and convex set of 2-RDMs. Such a three-dimensional analysis allows for visualizing a greater swath of the space of all possible Hamiltonians than traditional single-order parameter or energy-level analysis. As a result, this higher level prospective can guide focused studies with these more traditional techniques to regions with interesting critical behavior.

Here, through exactly solving the system Hamiltonian for finite systems, we are able to determine various phases of exciton and fermion-fermion pair condensation, as well as identify the emergence of phase transitions with growing particle number. These phase transitions prove particularly interesting as the FEC states are found to lie in these critical regions, and they provide evidence that long range off-diagonal coupling, due to scattering, generates and can even suppress simultaneous condensation. This analysis supplies a perspective, which may aid in finding real-world systems that exhibit simultaneous condensation, and exploit their potential in energy transport and electronics.

3.3 Theory

We cover the signatures or signs of condensation in Reduced Density Matrix theory in section 3.3.1, then provide a description of the Fermion-Exciton Condensate Hamiltonian in section 3.3.2, and finally, identify the geometric consequences on the convex set of ground-state 2-RDMs of quantum phase transitions in section 3.3.3.

3.3.1 RDM Signatures of Condensation

Fermion-pair condensation—superconductivity being a prominent example—is the result of multiple quasi-bosonic fermion-fermion pairs occupying a single two-fermion function, known as a geminal, which is analogous to the single-fermion occupation of an orbital [146, 153, 154]. Such condensation results in the frictionless flow, superfluidity, of these particle-particle pairs through the material [8, 155, 156]. In the case of Cooper (electron-electron) pairs [146], superfluidity manifests as superconductivity, which has a vast set of potential applications including in energy transport [133] or in the nascent field of quantum computing [136, 137].

In order to verify the presence and extent of fermion-fermion pair condensation, Yang [8] and Sasaki [7] independently developed a computation signature derived from the particle-particle reduced density matrix (RDM), ${}^2D$, whose elements are described by

$$ {}^2D^{i,j}_{k,l} = \langle \Psi | \, a_i^\dagger a_j^\dagger a_l a_k \, | \Psi \rangle \tag{3.1} $$

where $a_i^\dagger$ and a_i are the fermionic creation and annihilation operators for the ith orbital acting on the N-fermion wave function $|\Psi\rangle$. Eigenvalues of the ${}^2D$ matrix describe the occupation of the two-fermion geminals [151, 31], meaning that when one of these eigenvalues exceeds the Pauli-like limit of one, multiple fermion-fermion pairs occupy a single geminal and hence fermion-pair condensation occurs. More generally, measurement of the largest eigenvalue, λ_D, serves as a indicator of off-diagonal long-range order in a system [31].

Similarly, exciton condensation occurs when multiple fermion-hole pairs begin to occupy the same particle-hole function, resulting in the superfluidity of the quasi-bosonic particle-hole pairs [141, 142]. The computational signature of this condensation is the second largest eigenvalue of the particle-hole RDM or the G matrix [9] where the largest eigenvalue is the ground-state-to-ground-state transition. This transition can be removed using the one-fermion RDM, ${}^1D$:

$$ {}^2\tilde{G}^{i,j}_{k,l} = {}^2G^{i,j}_{k,l} - {}^1D^i_j \, {}^1D^l_k = \langle\Psi| a^\dagger_i a_j a^\dagger_l a_k |\Psi\rangle - \langle\Psi| a^\dagger_i a_j |\Psi\rangle \langle\Psi| a^\dagger_l a_k |\Psi\rangle , \tag{3.2} $$

leaving the largest eigenvalue of the modified G matrix, which we denote as λ_G, as a signature of exciton condensation.

These signatures have been successfully used to identify condensation in a variety of systems [9, 101, 11, 143, 12], and because of the linear mapping between ${}^2D$ and ${}^2G$ [122], calculation of one type of reduced density matrix trivializes the calculation of the other one. This relationship makes it possible to easily determine if both forms of condensation exist within a single system by calculating the 2-RDM—the ${}^2D$ matrix—either exactly or through approximate methods [19, 20, 157].

3.3.2 Fermion-Exciton Condensate Hamiltonian

The Fermion-Exciton Condensate (FEC) model Hamiltonian was proposed by Sager and Mazziotti [145] as a means to produce a model capable of demonstrating exciton condensation, fermion-pair condensation (FPC), and simultaneous FEC. The Hamiltonian is constructed by combining two model systems, the Bardeen-Schrieffer-Cooper (BCS) or Pair-Force (PF)[146] and Lipkin-Meshkov-Glick (LMG) [110, 147] systems, which independently are able to achieve fermion-pair and exciton condensation, respectively. The resulting Hamil-

tonian is

$$H = \epsilon\hat{E} + \frac{\lambda}{2}\hat{\Lambda} + \frac{w}{2}\hat{W} - g\hat{G} \tag{3.3}$$

where

$$\hat{E} = \sum_{i}^{N} \left(a_i^\dagger a_i - a_{i+N}^\dagger a_{i+N} \right), \tag{3.4}$$

$$\hat{\Lambda} = \sum_{q,p=1}^{N} \left(a_p^\dagger a_q^\dagger a_{q+N} a_{p+N} + a_{p+N}^\dagger a_{q+N}^\dagger a_q a_p \right), \tag{3.5}$$

$$\hat{W} = \sum_{q,p=1}^{N} \left(a_{p+N}^\dagger a_q^\dagger a_{q+N} a_p + a_p^\dagger a_{q+N}^\dagger a_q a_{p+N} \right), \tag{3.6}$$

and

$$\hat{G} = \sum_{p,q=1}^{N} a_{2p-1}^\dagger a_{2p}^\dagger a_{2q} a_{2q-1}. \tag{3.7}$$

This Hamiltonian describes a system of spinless fermions with two energy levels each of which contains N orbitals. Within these levels, there is a pairing force between sets of adjacent $(2k-1, 2k)$ orbitals, $\hat{G}$, derived from the BCS Hamiltonian. This pair force can also move these pairs of particles to other sets of empty adjacent orbitals. Additionally, the LMG model introduces several terms, the first of which, $\hat{E}$ is set to zero in this study as it is unnecessary to maximize either form of condensation. The $\hat{\Lambda}$ scattering force moves pair of particles between the energy levels, and the $\hat{W}$ scattering force interchanges particles between the levels, leaving the occupation number within each level unchanged. The eigenvalues of the resulting ground-state 2-RDMs are bounded from above by $\lambda_D \leq \frac{N}{2}\left(1 - \frac{N-2}{r}\right)$ [16] and $\lambda_G \leq \frac{N}{2}$ [152] where r is the number of orbitals or $2N$ in this system.

3.3.3 Geometry of the Set of 2-RDMs

Exploration of the FEC system in this paper is done with methods recently developed within the field of quantum information theory that utilize the convexity of the set of ground-state 2-

RDMs to provide a visually compact overview of the infinite space of Hamiltonians [107, 108, 106, 158]. Analyzing the geometry of the resulting structure can give significant information about quantum criticality in the system, even in the finite particle limit [158]. Abstract concepts like symmetry breaking become readily visible in the form of ruled surfaces on the convex set, and discontinuities in the surface of the set serve as an indication of first-order phase transitions. Additionally, this approach allows for the identification of critical phenomenon by observing the 'speed' of the RDM along the edge of the set moving between Hamiltonian configurations H_i and H_f linearly in the space of Hamiltonians as described by

$$H_t = H_i\,(1-\chi) + \chi H_f \tag{3.8}$$

This 'speed' or curvature of the set is then defined as $(v \cdot v)^{1/2}$ with

$$v = \left(\frac{\partial \langle \hat{\Lambda} \rangle}{\partial \chi}, \frac{\partial \langle \hat{W} \rangle}{\partial \chi}, \frac{\partial \langle \hat{G} \rangle}{\partial \chi} \right). \tag{3.9}$$

These methods can be used to provide a high-level overview of the system, by compressing the infinite space of Hamiltonians into a convex set that emphasizes regions of interest through easily discernible visual cues. This then allows for a more focused study of the areas of interest with traditional methods like energy-level analysis.

In order to characterize phase behavior as well as the exciton and fermion-pair condensation within the system, the ground-state RDMs for the finite-particle Hamiltonians are solved exactly. The D and G matrices are then analyzed as discussed above to provide an overview of the critical phenomenon in the system.

3.4 Results

We address results attainable from finite-particle simulations of the system, and analyze these results through the RDM approach to QPTs in section 3.4.1. These results then are

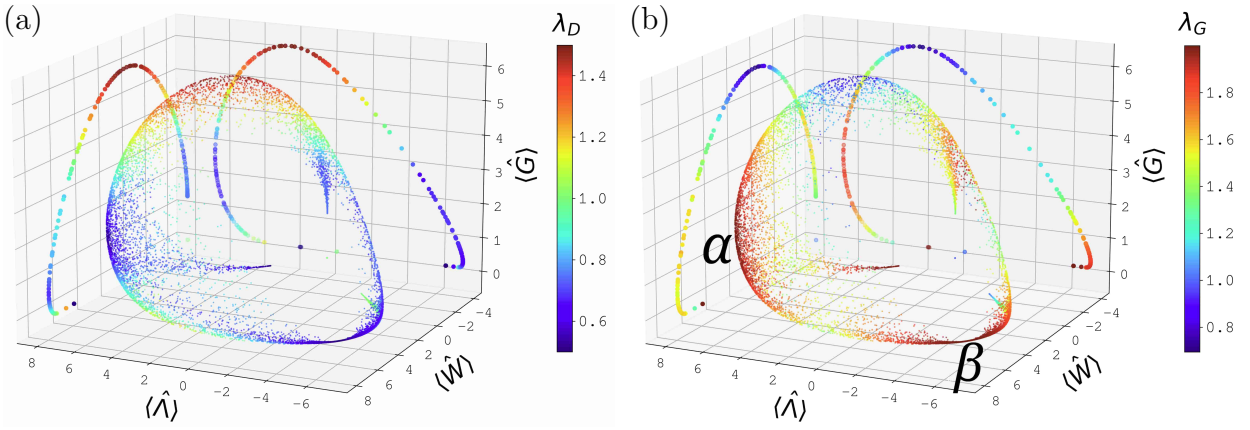

Figure 3.1: Color map of Fermion-Pair and Exciton Condensation on the Convex Set of 2-RDMs. This scatter plot shows the resulting RDMs from a random sampling of Hamiltonian, Eq.3.3, configurations with a color map indicating the value of λ_G and λ_D for 3.1b and 3.1a respectively. Additionally, both plots contain the convex hull of the projections of the 3-D plot into the $\langle\hat{\lambda}\rangle$-$\langle\hat{G}\rangle$ and $\langle\hat{W}\rangle$-$\langle\hat{G}\rangle$ planes. In Figure 3.1b, α and β are marked to distinguish two regions of exciton condensation character.

used to extrapolate to the thermodynamic limit through construction of the ground-state wave functions in section 3.4.2.

3.4.1 Finite Particle

Investigation of the condensate character and critical behavior of the set of ground-state RDMs for the minimal four particle system can be seen in Figure 3.1. Figures 3.1a and 3.1b show the regions with exciton and fermion-pair condensation (FPC) or high values for λ_D and λ_G, respectively. The regions with hotter coloring (red/orange) exhibit the highest levels of condensation, while cooler colors (blues) have limited to no condensation. Figure 3.1 shows that there exists a significant yellow tinged area with high values of both λ terms ($\lambda_i > 1$) between the regions of single condensation, indicating the existence of simultaneous fermion-exciton condensation (FEC) as reported in the initial and subsequent investigations of this system [145, 10, 159]. In Figure 3.1b, two separate regions seem to maximize the exciton condensation (EC), marked as α and β, while one region in 3.1a maximizes the

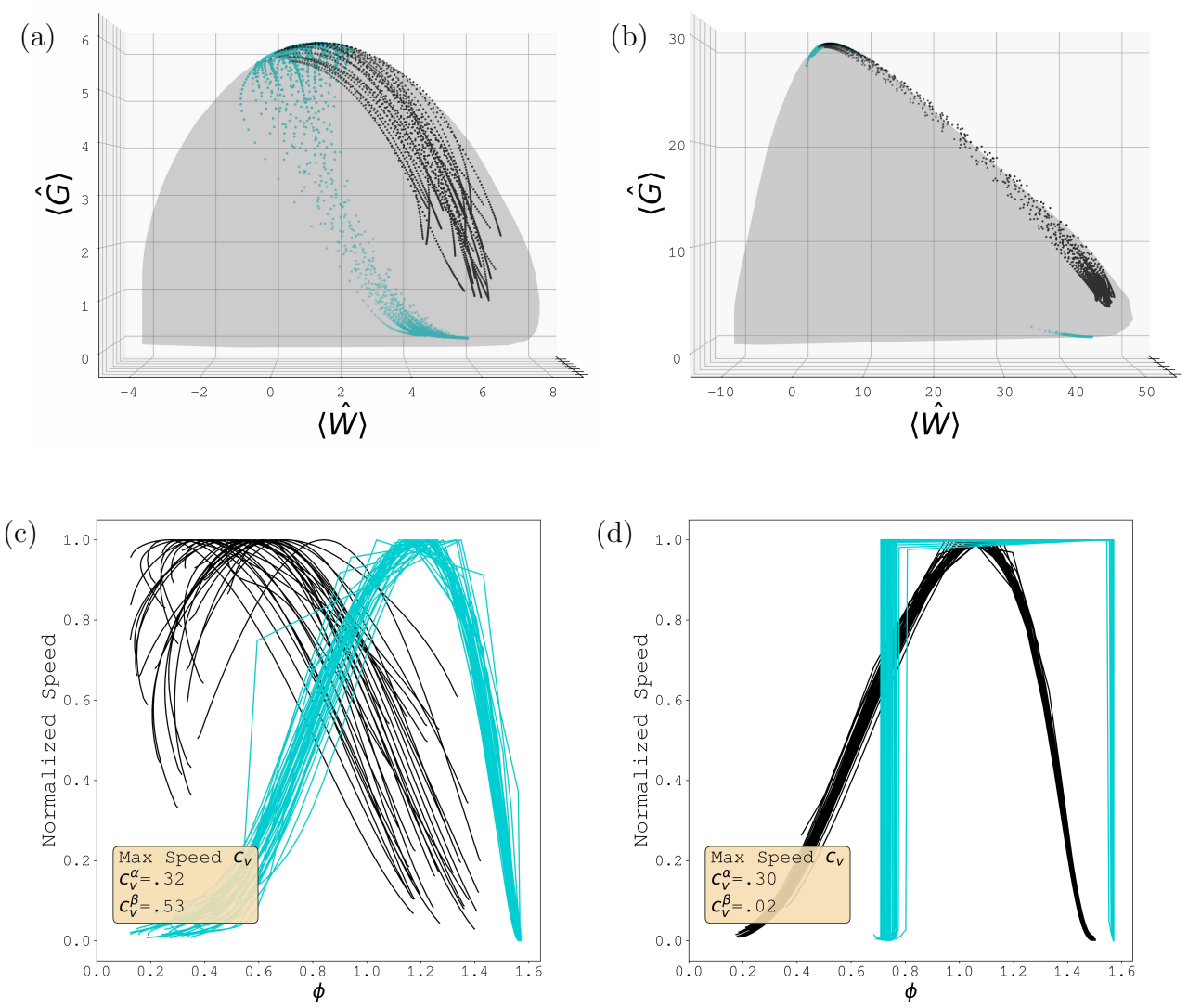

Figure 3.2: Coalescing Trajectories from EC to FPC Regions. Figures 3.2a and 3.2b illustrate several dozen trajectories from the α, in black, and β, in grey, regions to the FPC. A light grey shape illustrates the extent of the convex hull of the set of 2-RDMs. Figures 3.2c and 3.2d show the normalized 'speed' of the points along the convex set for both groups of trajectories with respect to the altitude angle ϕ in radians. The coefficient of variance for the maximum speed attained along the trajectories is listed in the bottom left corner.

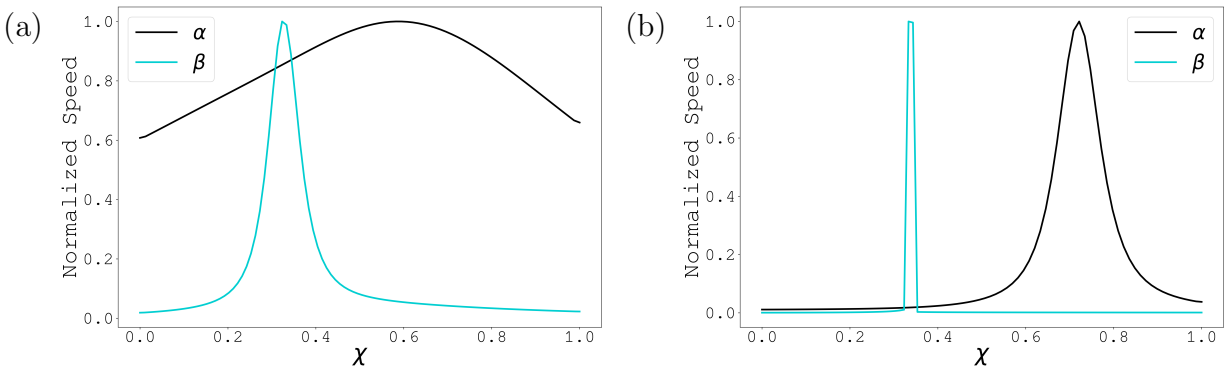

Figure 3.3: Speed of the α and β Trajectories. Figures 3.3a and 3.3b show the speed of a random trajectory from those plotted in Figure 3.2 for the 4 and 10 particle systems, respectively. χ is the parameter for the function describing the line between the starting and final Hamiltonians of the trajectories.

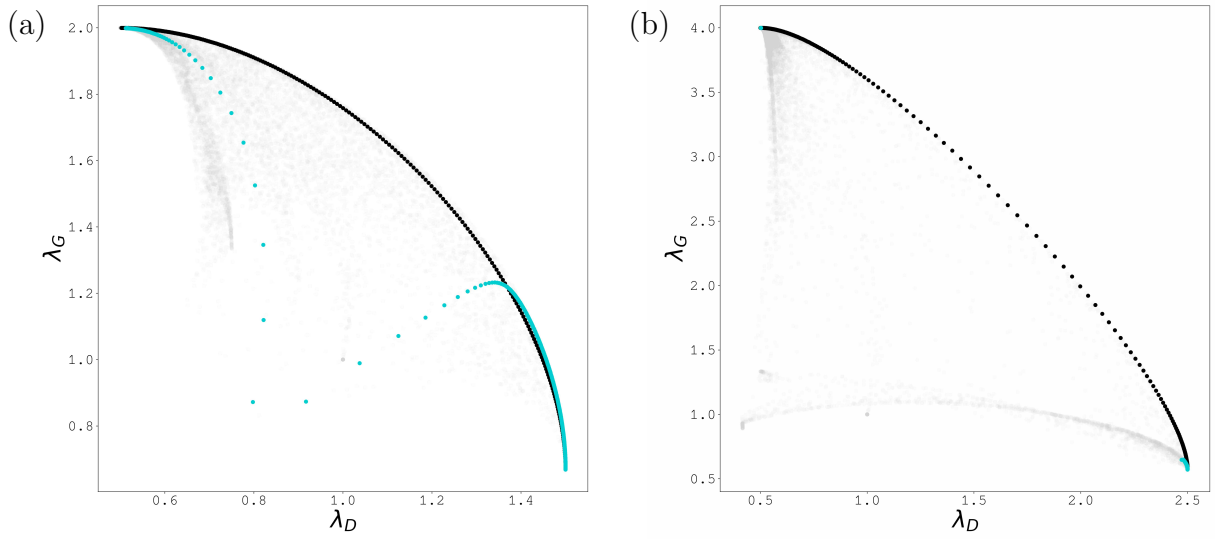

Figure 3.4: λ Values along Trajectories. Figures 3.4a and 3.4b contain a α, in black, and a β, in grey, trajectory for the 4 and 8 particle systems, respectively. The light grey dots are the result of a random sampling of ground-state 2-RDMs.

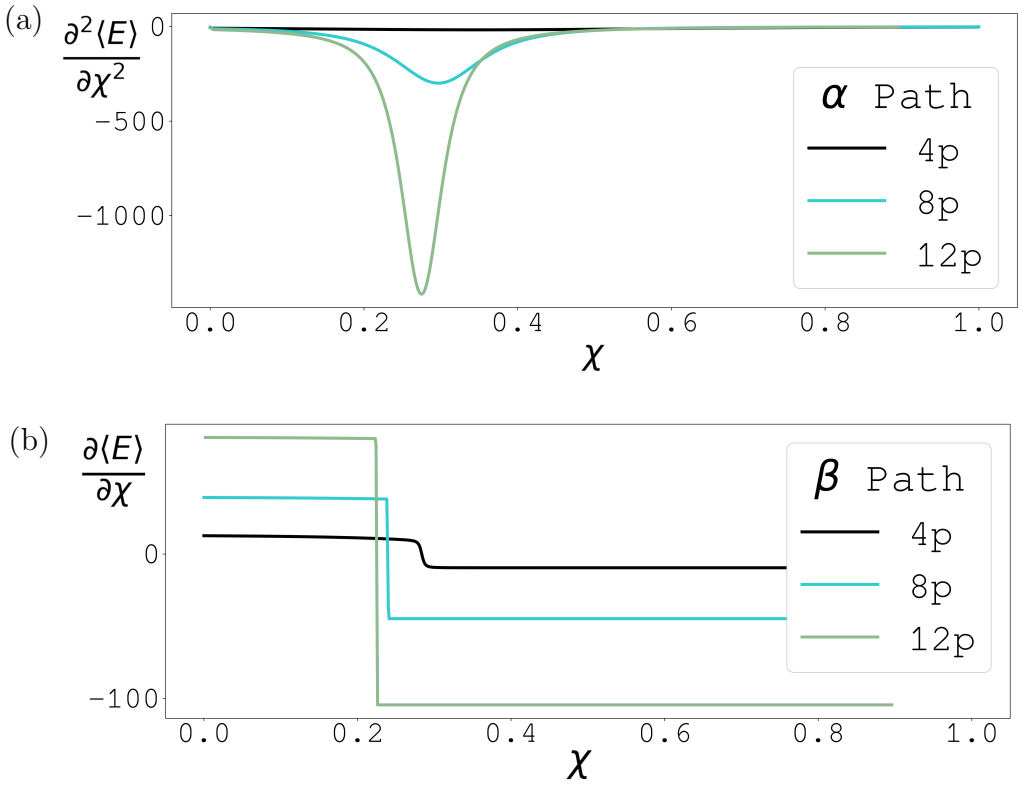

Figure 3.5: Derivatives of the Ground State Energy Along Trajectories. Figure 3.5a shows the second derivative of the ground-state energy with respect to χ, a parameter of a α line in Figure 3.3, for the 4, 8, and 12 particle systems. Figure 3.5b shows the first derivative of the ground-state energy along a β trajectory for the 4, 8, and 12 particle systems.

FPC. This RDM depiction of the system allows for a rapid assessment of the properties of the two different EC regions. Both EC regions have large positive values for the $\langle\hat{W}\rangle$, which is to be expected as the $\hat{W}$ term of the Hamiltonian scatters particle-hole pairs around the lattice. However, the two EC regions differ in regards to the expectation value of $\hat{\Lambda}$, which is the scattering term that moves pairs of particles (or holes) between the two degenerate energy levels. These observations raise several questions: What is the critical behavior of the system as it transitions between the FPC and EC regions, and does this behavior differ when comparing the α or β regions? Additionally, does the existence of two separate EC regions indicate the existence of two types of FECs?

As discussed in prior RDM studies, the 'speed', Eq. 3.9, of a trajectory between two

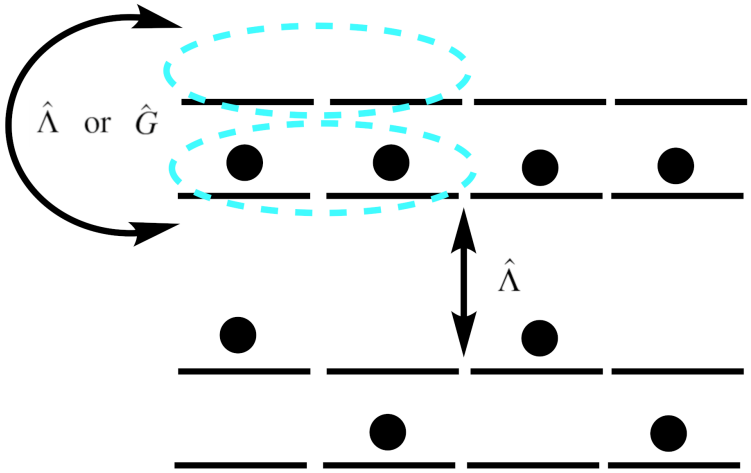

Figure 3.6: $\hat{\Lambda}$ Scattering. The upper most arrow shows a form of scattering that could be due to either the pair-force $\hat{G}$ term or the $\hat{\Lambda}$ term. While the lower arrow demonstrates how the $\hat{\Lambda}$ scattering is able to entangle states with large contributions to the maximal eigenstates of $\hat{W}$ with states that have large contributions to the maximal eigenstates of the pair-force term.

Hamiltonian configurations in the finite particle limit can serve as an indication of the presence of critical behavior in the thermodynamic limit [106, 158]. For example, any abrupt changes in speed of the RDM along the surface of the convex set as the system is taken from the α to FPC region would indicate the development of some critical phenomenon between those regions. However, it is possible that the critical behavior along some of the paths between the regions differ drastically. Figure 3.2 shows several dozen linear trajectories in the space of Hamiltonians, see Eq. 3.8, that are between randomly chosen Hamiltonians in the different condensate regions. Grey lines are used to indicate paths between the β and FPC regions and black lines for trajectories between the α and FPC regions. For the four particle system, the trajectories in Figure 3.2a show significant spread over the surface of the convex set of RDMs, which is illustrated as a grey shadow in the figure. Additionally, the trajectories appear to differ in where they become sparse, or where their speed is the highest. This difference in the speed domain can be seen in Figure 3.2c with the position of maximum speed differing significantly between the trajectories. The shapes of the speed

curves also seem to differ, with a particularly large coefficient of variance for the maximum speed of the β curves.

However, as the particle number increases there is a drastic decrease in the variability of the trajectories. The 3D-scatter plot of the curves shows a coalescing of the trajectories with the sparsity in the black α curves occurring in the same region, which is supported by the speed graph, Figure 3.2d, that displays that the maximum speed is obtained at nearly the same point for all of the curves. The β curves also seem to become discontinuous at roughly the same point and their speed curves seem to be converging to a similar shape. The coefficient of variance of the maximum speed for the α curves, c_v^α, is lower, and has been seen to decrease continually for higher particle numbers indicating that properties like the critical exponents are converging as well. The decrease in c_v^β, while more significant, has slightly less meaning as all of the curves become discontinuous. This discontinuity reflects symmetry breaking in the system, and demonstrates the observation of abstract phenomena in the RDM formalism. Additionally, this data suggests that the critical behavior of the α and β sets of trajectories can be roughly characterized by a single trajectory, and in the thermodynamic limit properties such as the critical exponents of the transition will converge to the same value. This convergence results from the dampening of the effect of local fluctuations on the expectation values of the ground-state RDMs away from critical points as the particle number increases [29].

The speeds for a single α trajectory are plotted in Figures 3.3a and 3.3b. In these Figures, the hump showing the speed grows with the particle number, which indicates that it will likely become discontinuous in the thermodynamic limit. Therefore, this is the finite-particle signature of a quantum phase transition along this trajectory. The exact order of the QPT lying along the α trajectories cannot be determined from the speed alone, but can be discovered through more a traditional analysis of the ground-state energy. The grey or β line shows this same acceleration to a much larger degree. The RDMs along the β

line seem to "leap" from the region of exciton condensation to fermion condensation almost instantaneously in the eight-particle case. This leap, as discussed before, is an indication of symmetry breaking, and that this transition is first order.

This "leap" can also be seen in Figure 3.4 which shows the same trajectories, but now in the space of the signatures of condensation for excitons and particle-particle pairs, i.e., a plot of λ_G vs λ_D. This plot contains a light-grey scattering of a random sample of RDMs to illustrate the extent of the accessible λ region. In the four- and eight-particle cases the black line travels through the space of RDMs along an ellipse that simultaneously maximizes both of the λ values. However, the grey line for the four-particle case shows a drastic drop in the eigenvalues along the trajectory, while the eight-particle case skips the FEC region entirely. This demonstrates that the FEC only exists along the α trajectory, and that only one type of FEC exists in the thermodynamic limit of the system. These results for the β trajectory suggest that the large positive energy contribution of the $\hat{\Lambda}$ term in the Hamiltonian directly conflicts with the system's ability to become a FPC. This is a result of two separate functions of this scattering term. The first can be observed in Figure 3.1b, where the FPC condensate region seems to lie mostly above $\langle\hat{\Lambda}\rangle$=0 as seen in the projection into the $\langle\hat{\Lambda}\rangle - \langle\hat{G}\rangle$ plane. This preference for FPC to lie above $\langle\hat{\Lambda}\rangle$=0 is likely the result of the $\hat{\Lambda}$ scattering working cooperatively with the $\hat{G}$ pair-force term to lower the energy, by moving pairs of particles between the paired orbitals in the same way as the pair-force term as illustrated in the upper half of Figure 3.6. The potentially more crucial function of the $\hat{\Lambda}$ term, however, is the connection of states with large contributions to the $\hat{W}$ term with the pair-force states. In other words, the $\hat{\Lambda}$ scattering provides off-diagonal entanglement between exciton states and fermion-pair states as seen in the bottom half of Figure 3.6. When this scattering is energetically unfavorable, as is seen in the β trajectories in Figure 3.4, there is a dip or a leap in the eigenvalues as the system is unable to entangle the states from the two regions of condensation, resulting in what appears to be the formation of a first-order phase transition

between the states which minimize $\hat{W}$ and $\hat{G}$.

Analysis of the ground-state energy of the system as it travels along the trajectories outlined above can be seen in Figure 3.5. These results largely confirm those already gathered from RDM techniques, but allow for a deeper analysis of the order of the phase transitions postulated. Figure 3.5a shows that the second derivative of the energy along the α trajectory is rapidly growing as the particle number increases, likely becoming discontinuous in the thermodynamic limit. This indicates that a second-order or higher-order quantum phase transition is occurring between the α and FPC regions of condensation. While along the β trajectories, the first derivative of the energy is seemingly already discontinuous even with a finite number of particles, which is a result of the actual level crossing that occurs in the system. This means that a first-order phase transition exists between the β and FPC regions, but this was already clear from the discontinuity of the trajectories on the RDM set.

3.4.2 Thermodynamic Limit

The first-order transition can be extrapolated to the thermodynamic limit through analysis of the structure of the ground-state wave functions. The β region Hamiltonians are dominated by contributions of $\hat{\Lambda} - \hat{W}$. By diagonalizing this term in the finite-particle limit, a clear pattern emerges in the ground-state subspace. The ground-state is doubly degenerate, and this subspace can be characterized by wave functions of the form:

$$|\Psi_1^\beta\rangle = (-1)^{\hat{L}} \left[c_1 \Big(\sum_j^{N/2} \sum_i |\phi_i^{2j}\rangle \Big) + c_2 \Big(\sum_j^{N/2-1} \sum_i |\phi_i^{2j+1}\rangle \Big) \right] \tag{3.10}$$

$$|\Psi_2^\beta\rangle = (-1)^{\hat{L}'} \left[c_2 \Big(\sum_j^{N/2} \sum_i |\phi_i^{2j}\rangle \Big) + c_1 \Big(\sum_j^{N/2-1} \sum_i |\phi_i^{2j+1}\rangle \Big) \right] \tag{3.11}$$

Where $|\phi_i^k\rangle$ is the ith Lipkin-like wave function (a state without occupations of both p and $p+N$ orbitals) with k occupied orbitals in the 'upper' energy level (or k occupied orbitals

numbered greater than N) and

$$\hat{L} = \lfloor \left(\sum_{i}^{N} a_i^\dagger a_i \right) /2 \rfloor \tag{3.12}$$

$$\hat{L'} = \lfloor \left(\sum_{i}^{N} a_i^\dagger a_i + 1 \right) /2 \rfloor, \tag{3.13}$$

Which are equivalent to counting the number of pairs of particles in the 'upper' (p $\geq$ N) energy level. It is apparent from the structure of the wave function that it represents an exciton condensate because of the large variability in both the number and location of excitations throughout the lattice.

The proposed first-order transition occurs along the path $\hat{H} = \hat{\Lambda} - \hat{W} \rightarrow \hat{G}$. However, it can be shown (see Appendix A) that $\hat{G}\,|v\rangle = 0$ where $v \in |\Psi_1^\beta\rangle \otimes |\Psi_2^\beta\rangle$. This means that $|v\rangle$ is an eigenvalue for any Hamiltonian along the path. Therefore the ground-state will only change at an actual energy level crossing, as the degenerate subspace is diagonal, and thus uncoupled, to any other energy levels. Slight perturbations to the Hamiltonian from the path outlined above, only break the degeneracy of the ground-state subspace, but do not change its diagonal and uncoupled nature.

Similar analysis of the ground-states in the α and FPC regions reveal wave functions of the form:

$$|\Psi_1^\alpha\rangle = \left[c_1 \left(\sum_{j}^{N/2} \sum_{i} |\phi_i^{2j}\rangle \right) + c_2 \left(\sum_{j}^{N/2-1} \sum_{i} |\phi_i^{2j-1}\rangle \right) \right] \tag{3.14}$$

$$|\Psi_2^\alpha\rangle = \left[c_2 \left(\sum_{j}^{N/2} \sum_{i} |\phi_i^{2j}\rangle \right) - c_1 \left(\sum_{j}^{N/2-1} \sum_{i} |\phi_i^{2j-1}\rangle \right) \right] \tag{3.15}$$

and

$$|\Psi_{FPC}\rangle = N \left(\sum_{i} |\psi_i\rangle \right) \tag{3.16}$$

where $|\psi_i\rangle$ is the ith BCS-like state, meaning that if orbital $2j$ is occupied, then orbital $2j-1$ must be occupied as well. The α wave functions are not eigenvectors of $\hat{G}$ due to their internal parity relying on even or odd occupation of the different energy levels. However, $\hat{G}$ acting on α wave functions generates non-Lipkin-like states (see Appendix A for the action of $\hat{G}$ on Lipkin-like states), a subset of which are BCS-like states. This coupling between the two different ground-states, is what allows for a smooth transition (or avoided level crossing) between the regions of the RDM. This further confirms that if a QPT exists in the thermodynamic limit (which as discussed in earlier sections looks likely as the finite particle signature of the transition seems to grow sharper with increasing particle number), it will be a 2nd order or higher transition.

3.5 Discussion and Conclusions

The exploration of the critical behavior of this system brings to light several interesting revelations. Through a combination of RDM techniques, a mapping of the space of Hamiltonians to the convex set of RDMs reveals multiple excitonic phases in the system. This color map also highlights the regions with FEC states. Increasing the particle number increases the curvature of the set, or increases the 'speed' of the trajectories traveling through the regions containing the FEC states, resulting in the discovery of a first-order quantum phase transition between the "β" exciton and the fermion-fermion condensate regions, and a second-order transition between the "α" exciton and FPC regions. Using the RDM set as a guide, it is possible to apply more traditional wave function analysis to the transitions. The characteristic ground-state wave functions for each of the regions are then used to extrapolate the behavior of the system at the thermodynamic limit confirming the existence of the QPTs.

Several interesting questions still remain about the system. The first concerns the behavior of the system at non-zero temperature. How resilient are the condensates to temperature,

and do novel phases emerge? Additionally, would constraining the BCS and LMG terms to a limited spatial area, to make the interactions more applicable to common crystal systems, completely suppress condensation? This would require defining a specific lattice shape, and with the BCS term it might be possible to generate zero energy edge states in the system much like the Kitaev chain. As two different symmetries, L and even/odd parity, seem to dominate the system, perhaps these could be used to generate symmetry protected topological states.

An experimental realization of this material may be able to take advantage of the finding that the FEC region lies between fermion-fermion pair and exciton condensate phases. This suggests that one route to an FEC material is placing a excitonic material, like a bilayered system or a gapped system [160], on a bulk superconductor. Ideally, this bilayered system would also be able to exhibit superconductivity in some regimes (a possible candidate being twisted graphene). The superconducting character of the heterogeneous system could then be potentially controlled by varying the temperature of the system or by inducing a voltage along the junction of the materials. By lowering the temperature or increasing the voltage, the bulk superconductor will begin to donate a greater number of Cooper pairs into the bilayer, and potentially increase the superconducting character of the bilayer until it exhibits FEC. Studying simple composite systems computationally will increase our theoretical understanding of this novel form of condensation and help build the framework necessary for an experimental realization of Fermion-Exciton Condensation.

3.6 Appendices

3.6.1 Appendix A

The proposed 1st order QPT arises from the symmetry of the degenerate ground-state in the β exciton region. This symmetry, L (Eq. 3.12), which swaps the sign of states with 'upper'

(orbital number $\geq N$) occupation values differing by 2, preserves the degenerate subspace in the FPC region, dominated by $\hat{G}$. This can be proven by differentiating the basis functions given in the paper, with new quantum numbers, which allow for an easier analysis of the effect of $\hat{G}$ on the wave functions.

With these new quantum numbers, $|\Psi_1^\beta\rangle$ can be defined as:

$$\begin{aligned} |\Psi\rangle = c_1 \left(\sum_{j=0,2,..}^{N/2} \sum_{i=0,2,..}^{N/2-j} |i,j\rangle_L - |i+1,j\rangle_L \right) \\ + c_2 \left(\sum_{j=1,3,..}^{N/2} \sum_{i=0,2,..}^{N/2-j} |i,j\rangle_L - |i+1,j\rangle_L \right) \end{aligned} \tag{3.17}$$

where $|i,j\rangle_L$ is a Lipkin-like wave function (i.e. orbitals p and $p+N$ cannot be occupied simultaneously), i is the number of occupied adjacent orbitals $(2p, 2p-1)$ where $p \geq N$, and j is the number of Lipkin-like pairs where $(2p, 2p-1+N)$ or $(2p+N, 2p-1)$ are occupied. It should be noted that the first and second term contain wave functions with even and odd occupations of the 'upper' energy level, respectively. For any i and j, there are $\binom{N/2}{j}\binom{N/2-j}{i}$ arrangements of particles in the lattice which satisfy these conditions, and $|i,j\rangle_L$ is an equal and positive superposition of all of these configurations.

Recall that $\hat{G}$ is only able to move pairs of particles occupying $(2k, 2k-1)$ orbitals, therefore it cannot act on particles forming Lipkin-like pairs. This means j is uneffected by the BCS operator. Applying $\hat{G}$ to a $|i,j\rangle_L$ results in a new superposition:

$$\begin{aligned} \hat{G}\,|i,j\rangle_L = G_L^{=}\,|i,j\rangle_L + G_L^{+}\,|i+1,j\rangle_L + G_L^{-}\,|i-1,j\rangle_L \\ + G_{NL}^{=}\,|i,j\rangle_{NL} + G_{NL}^{+}\,|i+1,j\rangle_{NL} + G_{NL}^{-}\,|i-1,j\rangle_{NL} \end{aligned} \tag{3.18}$$

Where $|i,j\rangle_{NL}$ is a state with one set of occupied orbitals $(2p, 2p-1, 2p+N, 2p-1+N)$, which is a state not found in the traditional LMG model. These Non-Lipkin-like conditions result in $\binom{N/2}{j}\binom{N/2-j}{1}\binom{N/2-j-1}{i-1}\binom{N/2-j-i}{1}$ possible arrangements of particles in the lattice

which are also summed in an equal superposition to generate the wave function $|i,j\rangle_{NL}$. It can be rationalized that the G terms are determined by the following relationship:

$$G_{L/NL}^{+/-/=} = \frac{D\left(|i,j\rangle_L\right)\left(E_{L/NL}^{+/-/=}\right)}{D\left(|i\pm 1/i,j\rangle_{L/NL}\right)} \tag{3.19}$$

where $D\left(|i,j\rangle\right)$ is the number of arrangements of particles in the lattice which satisfy i and j (given above), and E is the number of arrangements any specific configuration that satisfies i and j can be excited/de-excited to. E must be the same for every arrangement of the same i and j. It is easy to rationalize this fact for Lipkin states going to Lipkin states as the number of excitations/de-excitations is exactly equal to the number of BCS pairs in the 'lower'/'upper' energy levels (changing the occupied orbital label by $\pm N$). This number, i or $N-i-j$, must be the same for any of the arrangements of particles in the lattice, which compose $|i,j\rangle_L$.

Solving this equation for the various values of G reveals:

$$\begin{aligned}\hat{G}\,|i,j\rangle_L = {} & (N-j)\,|i,j\rangle_L + (i+1)\,|i+1,j\rangle_L + (N-j-i+1)\,|i-1,j\rangle_L \\ & + 2\,|i,j\rangle_{NL} + |i+1,j\rangle_{NL} + |i-1,j\rangle_{NL}\,.\end{aligned} \tag{3.20}$$

Finally applying these terms to G acting on $|\Psi\rangle$:

$$\begin{aligned}\hat{G}\,|\Psi\rangle &= \hat{G}\left(..-|i+1,j\rangle_L + |i,j\rangle_L - |i-1,j\rangle_L\right) \\ &= .. + \left(-\left(N-j-(i+1)+1\right) + (N-j) - i\right)|i,j\rangle_L \\ &+ (-1+2-1)\,|i,j\rangle_{NL} + ... = 0\end{aligned} \tag{3.21}$$

demonstrates that $|\Psi_1^\beta\rangle$ is an eigenvalue of $\hat{G}$. The exact same arguments can be applied to $|\Psi_2^\beta\rangle$, and therefore $\hat{G}\,|v\rangle = 0$.

CHAPTER 4

TOPOLOGICAL PHASE TRANSITIONS CAPTURED IN THE SET OF REDUCED DENSITY MATRICES

Republished with permission from Samuel Warren, LeeAnn M. Sager-Smith, and David A. Mazziotti, *Physical Review B.* **109**, 4, 045134. Copyright 2024 American Physical Society.

4.1 Abstract

Topological phase transitions fall outside of the symmetry-breaking paradigm and therefore elude many traditional analytical methods. In particular, significant geometric features found in the set of reduced density matrices (RDMs) disappear in symmetry-preserving topological systems. By returning to the fundamental properties of phase transitions, such as the divergence of correlation length and energy surface discontinuities, we demonstrate that the set of RDMs captures the critical behavior of systems with topological order. We find signatures of the gapless transition in the discontinuous movement of the ground-state RDMs. Additionally, the correlation length divergence near critical points appears in the off-diagonal character of RDMs, which is quantified through spectral and linear fitting analyses. This framework generalizes the quantum information approach to RDM critical theory, allowing for classification and visualization of all of the phases of the system—both topological and trivial—in the convex set of RDMs.

4.2 Introduction

Topological phase transitions, transitions that do not break system symmetries, have garnered significant theoretical and experimental interest due to the robust zero-energy edge states found in topological phases [161, 162]. These resilient states are used in topological light emitting devices to protect against fabrication defects [163, 164, 165, 166, 167, 168].

Additionally, research into topological quantum memory and computing focuses on harnessing the robustness of these edge states to reduce errors [138, 169, 170, 171]. Topological order has also been used to explain exotic experimental phenomena like the quantum, spin, and fractional Hall effects [172, 173, 174, 175, 176, 177]. However, many of the traditional analytical methods for studying phase transitions rely on symmetry breaking and therefore fail to capture the behavior of topological transitions.

The study of the relationship between reduced density matrices (RDMs) and quantum phase transitions was initiated by Erdahl and Jin [105], who noted that RDMs in different phases lie in significantly different regions of the set of RDMs. Gidofalvi and Mazziotti [106] later studied the movement of the RDMs between the regions with respect to critical parameters in the Hamiltonian and found that, in the vicinity of the transitions, the RDM moves very rapidly with one or more critical parameters and in the thermodynamic limit the speed becomes discontinuous at the critical point [107, 178]. This work was then followed by Zauner and Verstraete [108] who discovered that, in systems with symmetry-breaking phase transitions, the geometry of the set of RDMs has significant features, such as ruled lines and surfaces that appear on the boundary of the set, reflecting the degeneracy of the symmetry broken ground states. These features convey, without any reference to the underlying Hamiltonian, where symmetry breaking occurs in the system [179]. However, it was soon recognized by Chen [158] that the set of RDMs for systems with topological phases do not exhibit some of these geometric features such as the ruled lines and surfaces because no symmetries are broken between the trivial and topological regions. To recover the descriptive power of the RDM approach, aspects of the RDM set other than the ruled surfaces must be considered.

In this paper, we demonstrate that diverging correlation length and non-smooth energy

surfaces, signatures of phase transitions, are captured by an RDM approach to phase transitions regardless of the presence of symmetry breaking. Energy-surface discontinuities appear in the discontinuous movement of the RDM across the set, and the divergence of correlation length can be detected in the structure of the individual matrices of the set. We show that a simple visual inspection of the change in the RDMs during a transition reveals the divergence of correlation length, demonstrating an advantage of RDMs over the full N-body wave function, which can often obfuscate the true behavior of the system [180, 181]. Additionally, we show that linear and spectral analysis of the RDMs can quantify this correlation length divergence, and that analysis of higher order RDMs reveals the rapid changes in higher order correlations near the critical region [8, 7, 182, 101, 11, 183, 184, 185, 186].

To demonstrate this approach, we study the Su-Schrieffer-Heeger [187] and Kitaev chain models [188], two simple and extensively-studied systems that exhibit topological edge states. The latter model adds the additional novelty of Majorana fermionic edge modes, which have garnered significant interest for their non-abelian statistics, but have had limited study in the field of RDM mechanics. These examples show that significant information about topological phase and multi-state phenomena — e.g. gap closing — is captured entirely within the ground-state set of RDMs.

4.3 Theory

For any Hamiltonian parameter space, the ground-state RDMs form a convex set. In the presence of symmetry-breaking phase transitions, distinct geometric features like ruled lines or surfaces begin to appear on the hull, the outer shell of the set, in the thermodynamic limit [108, 179], reflecting the degeneracy of the symmetry broken ground states. The benefit of this method is the simple visual identification of abstract concepts like symmetry breaking, and the ability to visualize the entire phase space of the system in a finite convex set.

However, this methodology fails to generate the same stark geometric features in the presence of topological phase transitions, where no symmetries are broken between the trivial and topological regions [158]. Other factors in the set of RDMs and the structure of the individual matrices must be considered to recover the descriptive power of this methodology.

Initial investigations of the link between critical phenomenon and the set of 2-RDMs studied the movement of the RDMs near critical points. As the parameters of a Hamiltonian are varied, its ground-state RDMs move along the convex hull, and the speed or higher derivatives of this parametric curve become discontinuous near symmetry breaking quantum phase transitions [106, 107, 178]. This was then incorporated into Verstraete's geometric interpretation of the convex hull as a form of parametric curvature [108], expanding the analytical capability of both approaches. However, this connection between the two methods does not necessarily subject the speed or other Hamiltonian-dependent metrics to the same constraints as the ruled-surfaces approach when studying topological phases.

The movement of the RDMs arises from the changes in all one- and two-particle expectation values,

$$\frac{\partial^n r}{\partial \mathbf{t}^n} = \sqrt{\sum_i \left(\frac{\partial^n O_i}{\partial \mathbf{t}^n} \right)^2} \tag{4.1}$$

where O_i is the ith observable varied by the parameter(s) $\mathbf{t}$, and r is a coordinate for the RDMs within the convex set. As the Hamiltonian is a weighted sum of these observables, the behavior of the energy is intimately tied to the movement of the RDM. Near critical points, the system's energy or its higher derivatives become discontinuous despite the parameters changing continuously. Therefore, the observables are discontinuous, and thus, the movement of the RDMs must also become discontinuous.

In the case of topological phase transitions, each transition is associated with a closing of the bandgap. This closing, along with the spontaneous generation of zero-energy edge modes, introduces discontinuities into the energy surface near the critical points. These

discontinuities are then also found in the speed or higher derivatives of the RDMs. The speed, however, relies on knowledge of the Hamiltonian and its parameters, which are not needed in the symmetry-broken geometric analysis of the set of RDMs. A more Hamiltonian-agnostic approach to analyzing topological phase transitions with RDMs will require the investigation of other properties of RDMs in order to abstract the set from the system parameters.

The universality of phase transitions arises due to the divergence of correlation lengths near critical points. In topological insulating systems the correlation length directly coincides with the edge-state decay length [189]. This decay length is how far the edge states penetrate into the bulk of the material in the topological phase. If these edge states are Dirac fermions, they can be described as a linear combination of creation operators acting on the vacuum state, and are, therefore, natural orbitals of the 1-particle RDM (1-RDM)

$$ {}^{1}\mathrm{D}^{i}_{j} = \langle \Psi | \, \hat{a}^{\dagger}_{i} \hat{a}_{j} \, | \Psi \rangle \, . \tag{4.2} $$

where $\hat{a}^{\dagger}_{i}$ and $\hat{a}_{i}$ are the ith fermionic creation and annihilation operators, $|\Psi\rangle$ is the N-body fermionic ground-state wave function, and ${}^{1}\mathrm{D}$ is the 1-RDM. Therefore near the critical points, when the edge states are bleeding considerably into the bulk, more off-diagonal elements of the RDM will have finite values with the RDM becoming maximally off-diagonal at the point of the transition as the edge states collapse into the bulk.

The RDM approach to topological phase transitions can be generalized to quadratic Hamiltonians, with the study of the 2-RDM

$$ {}^{2}\mathrm{D}^{ij}_{kl} = \langle \Psi | \, \hat{a}^{\dagger}_{i} \hat{a}^{\dagger}_{j} \hat{a}_{l} \hat{a}_{k} \, | \Psi \rangle \, . \tag{4.3} $$

Quadratic Hamiltonians can contain additional non-particle conserving terms which do not appear in the 1-RDM, but result in strong 2-body correlation. While the 2-RDM contains additional information, it also contains information that is redundant with the 1-RDM. In

order to demonstrate the contribution of these non-particle conserving terms to the edge modes, it is possible to subtract the 1-RDM contributions from the 2-RDM leaving behind the cumulant part of the 2-RDM [190, 191].

$$^2\Delta = {}^2\mathrm{D} - {}^1\mathrm{D} \wedge {}^1\mathrm{D} \tag{4.4}$$

Where $\wedge$ is the Grassmann wedge product [124] and $^2\Delta$ is the two-particle cumulant. The largest eigenvector and value of the cumulant has been used extensively to demonstrate fermion-fermion [183, 192, 31, 193] and fermion-hole [194] correlation, pairing, and condensation in systems. Therefore, as a measure of correlation, the eigenvalue should experience significant changes as the system approaches a critical point due to the divergence of correlation length.

An additional metric that can be used to study both the 1- and 2-RDMs is the Pearson correlation coefficient (PCC), which can quantify the degree to which a matrix is diagonal. The PCC has also been used to study the time correlation between blocks of the RDMs and their cumulants [195]. In general, the PCC determines the degree of linear or anti-linear correlation between two sets of data, with a value between 1 (if the data lies along a line with a positive slope) or -1 (if the data lies along a line with a negative slope) and a value of 0 signifying no linear correlation between the two data sets.

This metric can also be used to determine the diagonal character of a matrix by measuring the correlation between the rows and columns. The elements of the RDM, being a density matrix, give a measure of the probability of two events (the column and row operators) occurring in the system. This suggests the following form of the PCC:

$$\frac{n\langle ij\rangle - \langle i\rangle \langle j\rangle}{\sqrt{n\langle i^2\rangle - \langle i\rangle^2}\sqrt{n\langle j^2\rangle - \langle j\rangle^2}}, \tag{4.5}$$

where for the 1-RDM

$$n = \sum_{i,j}^{N} |\langle \hat{a}_i^\dagger \hat{a}_j \rangle|$$
$$\langle i \rangle = \sum_{i,j}^{N} i |\langle \hat{a}_i^\dagger \hat{a}_j \rangle|$$
$$\langle ij \rangle = \sum_{i,j}^{N} ij |\langle \hat{a}_i^\dagger \hat{a}_j \rangle|.$$

Due to the Hermitian nature of RDMs, this can be simplified to

$$\frac{n\langle ij \rangle - \langle i \rangle^2}{n\langle i^2 \rangle - \langle i \rangle^2}, \tag{4.6}$$

where it can easily be seen that a diagonal matrix in which $\langle ij \rangle = \langle i^2 \rangle$ will have a PCC value of 1. Conceptually, the 1-RDM element $\hat{a}_i^\dagger \hat{a}_j$, gives a measure of how often the system is in a state where there is a particle at site j and no particle at site i. Thus, the absolute values of the elements can be thought of as the un-normalized frequency of these events. The PCC can then be used to measure the linear correlation between this series of pairs of events. Taking the case of a pure insulator, e.g. a chain of very distantly separated hydrogen atoms, the expected structure of the 1-RDM is entirely diagonal; thus, the PCC should be equal to 1. However, if a system contains a topological phase transition, the coupling between the edges and the bulk should result in a drastic drop in the PCC value when the band gap closes.

4.4 Results

This section analyzes the Su-Schrieffer-Heeger (SSH) and the Kitaev chain topological systems. First, the structure of the 1-RDMs is investigated, revealing the visual signature of topological edge states. Then the speed and off-diagonal character of the RDMs are analyzed

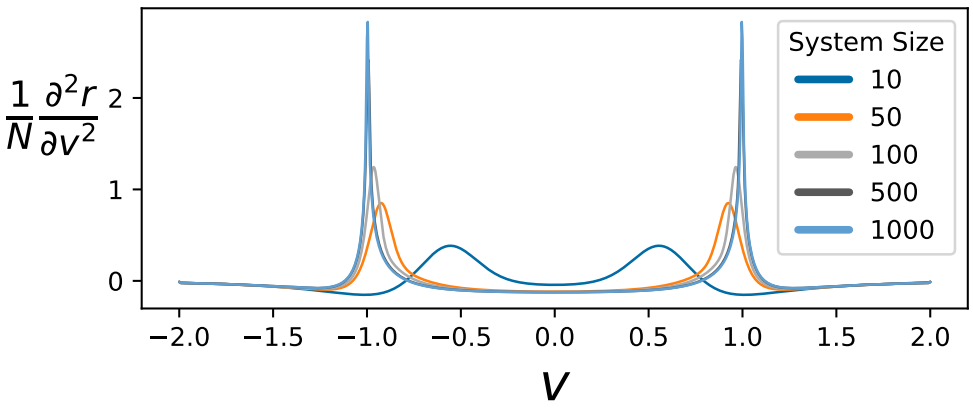

Figure 4.1: RDM acceleration through a topological phase transition in the SSH model. The acceleration is calculated using Eq. (4.1), and is divided by the system size for normalization. The results are for the ground-state RDM for a system that is tuned from [v,w]: [-2,-1]→[2,-1] (see Eq. 4.7) passing through 2 phase transitions at v=±1

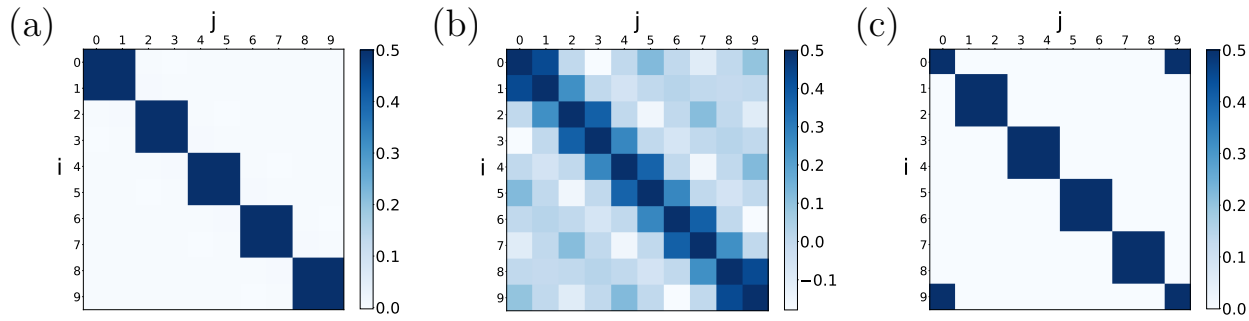

Figure 4.2: Structural changes in the 1-RDM near topological phase transition in the SSH Hamiltonian. Subplots (a)-(c) show the matrix elements of the 1-RDMs for a 10 site system in the trivial ($100v = w$), gapless ($v = w$), and topological phases ($v = 100w$), respectively, where each matrix element is given by $\langle \hat{a}_i^\dagger \hat{a}_j \rangle$.

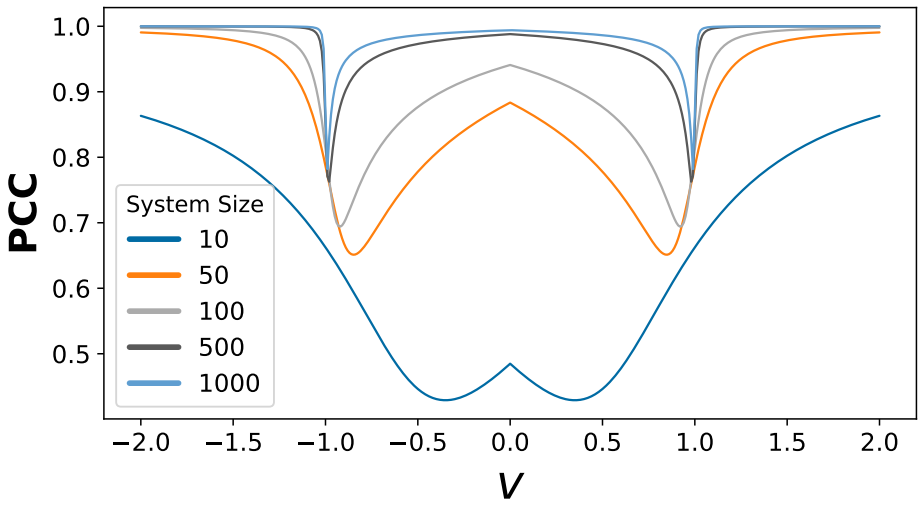

Figure 4.3: Change in the Pearson Correlation Coefficient near topological phase transitions in the SSH Hamiltonian. The Hamiltonian is tuned from [v,w]: [-2,-1]→[2,-1] (see Eq. (4.7)) passing through two phase transitions at v=±1.

as the system travels through a topological phase transition. Finally, in the Kitaev chain model, due to its non-number-conserving terms, the cumulant of the system can be analyzed, revealing the significance of 2-particle correlation in the topological transition.

4.4.1 SSH Model

One of the simplest systems with topological order is the Su-Schrieffer-Heeger model [187], which has garnered attention due to its experimental application in topological lasers [167, 163]:

$$\hat{H} = v \sum_{i=1}^{N} \hat{a}_{2i-1}^{\dagger} \hat{a}_{2i} + w \sum_{i=1}^{N-1} \hat{a}_{2i}^{\dagger} \hat{a}_{2i+1} + \text{h.c.} \tag{4.7}$$

where N is the number of particles in a half-filled chain, v and w are real parameters, h.c. denotes Hermitian conjugate, and the finite $2N$-site chain is treated without periodic boundary conditions. The first term in the Hamiltonian is block diagonal with blocks of $\sigma_x = \left(\begin{smallmatrix} 0 & 1 \\ 1 & 0 \end{smallmatrix}\right)$. Therefore, 1-particle solutions, when $|v| \gg |w|$ (far into the *trivial region*), are

of the form

$$|\Psi_i\rangle = \frac{1}{\sqrt{2}}(\hat{a}^\dagger_{2i-1} \pm \hat{a}^\dagger_{2i})\,|\emptyset\rangle \tag{4.8}$$

in which $|\emptyset\rangle$ is the vacuum state. The second term in the Hamiltonian is identical in the bulk of the material (aside from a shift up by 1 in the indices), but possesses two additional diagonal elements at the edges with eigenvalues of 0. These zero-energy edge states,

$$|\Psi_0\rangle = \frac{1}{\sqrt{2}}(\hat{a}^\dagger_1 \pm \hat{a}^\dagger_{2N})\,|\emptyset\rangle\,, \tag{4.9}$$

appear in the *topological region* ($|w| > |v|$).

The ground-state RDM's movement can be tracked as the system is taken through a topological phase transition. Figure 4.1 displays the normalized acceleration of the ground-state RDM for various system sizes. This is calculated using Eq. (4.1), which for this system can be explicitly expressed as

$$\frac{\partial^2 r}{\partial t^2} = \sqrt{\left(\frac{\partial^2 r_w}{\partial w^2}\right)^2 + \left(\frac{\partial^2 r_v}{\partial v^2}\right)^2}, \tag{4.10}$$

where

$$r_w = \langle\Psi(w,v)|\sum_{i=1}^{N}\left(\hat{a}^\dagger_{2i-1}\hat{a}_{2i} + \text{h.c}\right)|\Psi(w,v)\rangle \tag{4.11}$$

and

$$r_v = \langle\Psi(w,v)|\sum_{i=1}^{N-1}\left(\hat{a}^\dagger_{2i}\hat{a}_{2i+1} + \text{h.c}\right)|\Psi(w,v)\rangle\,. \tag{4.12}$$

The acceleration was chosen, as it is the lowest derivative of the movement that becomes discontinuous near the critical point, likely due to the curvature of the energy diverging near the gap closing. Even at small system sizes, significant changes in the acceleration of the RDM can be seen with the curves converging on a similar structure as the number of sites grows. Near $|v| = 1$, the acceleration begins to change rapidly with larger systems exhibiting

a larger normalized change, indicating that a phase transition would occur at this point in the thermodynamic limit. Therefore, the movement of the RDMs along the convex set continues to function as a useful parameter for finding both topological and symmetry-breaking phase transitions.

The transition between the topological and trivial regions can also be observed in the structure of the 1-RDMs as seen in Figures 4.2a, 4.2b, and 4.2c. In the trivial region, presented in Fig. 4.2a, the block diagonal structure of the 1-RDM shows that it is energetically favorable for pairs of neighboring sites to bind tightly together, and demonstrates the extremely local nature of the correlation in the system. At the transition point between the two phases, the gap closes, the material becomes conductive, and the correlation or, equivalently, the edge state decay length reaches its maximum. This is reflected in Fig. 4.2b where connections form between all of the neighbors dissolving the block diagonal structure. Finally, in the topological region, presented in Fig. 4.2c, there is the same insulating behavior in the bulk of the material that is observed in the trivial region, but now there exist distinct and highly visible connections between the edges of the chain, demonstrating how edge states are easily visualized in an RDM-based framework.

This off-diagonal character can be measured through the use of the PCC. Figure 4.3 shows the value of the PCC as the system is taken from the trivial region into the topological and back out again for varying particle number. As the particle number increases, a discontinuity appears to form in the PCC value at the exact point of the phase transition, $v = 1$. This discontinuity reflects the sudden increase in correlation length that occurs near a critical point. Interestingly, even in the low-particle limit (10 particles), taking the derivative of the PCC with respect to v reveals that the PCC changes most rapidly exactly at $v = 1$, indicating that this metric is incredibly sensitive to the gap closing even before the system approaches the thermodynamic limit. This plot also shows a discontinuity in the derivative of the PCC at $v = 0$, which disappears with increasing system size. By using a non-smooth

function like the absolute value of the RDM elements in the calculation of the PCC, when the sign of the elements flip, like at $v = 0$, a discontinuity occurs in the PCC.

This 'single particle' system generates ground states that are completely captured in the 1-RDM making the higher-order RDMs trivial and redundant. The next system, however, introduces two-particle correlations that complicate a purely 1-RDM based analysis.

4.4.2 Kitaev Chain

The Kitaev chain was developed as a simple system that can not only demonstrate topological order, but also produce Majorana edge modes (MEMs) [188]. The non-abelian statistics of these MEMs make them very appealing for quantum computing applications where they may protect against the intrusion of noise. Pairs of MEMs are defined as

$$\hat{m}_{2i} = \hat{a}_i + \hat{a}_i^\dagger \tag{4.13}$$

$$\hat{m}_{2i+1} = -i(\hat{a}_i - \hat{a}_i^\dagger), \tag{4.14}$$

which obey the anticommutation relationship $\{\hat{m}_i, \hat{m}_j\} = 2\delta_{ij}$ [196]. In order to obtain these states, Kitaev generated a Hamiltonian similar to the SSH chain, except that MEMs instead of Dirac fermions form on the edge.

The Hamiltonian can be written in terms of Dirac fermionic operators,

$$\hat{H} = \sum_i \mu \hat{a}_i^\dagger \hat{a}_i + \omega \left(\hat{a}_i^\dagger \hat{a}_{i+1} + \text{h.c.} \right) + \beta \left(\hat{a}_i \hat{a}_{i+1} + \text{h.c.} \right), \tag{4.15}$$

where the first term is a chemical potential, the second term is a nearest-neighbor hopping interaction, and the final term represents the superconducting gap. We will use $\hat{\mu}$, $\hat{\omega}$, and $\hat{\beta}$ to denote the operators found in the first, second, and third terms of the Hamiltonian. The cumulant eigenvectors for systems up to 18 sites are calculated through the exact diagonalization of the Hamiltonian, while through the use of the Bogoliubov transform it is

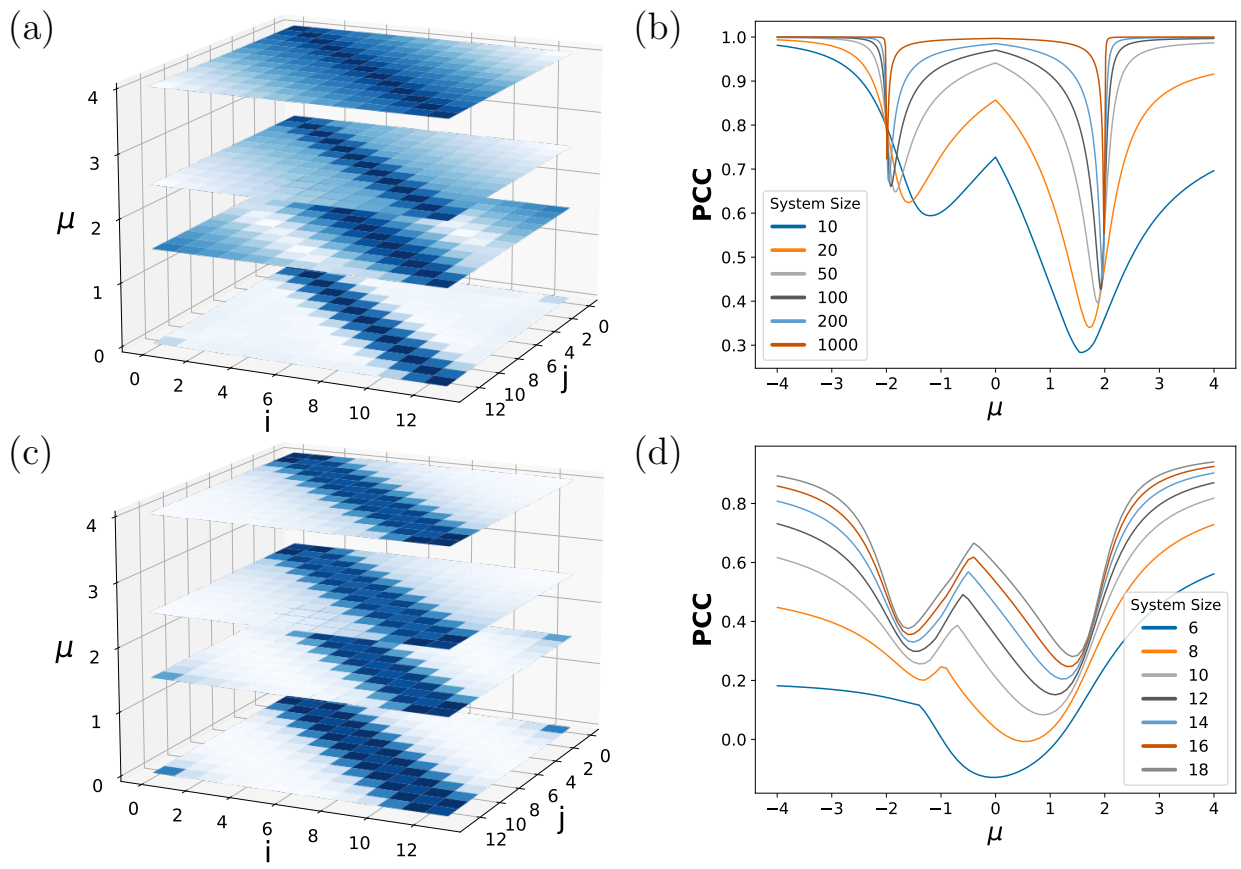

Figure 4.4: Signatures of topological phase transitions in the structure of the 1-RDM and the 2-Particle Cumulant in the Kitaev Chain Model. Subplot (a) shows the change in the structure of the 1-RDM as it is taken through a topological phase transition at $\mu = 2$ (to emphasize the shift of population to the edges, the color scale of the RDM element is logarithmic in base 10), and subplot (b) shows how this change is reflected in the PCC. Subplot (c) shows the changes in the structure of the eigenvector of the largest eigenvalue of the 2-particle cumulant (LCE) (see Eq.(4.17)), and Subplot (d) shows the PCC of the LCE as the system is taken through the same phase transitions. All of the plots have $[\omega, \beta] = [-1, -1]$ (see Eq.(4.15))

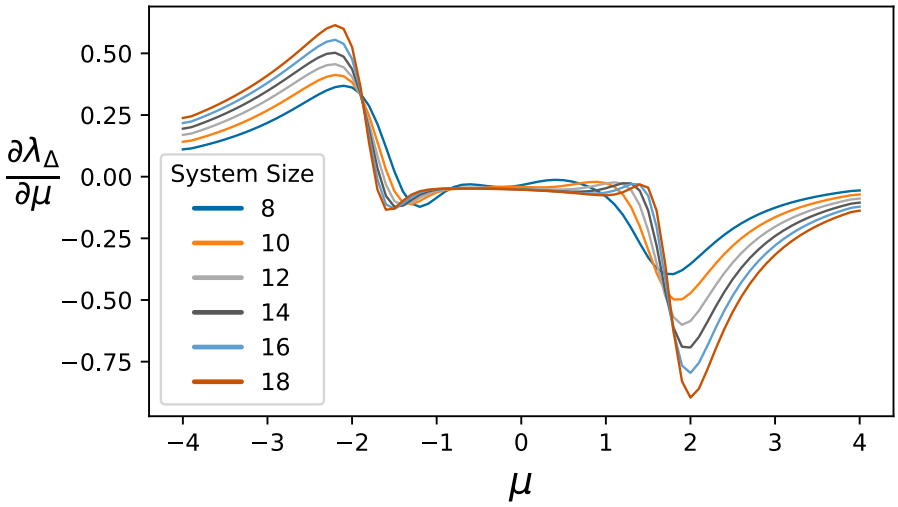

Figure 4.5: Changes in the Largest Cumulant Eigenvalue near topological phase transitions in the Kitaev Chain. The legend depicts the size of the system for 8-18 site systems as the Hamiltonian is tuned from $[\mu, \omega, \beta]$: [-4,-1,-1]→[4,-1,-1] (see Eq. (4.15))

possible to obtain the 1-RDM's for systems on the order of 1000 particles. We can also use the Bogoliubov transform to obtain the spectra:

$$e(k) = \pm\sqrt{(2\omega\cos k + \mu)^2 + 4\beta^2 \sin^2 k} \quad -\pi \leq k \leq \pi \tag{4.16}$$

where k is a wave vector. This equation shows that there are two gapped regions separated by the gapless line $\mu = -2\omega$. The first and second regions occur (a) when $|\mu| > 2|\omega|$ and (b) when $2|\omega| > |\mu|$ with $\beta \neq 0$, respectively. Additionally, another gapless line can be found when $\beta = 0$ in (b). This bulk analysis does not reveal which region contains the MEMs, but these can be found by analyzing the RDMs in the various regions.

The 1-RDMs shown in Fig. 4.4a are from the path $\mu : 0 \to 4$, $\beta/\omega = 1$ for a system with 14 sites. In the regime of large (absolute value) μ all the way to slightly above ($\mu = 2.5$) there are no apparent edge states. The tridiagonal nature of the 1-RDMs also shows the relatively short correlation length scale of the system. However, immediately after the transition at $\mu = 2$, the edge states begin to appear, and more off-diagonal elements become populated indicating

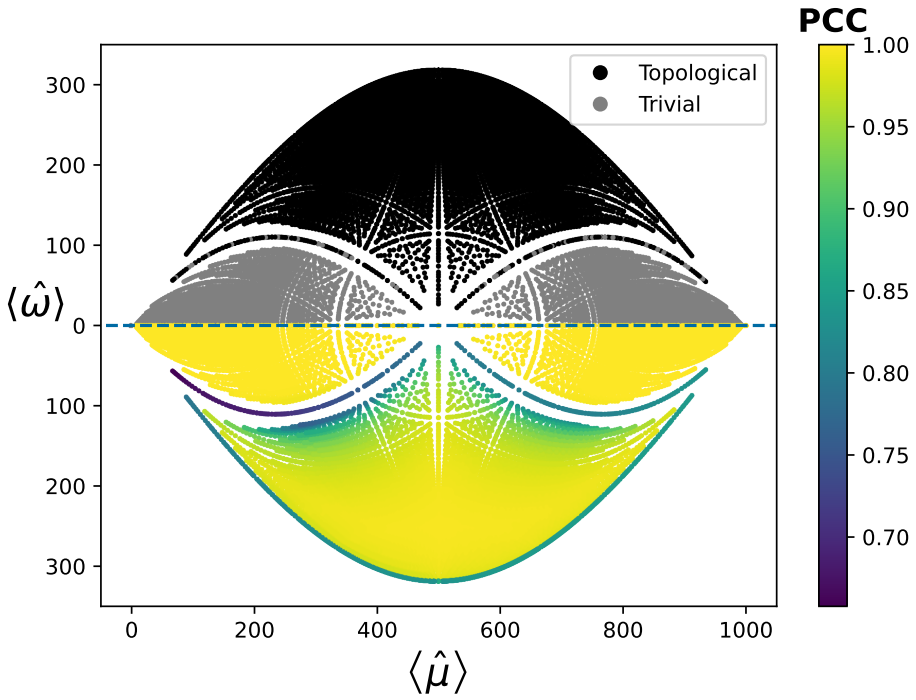

Figure 4.6: Slice of the Convex Set of the ground-state RDMs of the Kitaev Chain Model. For this 1000 site system, the coloring of this figure is split around the grey dashed line, where the upper-half is a binary coloring with gray or black indicating that a point lies in the trivial or topological regimes respectively. In the lower-half, the coloring corresponds to the color bar to the right and depicts the value of the PCC (see Eq. (4.5)) at any point. $\langle\hat{\omega}\rangle$ and $\langle\hat{\mu}\rangle$ refer to the expectation value of Hamiltonian terms found in Eq. (4.15)

the divergence of length scales near the critical point. Finally, deep in the topological region when $\mu = 0$, the edge states peak with an apex at $|.25|$ and the local tridiagonal nature of the bulk returns.

Figure 4.4b shows the sharpening of the transition through the PCC value for the 1-RDM as the particle number increases. The PCC value for the different system sizes changes rapidly, with larger systems converging to a structure that diverges at $\mu = 2$, serving as a signature of a topological transition. Additionally, the discontinuity due to the measurement of absolute values of the 1-RDM elements is seen at $\mu = 0$. Like the SSH model, the derivative of the PCC with respect to μ shows a peak at the $\mu = 2$ even at 10 particles, but unlike the SSH model a significant asymmetry with respect to μ has appeared. This is likely caused

by the rapid drop in particle number in regions with positive chemical potential values. Therefore, the edge modes contribute more to the overall behavior of the 1-RDM, being a larger percentage of the population of the system than in the particle-rich region.

This 1-RDM analysis, however, ignores the newly added 2-body correlation, which can be found in the 2-particle cumulant. The eigenvector associated with the largest eigenvalue of the cumulant (LCE) gives a picture of the most dominant 2-body effects in the system [31]. We define this eigenvector, g, as

$$\lambda_\Delta = g_{ij}^{\dagger\,2} \Delta_{kl}^{ij} g_{kl} \tag{4.17}$$

where λ_Δ is the largest eigenvalue of the 2-particle cumulant. Then by plotting g_{ij}, we recover a plot similar to the plot of the 1-RDM, but this plot contains spatial information about 2-body correlations in the system. Looking at Fig. 4.4c in the region with $\mu > 2$, the large number of off-diagonal terms indicates that the LCE contains information about long-range order in the system arising from the superconducting gap term in the Hamiltonian. Interestingly, the cumulant displays an identical transformation to the 1-RDM with the formation of edge states at $\mu < 2$. However unlike the 1-RDM, in the exact MEM limit, $\mu = 0$, the edge state is not completely isolated with some contributions coming from elements near the edges (i.e. $\langle \hat{a}_0^\dagger \hat{a}_{N-1}^\dagger \rangle$, ...). Looking at Fig. 4.4d, which is plotting the value of PCC for the LCE, aside from the 6 particle case, the values seem to follow a similar pattern to the RDM PCC curves. The peaks of the plots are lower due to the superconducting term generating nearly diagonal connections between the sites, but the linear correlation still experiences a significant drop near the phase transition. These rapid changes in correlation captured by this linear fitting can also be seen in a spectral analysis of the cumulant. The change in the eigenvalue of the LCE can be seen in Fig. 4.5. As a reflection of the divergence of correlation lengths when approaching the critical point, the eigenvalue changes very rapidly indicating that the two particle correlation is undergoing a dramatic change.

Analysis of a slice of the convex set of RDMs provides a map of the phases of the system.

Figure 4.6 displays a portion of the set for the 1000 site system mirrored around the horizontal dotted line, where above the line a binary color scale depicts the trivial region as gray and the topological as black, while below the line the color scale for the PCC can be seen in the color bar. The set was collected via sampling a grid in the Hamiltonian parameter space, which results in sparse regions that would likely be filled if the plot had been drawn with random sampling. This sparsity, however, is the result of the RDM moving rapidly near the phase transition, thus showing the divergence of the speed. This illustrates how speed information can be incorporated in the set picture. Finally, the value of the PCC also appears to fall at the site of the topological transition and near the bottom of the figure, reflecting the closing of the band gap that occurs at the transition and when $\beta = 0$. While it is not visible in this 2-D projection, there is also a significant gap in the RDMs between the yellow and green regions. This, of course, is not a topological phase transition, indicating that the PCC and speed might serve as a general indicator of when the gap is closing rather than a definitive sign of topological order.

4.5 Discussion and Conclusions

Characterization of topological phases is a vitally important step in the development of novel technologies like topological transistors, lasers, and quantum computers. In this article, we introduce the RDM approach to topological phase transitions, and analyze two simple systems exhibiting topological order. The first system, the SSH model, demonstrates that fermionic edge modes appear as easily recognizable features in the structure of the 1-RDM. Additionally, we see that the 1-RDM passes through a region with considerable off-diagonal character as the gap closes, reflecting the divergence of correlation length near critical points. The Pearson correlation coefficient (PCC), which spikes at the point of the gap closing, quantifies this off-diagonal quality by providing a simple metric, untethered from the Hamiltonian parameters, for identifying phase transitions.

The next system, the Kitaev chain, presents a novel challenge for RDM theory in the form of Majorana fermions. We show, however, that these fermions appear in the 1-RDM and that the transition exhibits the same off-diagonal spiking, seen in the PCC, as the SSH transition. Using this behavior, we reconstruct a picture of the full set of RDMs, which easily distinguishes between the phases without any reference to the underlying Hamiltonian, a useful trait for experimental settings. The Kitaev chain also contains non-number-conserving particle terms, which introduce higher order correlations to the system. This two-particle correlation is seen in the spectrum of the cumulant, and near the critical regions, the largest eigenvalue undergoes considerable shifts reflecting the divergence of correlation length scale.

These results demonstrate the power of the RDM approach to topological phase transitions, presenting a method, which is able to resolve multi-state phenomena like gap closing with ground-state information in an easily interpreted framework. This has many advantages not only for finite-sized theoretical modeling, but also for experiments or quantum computing simulations where calculation of the 1- and 2-RDMs requires considerably fewer measurements than complete determination of the wave function.

CHAPTER 5

EXACT ANSATZ OF FERMION-BOSON SYSTEMS FOR A QUANTUM DEVICE

Republished with permission from Samuel Warren, Yuchen Wang, Carlos L. Benavides-Riveros, and David A. Mazziotti. *Physical Review Letters* **133**, 8, 080202. Copyright American Physical Society 2024.

5.1 Abstract

We present an exact ansatz for the eigenstate problem of mixed fermion-boson systems that can be implemented on quantum devices. Based on a generalization of the electronic contracted Schrödinger equation (CSE), our approach guides a trial wave function to the ground state of any arbitrary mixed Hamiltonian by directly measuring residuals of the mixed CSE on a quantum device. Unlike density-functional and coupled-cluster theories applied to electron-phonon or electron-photon systems, the accuracy of our approach is not limited by the unknown exchange-correlation functional or the uncontrolled form of the exponential ansatz. To test the performance of the method, we study the Tavis-Cummings model, commonly used in polaritonic quantum chemistry. Our results demonstrate that the CSE is a powerful tool in the development of quantum algorithms for solving general fermion-boson many-body problems.

5.2 Introduction

Strong coupling with bosonic particles can drastically change many physical properties of electronic systems. For instance, when coupled with phonons, low-energy electronic excitations are strongly modified, influencing, as a result, the optical, thermodynamic, and transport properties of solids [197]. This electron-phonon coupling is also the source of the effective

attractive electronic interaction needed for conventional superconductivity [198, 146]. When coupled with light, emergent hybrid quantum states (known as polaritons) can catalyze or inhibit the reactive paths of chemical reactions [199, 200, 201, 202]. Both electron-phonon and electron-photon couplings lead to many fascinating chemical and technological applications, including spintronics [203], quantum information processing [204, 205], optical control of collective modes in solids [206], catalysis [207, 208, 209], solar power [210], or low energy lasing [211, 212, 213, 214].

Given the complexity of these entangled electron-boson systems, it is not surprising that their theoretical description usually relies on semi-empirical model Hamiltonians [215, 216, 217, 218]. However, a more complete understanding of the effects arising from mixed particle coupling requires quantitative methods that treat electronic and bosonic modes with equal theoretical rigor [219, 220, 221, 222]. For instance, to predict reaction pathways in polaritonic catalysis, it is important to port over electronic structure methods to mixed fermion-boson problems [223]. Current ab-initio approaches are mainly variants of density functional theory (DFT), but, while lattice dynamics and electron-photon coupling can be accounted for through perturbative [224, 225, 226] or quantum electrodynamics DFT [227, 223, 228], the unknown form of the corresponding exchange-correlation functionals for the electron-boson interaction limits the accuracy of both approaches [229, 230, 44]. Alternative methods can be found in a new class of coupled cluster (CC) algorithms. Originally developed for electrons [231, 232], CC has been extended to electron-phonon [233] and electron-photon [234, 51, 235] systems, where the key ingredient is an exponential ansatz believed to span a trial wave function across the most significant regions of the Hilbert space. Additionally, inspired by the prospects of quantum computing, there has been considerable development of CC's unitary form [52, 236, 237, 238]. In both cases the expressibility of the approach strongly depends on the quality of the ansatz and, from the quantum computational viewpoint, its Trotterized implementation is not always well defined [239].

Here we report the development of an alternative approach that gives an exact ansatz for ground and excited states of arbitrary electron-boson systems, overcoming the limitations of both DFT and CC methods. Our approach is based on an extension of the contracted Schrödinger equation (CSE) [240, 241, 242, 243, 244, 126, 245, 246, 247, 248, 249, 250, 251, 20, 21, 252, 253, 254, 255], known in the context of reduced density matrix theory for fermionic systems [122, 256, 257]. Our main result is an exact ansatz that can be implemented directly on quantum devices to find the eigenstates of arbitrary mixed particle Hamiltonians.

The Letter is structured as follows. First, we recap and extend the fermionic CSE to general many-body physics, including boson-fermion systems. We then discuss how the CSE ansatz can inform a quantum algorithm for finding the ground states of mixed particle systems. In the second part of the paper, we demonstrate the effectiveness of the CSE ansatz on the Tavis-Cummings model. Finally, we discuss potential future directions and the implications of our results.

5.3 Theory

Originally derived for fermionic systems, the *Contracted Schrödinger Equation* (CSE) reads [240, 241, 242, 243, 244, 126, 245, 246, 247, 248, 249, 250]:

$$\langle\Psi|\,\hat{a}_{i_1}^\dagger\hat{a}_{i_2}^\dagger\hat{a}_{k_2}\hat{a}_{k_1}\hat{H}\,|\Psi\rangle = E\;{}^2D_{k_1k_2}^{i_1i_2} \tag{5.1}$$

where $\hat{a}_i^\dagger$ and $\hat{a}_k$ are fermionic creation and annihilation operators on the ith and k^{th} sites, respectively, and

$${}^2D_{k_1k_2}^{i_1i_2} = \langle\Psi|\,\hat{a}_{i_1}^\dagger\hat{a}_{i_2}^\dagger\hat{a}_{k_2}\hat{a}_{k_1}|\Psi\rangle \tag{5.2}$$

is the two-body reduced density matrix (RDM). Nakatsuji's theorem states that the CSE (5.1) is satisfied if and only if the corresponding N-body preimage of ${}^2D_{k_1k_2}^{i_1i_2}$ satisfies the usual Schrödinger equation (SE) [240, 249].

We now extend the CSE to mixed fermion-boson systems and show that Nakatsuji's theorem also holds for those systems. Let's first define a general electron-boson density operator

$$\hat{\Gamma}^{i_1...i_q,j_1...j_s}_{k_1...k_r,l_1...l_t} = \hat{a}^\dagger_{i_1}...\hat{a}^\dagger_{i_q}\hat{a}_{k_r}...\hat{a}_{k_1}\hat{b}^\dagger_{j_1}...\hat{b}^\dagger_{j_s}\hat{b}_{l_t}...\hat{b}_{l_1} \equiv \hat{\Gamma}^{\boldsymbol{i},\boldsymbol{j}}_{\boldsymbol{k},\boldsymbol{l}}, \tag{5.3}$$

where $\hat{b}^\dagger_j$ and $\hat{b}_l$ are bosonic creation and annihilation operators. Here i_m and k_m (j_m and l_m) run over the different fermionic (bosonic) indices, and we use the compact notation $\boldsymbol{i} = (i_1, ..., i_q)$, $\boldsymbol{k} = (k_1, ..., k_r)$, $\boldsymbol{j} = (j_1, ..., j_s)$ and $\boldsymbol{l} = (l_1, ..., l_t)$.

The density operator (5.3) allows us to define concisely a general fermion-boson (fb) Hamiltonian:

$$\hat{H}_{fb} = \sum_{\boldsymbol{ik},\boldsymbol{jl}} h^{\boldsymbol{i},\boldsymbol{j}}_{\boldsymbol{k},\boldsymbol{l}} \hat{\Gamma}^{\boldsymbol{i},\boldsymbol{j}}_{\boldsymbol{k},\boldsymbol{l}}. \tag{5.4}$$

We then multiply the corresponding fermion-boson SE, i.e., $\hat{H}_{fb}\left|\Psi\right\rangle = E\left|\Psi\right\rangle$, on the left by $\left\langle\Psi\right|\hat{\Gamma}^{\boldsymbol{i},\boldsymbol{j}}_{\boldsymbol{k},\boldsymbol{l}}$ to obtain a *generalized* CSE:

$$\left\langle\Psi\right|\hat{\Gamma}^{\boldsymbol{i},\boldsymbol{j}}_{\boldsymbol{k},\boldsymbol{l}}\hat{H}_{fb}\left|\Psi\right\rangle = ED^{\boldsymbol{i},\boldsymbol{j}}_{\boldsymbol{k},\boldsymbol{l}}, \tag{5.5}$$

where $D^{\boldsymbol{i},\boldsymbol{j}}_{\boldsymbol{k},\boldsymbol{l}} = \left\langle\Psi\right|\hat{\Gamma}^{\boldsymbol{i},\boldsymbol{j}}_{\boldsymbol{k},\boldsymbol{l}}\left|\Psi\right\rangle$ is a *generalized* RDM of the electron-boson system. Multiplying both sides of the generalized CSE (5.5) by the elements of the reduced Hamiltonian matrix $h^{\boldsymbol{i},\boldsymbol{j}}_{\boldsymbol{k},\boldsymbol{l}}$ and summing over all indices yields

$$\sum_{\boldsymbol{ik},\boldsymbol{jl}} h^{\boldsymbol{i},\boldsymbol{j}}_{\boldsymbol{k},\boldsymbol{l}} \left\langle\Psi\right|\hat{\Gamma}^{\boldsymbol{i},\boldsymbol{j}}_{\boldsymbol{k},\boldsymbol{l}}\hat{H}_{fb}\left|\Psi\right\rangle = E\sum_{\boldsymbol{ik},\boldsymbol{jl}} h^{\boldsymbol{i},\boldsymbol{j}}_{\boldsymbol{k},\boldsymbol{l}} D^{\boldsymbol{i},\boldsymbol{j}}_{\boldsymbol{k},\boldsymbol{l}}. \tag{5.6}$$

The sum on the right-hand side is equal to the energy, making the expression equal to E^2. Thus, the equation can be rewritten as the energy variance

$$\left\langle\Psi\right|\hat{H}^2_{fb}\left|\Psi\right\rangle - \left\langle\Psi\right|\hat{H}_{fb}\left|\Psi\right\rangle^2 = 0, \tag{5.7}$$

which, as a stationary condition for the wave function, is equivalent to the SE. Therefore, the set of solutions to Eq. (5.5) must be the same as the solutions to the electron-boson SE. This derivation shows that the minimal RDM necessary to satisfy both the CSE and SE will have the same degrees of freedom as the corresponding many-body Hamiltonian. This is reminiscent of the standard electronic structure problem where a nondegenerate electronic ground-state wavefunction maps to a unique 2-electron RDM, which, as a result, has enough information to build higher-order RDMs and the exact wavefunction [123].

The CSE (5.5) can be further decomposed into Hermitian and anti-Hermitian parts:

$$\langle\Psi|\,\hat{\Gamma}(\hat{H}_{fb}-E))\,|\Psi\rangle = \frac{1}{2}\big(\,\langle\Psi|\,[\hat{\Gamma},\hat{H}_{fb}]\,|\Psi\rangle + \langle\Psi|\,\{\hat{\Gamma},\hat{H}_{fb}-E\}\,|\Psi\rangle\,\big), \tag{5.8}$$

where $[\cdot,\cdot]$ and $\{\cdot,\cdot\}$ are the usual commutator and anticommutator. As described in several prior works for the electronic problem, this decomposition can be used to converge to stationary states either through classical [251, 20, 21, 252, 253, 254, 255, 148] or quantum [65, 247, 258, 259, 260, 261, 262] computing methods.

On modern quantum devices, the *Contracted Quantum Eigensolver* (CQE) algorithm measures the total residual of Eq. (5.8) for trial wave functions. Such a residual can then be used to guide a sequence of trial wave functions toward the ground (or an eigen-) state by iteratively applying a sequence of exponential transformations. The scheme is agnostic to the statistics of the system and has already been applied both for fermions and bosons with significant success [247, 258, 259, 260, 261, 262]. Here, we will show that the CQE algorithms also provide a simple methodology for resolving the ground state in mixed fermion-boson systems.

Our scheme is as follows: at iteration $(n+1)$ the wave function results from two separate exponential transformations of the wave function at iteration (n):

$$|\Psi^{(n+1)}\rangle = \exp(\eta_B\hat{B}^{(n)})\exp(\eta_A\hat{A}^{(n)})\,|\Psi^{(n)}\rangle\,, \tag{5.9}$$

where

$$\hat{A}^{(n)} = \sum_{\boldsymbol{ik},\boldsymbol{jl}} A^{(n)}_{\boldsymbol{ik},\boldsymbol{jl}} \hat{\Gamma}^{\boldsymbol{i},\boldsymbol{j}}_{\boldsymbol{k},\boldsymbol{l}} \tag{5.10}$$

is an anti-Hermitian operator,

$$\hat{B}^{(n)} = \sum_{\boldsymbol{ik},\boldsymbol{jl}} B^{(n)}_{\boldsymbol{ik},\boldsymbol{jl}} \hat{\Gamma}^{\boldsymbol{i},\boldsymbol{j}}_{\boldsymbol{k},\boldsymbol{l}} \tag{5.11}$$

is a Hermitian one, and η_A and η_B can be interpreted as learning rates of the algorithm.

Notice that if the unitary operator $\exp(\eta_A \hat{A}^{(n)})$ is applied to a normalized wave function $|\Psi^{(n)}\rangle$, the total energy of the transformed state is (in leading order of the parameter η_A): $\mathcal{E}_{n+1} = \mathcal{E}_n + \eta_A \langle\Psi^{(n)}| [\hat{H}_{fb}, \hat{A}^{(n)}] |\Psi^{(n)}\rangle + \mathcal{O}(\eta_A^2)$ where $\mathcal{E}_n = \langle\Psi^{(n)}| \hat{H}_{fb} |\Psi^{(n)}\rangle$. As a result, the anti-Hermitian portion of Eq. (5.8) can be used as a residual to find the optimal operator at each step, and the anti-Hermitian parameters can be updated as follows:

$$A^{(n)} = \langle\Psi^{(n)}| [\hat{\Gamma}, \hat{H}_{fb}] |\Psi^{(n)}\rangle \,. \tag{5.12}$$

These parameters generate the unitary $\exp(\eta_A \hat{A}^{(n)})$. In turn, η_A can be selected to minimize the expectation energy of the resulting state $|\Phi^{(n)}\rangle = \exp(\eta_A \hat{A}^{(n)}) |\Psi^{(n)}\rangle$. Quite remarkably, many well-known canonical transformations of mixed fermion-boson systems are exactly recovered when only the anti-Hermitian part of the ansatz is used. This is the case, for instance, of the Lang-Firsov transformation for the Holstein Hamiltonian [263] or the Schrieffer-Wolff transformation for the Anderson model [264]. As already suggested for the electronic case [148], this means that the anti-Hermitian part of the CSE converges to the appropriate canonical transformation of the respective problem.

Next, the Hermitian portion of the residual is measured with respect to the updated

(normalized) vector $|\Phi^{(n)}\rangle$.

$$B^{(n)} = \langle\Phi^{(n)}| \{\hat{\Gamma}, \hat{H}_{fb} - E^{(n)}\} |\Phi^{(n)}\rangle\,, \tag{5.13}$$

where $E^{(n)} = \langle\Phi^{(n)}| \hat{H}_{fb} |\Phi^{(n)}\rangle$. The resulting Hermitian operator $\hat{B}^{(n)}$ generates the non-unitary $\exp(\eta_B \hat{B}^{(n)})$ where η_B is selected to minimize the energy of $|\Psi^{(n+1)}\rangle$. Implementing non-unitary operators on quantum devices is an active field of research [265, 266] and has resulted in the development of several methods such as quantum imaginary-time evolution [267, 268]. Prior implementations of the fermionic CQE have utilized dilation techniques similar to the Sz.-Nagy dilation [247], but the CQE is agnostic to the particular technique used to accomplish non-unitary transformations. Here, we exactly map the non-unitary transformation to a unitary transformation on a classical device, allowing us to focus on the effectiveness of the CSE ansatz for mixed systems.

To study the numerical performance of the algorithm, we use the *Tavis-Cummings model* (TC). This is a prototypical mixed fermion-boson system that attempts to capture the behavior of polaritons in a wide range of coupling regimes [269, 41, 40, 270, 271]. The model is comprised of N two-level fermionic systems coupled to a bosonic mode, making it analogous to situations found in polaritonic chemistry where molecules are bound in cavities [208, 201, 272, 221] or solid-state intersubband devices [273, 274]. The TC Hamiltonian is written as follows:

$$\hat{H} = \omega_b \hat{b}^\dagger \hat{b} + \sum_{i=1}^{N} \left[\omega_f \hat{a}_{i+}^\dagger \hat{a}_{i+} + g_c\big(\hat{a}_{i+}^\dagger \hat{a}_{i-} \hat{b} + \hat{a}_{i-}^\dagger \hat{a}_{i+} \hat{b}^\dagger\big)\right], \tag{5.14}$$

with the fermionic subscripts indicating the excited (+) and ground (−) orbitals in the ith two-level system, and where ω_b, ω_f, and g_c describe the angular frequency of the bosonic mode, the transition frequency of the fermionic modes, and the coupling between the bosonic mode and the fermionic bath, respectively.

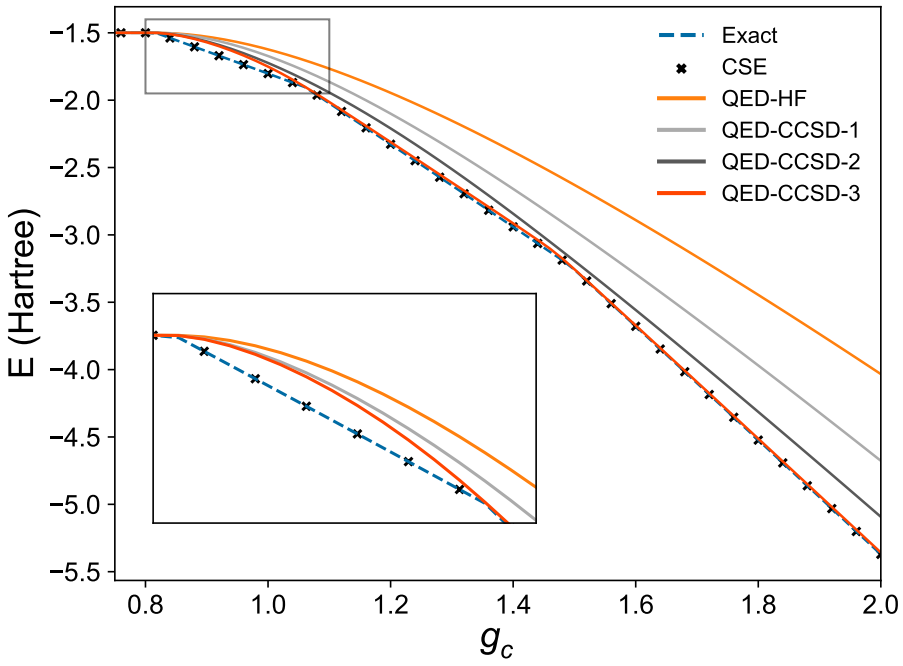

Figure 5.1: CSE and QED-CCSD energies for the 3 fermion Tavis-Cummings model with increasing coupling. The Hamiltonian parameters from Eq. (5.14) were fixed as $(\omega_b, \omega_f) = (2, 0.5)$ while g_c is varied as shown along the x-axis. The QED-CCSD-n methods are named according to the convention used in Ref. [51].

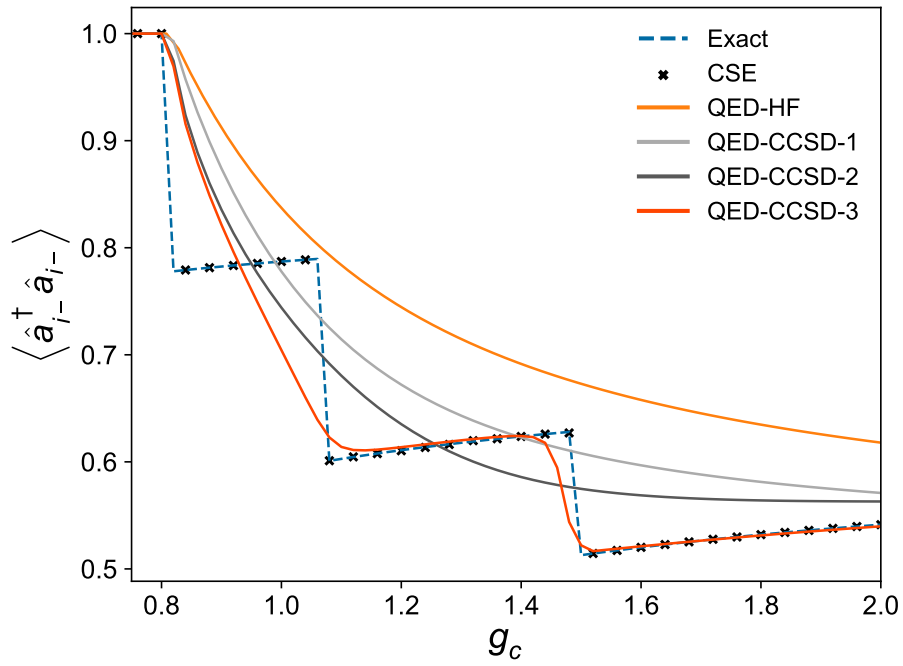

Figure 5.2: CSE and QED-CCSD predicted ground fermionic orbital populations with increasing coupling in the 3-fermion Tavis-Cummings Model.

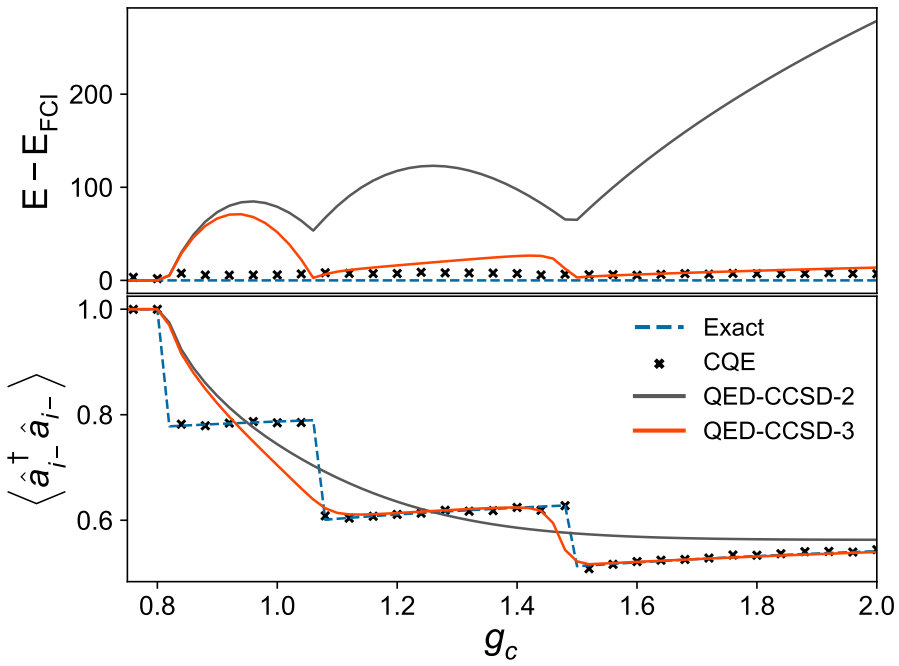

Figure 5.3: CQE and QED-CCSD ground-state energy and fermionic orbital population with increasing coupling. The y-axis of the energy shows the absolute error in mHartree.

5.4 Results

We first compare the CQE ground-state results to those obtained from the mixed fermion-boson quantum electrodynamics coupled cluster (QED-CC) methods for the TC model. Those are named such that QED-CC(SD)-n refers to coupled-cluster with single and double fermionic cluster terms combined with bosonic and mixed cluster terms containing up to n bosonic creation operators [51].

Fig. 5.1 depicts the ground-state energies predicted by various methods for the 3-site TC model as the coupling strength increases, entering well into the ultra-strong regime. The QED-CC methods capture the general trend of the energies but do not align with any section of the exact energy curve, including the high-level QED-CCSD-3, which is the most accurate QED-CCSD method possible in this coupling regime due to the maximum bosonic population of 3. This suggests that QED-CCSD-3 would begin to fail again in the stronger coupling limit when the maximum bosonic population increases to 4 or larger. Additionally,

despite being the best CCSD method in this region, QED-CCSD-3 is unable to predict the transition in the weak coupling limit seen in the zoomed-in section of the figure due to the omission of the triple cluster operator. The CSE, however, is able to accurately reproduce the exact energy regardless of coupling strength. Notice that this accuracy is achieved while only ever measuring the residual with the same density operators that appear in the TC Hamiltonian, while QED-CC must include all possible excitations to be accurate. Therefore, while the number of bosonic and mixed cluster terms remains fixed for the CQE, for the QED-CC methods it will grow with the coupling strength or, equivalently, the maximum boson population.

Fig. 5.2 demonstrates how QED-CC methods fail to capture both the quantitative and qualitative properties of the TC model. The plot shows the predicted population of the lower energy level in any of the fermionic two-level subsystems, which, due to symmetry, are the same. The QED-CC methods up to QED-CCSD-2 approximate the discontinuous population changes with successively better least squares errors, but fail to capture any of the stair-stepping behavior caused by actual level crossings. QED-CCSD-3 smoothes out the final two stair steps, but completely misses the first, as could be predicted from its failure in the prior figure. The CSE method, however, exactly recovers the populations, despite needing to resolve nearly degenerate states at the level crossings. The failure of CC to resolve level crossings [275] and the success of the CSE highlight the importance of the particular combination of Hermitian and anti-Hermitian contributions present in the CSE ansatz.

Finally, Fig. 5.3 presents the results from the CQE algorithm run on an ideal quantum device simulator and the ones from the classical QED-CCSD methods. The CQE algorithm reproduces the energies with an average error of 7 mhartree with a standard deviation of 1 mhartree, indicating that the error is uniform regardless of the distance from the level crossings. This is in contrast to the CC methods where the error exhibits significant fluctu-

ations. The CQE recovers the ground orbital populations near the degeneracies despite not exactly recovering the energy. These results demonstrate that despite sampling error, the CQE is able to outperform some of the most popular classical algorithms for mixed-particle systems.

5.5 Conclusions

Based on a generalization of the electronic CSE, we present an exact ansatz for mixed quantum fermion-boson systems. Our numerical results on the Tavis-Cumming model demonstrate the power of the CSE ansatz. While CC methods require constantly increasing the number of terms in the exponential to be accurate in different coupling regimes, the CSE is always exact and the required number of terms exactly matches the density operators present in the Hamiltonian. Additionally, the CQE demonstrates how the CSE can be applied on a quantum device, and can outperform cutting-edge classical algorithms. This Letter leaves many avenues for future works, whether it be the development of classical computing algorithms for mixed particle systems that leverage the CSE or the application of the CQE on real quantum devices. Furthermore, since the ansatz can be equally used for any eigenstate [276], the computation of exact excited states in polaritonic quantum chemistry is also a promising future direction.

CHAPTER 6

QUANTUM ALGORITHM FOR POLARITONIC CHEMISTRY BASED ON AN EXACT ANSATZ

Republished with permission from Samuel Warren, Yuchen Wang, Carlos L. Benavides-Riveros, and David A. Mazziotti, *Quantum Science and Technology* **10**, 2, 02LT02. Copyright © 2024 IOP Publishing.

6.1 Abstract

Cavity-modified chemistry uses strong light-matter interactions to modify the electronic properties of molecules in order to enable new physical phenomena such as novel reaction pathways. As cavity chemistry often involves critical regions where configurations become nearly degenerate, the ability to treat multireference problems is crucial to understanding polaritonic systems. In this Letter, we show through the use of a unitary *ansatz* derived from the anti-Hermitian contracted Schrödinger equation that cavity-modified systems with strong correlation, such as the deformation of rectangular H_4 coupled to a cavity mode, can be solved efficiently and accurately on a quantum device. In contrast, while our quantum algorithm can be made formally exact, classical-computing methods as well as other quantum-computing algorithms often yield answers that are both quantitatively and qualitatively incorrect. Additionally, we demonstrate the current feasibility of the algorithm on near intermediate-scale quantum hardware by computing the dissociation curve of H_2 strongly coupled to a bosonic bath.

6.2 Introduction

Polaritonic chemistry is a young discipline that exploits confined electromagnetic field modes to enable chemical processes that are not possible in bare materials [221, 277, 222]. It has

been shown, for example, that polaritons can modify photochemical reaction rates [278, 279], transition rates between different spin multiplets [280] or charge transfer in chemical reactions [281, 282]. Hybridized light-matter states are also crucial for exploring quantum states of matter or quantum phase transitions [283, 284] and are central in the emergent field of cavity quantum materials [285, 206]. From a theoretical viewpoint, polaritonic systems exhibit an intrinsic strong multireference character [286] and require an equal quantum-mechanical treatment of both bosonic and fermionic statistics. It is thus no surprise that studying molecular polaritonic systems is a very demanding computational task.

Recently, quantum-computing methods for solving electronic structure problems have emerged as promising computational tools to combat the curse of dimensionality [56, 57, 58]. The most prominent algorithm proposed for use on noisy intermediate scale quantum (NISQ) devices is the variational quantum eigensolver (VQE), often using a unitary coupled cluster (UCC) ansatz [61]. These methods, however, tend to inherit some of the pitfalls of classical coupled cluster methods [62, 63, 52], namely, an inability to treat static correlation [64] and the need for truncation in the number of exponential operators [239]. In addition, the extension of the ansatz to arbitrary systems (e.g., where bosonic modes are present) is not always straightforward [234, 51]. In parallel, methods derived from the contracted Schrödinger equation (CSE) forming the set of algorithms known as the Contracted Quantum Eigensolvers (CQE) have been shown to find exact ground and excited states for fermionic [65, 247, 276] and bosonic [262] systems with an ansatz whose underlying structure is universal. A subset of these algorithms focusing on the anti-Hermitian portion of the CSE, known as the ACSE, are particularly promising on NISQ devices [259].

Originally derived for fermionic systems [249, 248, 240, 241, 242, 243, 244, 126], the CSE was recently extended to mixed Boson-Fermion systems [287]. The main result of that extension is an exact ansatz that can be implemented directly on quantum devices to find eigenstates of arbitrary mixed-particle Hamiltonians. Remarkably, the CSE uniquely allows

the ansatz to have the same degrees of freedom as the original many-body Hamiltonian (e.g., a purely two-body ansatz for the traditional electronic structure problem). Here, based on those previous results, we present a quantum algorithm for molecular polaritonic chemistry. We show that cavity-modified systems exhibiting strong quantum correlation, such as the deformation of rectangular H_4 coupled to a cavity mode, can be accurately solved by using the simple unitary ACSE ansatz. Additionally, to demonstrate the current feasibility of the algorithm, we compute the dissociation curve of molecular hydrogen coupled to a bosonic bath on NISQ hardware.

The Letter is structured as follows. First, we discuss how the ACSE naturally adapts to arbitrary quantum many-body systems. Next, we introduce the non-relativistic Pauli-Fierz Hamiltonian and discuss how our algorithm works for this problem as well as its favorable computational and measurement scaling on a quantum device. In the latter half of the paper, we will compare the results of the ACSE to quantum electrodynamics coupled cluster (QED-CC). We will also demonstrate the effectiveness of our ansatz on a real quantum device. Finally, we will discuss potential future directions and implications for our results.

6.3 Theory

6.3.1 Contracted Schrödinger Equation

Before studying a polaritonic system we review the fully general version of the CSE [240, 256] which can be used for arbitrary quantum many-body systems. We define a many-body M-term Hamiltonian:

$$\hat{H} = \sum_{\updownarrow=1}^{M} f_{\updownarrow} \hat{h}_{\updownarrow}, \tag{6.1}$$

where $\{f_{\updownarrow}\}$ is the set of Hamiltonian's parameters and $\hat{h}_{\updownarrow}$ is a general many-body operator. The stationary state problem or the (time-independent) Schrödinger equation reads: $\hat{H}\,|\Psi_m\rangle = E_m\,|\Psi_m\rangle$. After multiplying on the left by $\langle\Psi_m|\,\hat{h}_{\updownarrow}$, one obtains the CSE:

$$\langle\Psi_m|\,\hat{h}_{\updownarrow}(\hat{H} - E_m)\,|\Psi_m\rangle = 0\,. \tag{6.2}$$

The equivalence of this equation and the standard Schrödinger equation can be proved by multiplying Eq. (6.2) by the parameter $f_{\updownarrow}$ and summing up the resulting expression over the indices $\updownarrow$, which yields the energy variance equation $\langle\Psi_m|\,\hat{H}^2\,|\Psi_m\rangle = E_m^2$ [240, 256]. In the case of electronic systems ($\updownarrow \equiv ijkl$) the Hamiltonian (6.1) is

$$\hat{H}_e = \sum_{ijkl} f_{ijkl}\,\hat{a}_i^\dagger\hat{a}_j^\dagger\hat{a}_l\hat{a}_k\,, \tag{6.3}$$

where $\hat{a}_i$ and $\hat{a}_i^\dagger$ are fermionic creation and annihilation operators, respectively, and the relevant many-body operators, $\hat{h}_{\updownarrow}$, of Eq. (6.1) are two-particle terms only. Thus, the CSE (6.2) for the electronic problem becomes:

$$\langle\Psi_m|\,\hat{a}_i^\dagger\hat{a}_j^\dagger\hat{a}_l\hat{a}_k(\hat{H}_e - E_m)\,|\Psi_m\rangle = 0. \tag{6.4}$$

It is instructive to decompose the CSE (6.2) into two expectation values, containing an anti-commutator $\{\cdot,\cdot\}$ and a commutator $[\cdot,\cdot]$:

$$\langle\Psi_m|\,\{\hat{h}_{\updownarrow}, \hat{H} - E_m\}\,|\Psi_m\rangle + \langle\Psi_m|\,[\hat{h}_{\updownarrow}, \hat{H}]\,|\Psi_m\rangle = 0. \tag{6.5}$$

As described in several prior works for the electronic problem, this decomposition can be used to optimize a sequence of exponential (unitary and anti-unitary) ansätze that converge trial wave functions to the exact stationary states either through classical [251, 20, 21, 252,

253, 254, 255, 148] or quantum [65, 247, 258, 259, 260, 261, 262, 287] computing methods. Furthermore, the simultaneous presence of anti-unitary and unitary operators makes the ansatz a very flexible one that can contain dissipative and non-dissipative terms [247]. Interestingly, while similar operator combinations are the focus of recent efforts in developing variational ansätze for ground-state preparation [288], they emerge naturally in the CSE framework.

Although the CSE is fully general, so far it has been barely used beyond the realm of electronic structure theory [262, 287]. We now apply the CSE framework to tackle the eigenstates of the Pauli-Fierz Hamiltonian.

6.3.2 Pauli-Fierz Hamiltonian

The nonrelativistic Pauli-Fierz (PF) Hamiltonian describes the interaction of a molecular system with a cavity mode through the coupling of the electronic dipole moment to a bosonic field, and attempts to model the physics of, for example, electronic systems in mirrored cavities [219, 45, 44, 289]. Many-body methods such as quantum electrodynamics Hartree-Fock (QED-HF), density functional theory (QEDFT/QED-DFT) [46, 43, 47, 48, 49, 50], and coupled cluster (QED-CC) [51, 290, 235] have been benchmarked on this approximate Hamiltonian. The PF Hamiltonian, in the length gauge with the dipole approximation [42, 43], is not in general restricted to a single bosonic mode; however, we will only consider the single-mode case as described by:

$$\hat{H}_{\mathrm{PF}} = \hat{H}_e + \omega \hat{b}^\dagger \hat{b} - \sqrt{\frac{\omega}{2}} \left(\lambda \cdot \hat{\mu}\right) \left(\hat{b}^\dagger + \hat{b}\right) + \frac{1}{2} \left(\lambda \cdot \hat{\mu}\right)^2 , \tag{6.6}$$

where the first term, $\hat{H}_e$, is the traditional electronic Hamiltonian as seen in Eq. (6.3). The second term describes the energy of the cavity where ω is the fundamental frequency of the bosonic cavity mode and $\hat{b}$ and $\hat{b}^\dagger$ are the bosonic annihilation and creation operators,

respectively. The third term depicts the coupling between the molecular dipole and the cavity where $\hat{\mu}$ is the molecular dipole moment, and λ is the coupling vector. Finally, the last term is the dipole self-energy. An excellent introduction to QED-many-body methods and the coherent-state form of the PF Hamiltonian, used for construction of the Hartree-Fock reference state, can be found in Ref. [44].

The CSE for general mixed Fermi-Boson systems was derived by us in Ref. [287] and can be applied to the PF's ground state to generate the following set of CSEs:

$$\langle\Psi|\,\hat{\Gamma}^{ij}_{kl}(\hat{H}_{\mathrm{PF}} - E)\,|\Psi\rangle = 0 \tag{6.7a}$$

$$\langle\Psi|\,\hat{\Delta}^{i}_{j}(\hat{H}_{\mathrm{PF}} - E)\,|\Psi\rangle = 0 \tag{6.7b}$$

$$\langle\Psi|\,\hat{b}^{\dagger}\hat{b}\,(\hat{H}_{\mathrm{PF}} - E)\,|\Psi\rangle = 0, \tag{6.7c}$$

where $\hat{\Gamma}^{ij}_{kl} = \hat{a}^{\dagger}_{i}\hat{a}^{\dagger}_{j}\hat{a}_{l}\hat{a}_{k}$ and $\hat{\Delta}^{i}_{j} = (\hat{b}^{\dagger} + \hat{b})\hat{a}^{\dagger}_{i}\hat{a}_{j}$ are, respectively, two-body fermionic and mixed (i.e., Fermi-Bose) density operators. We reiterate that, since the CSE has the same set of solutions as the Schrödinger equation, Eqs. (6.7) are satisfied by the exact ground state of the PF Hamiltonian. Furthermore, as explained in Eq. (6.5), the set of CSEs (6.7) can be further decomposed into a Hermitian and an anti-Hermitian part, the latter comprising the following set of equations:

$$\langle\Psi|\,[\hat{\Gamma}^{ij}_{kl}, \hat{H}_{\mathrm{PF}}]\,|\Psi\rangle = 0 \tag{6.8a}$$

$$\langle\Psi|\,[\hat{\Delta}^{i}_{j}, \hat{H}_{\mathrm{PF}}]\,|\Psi\rangle = 0. \tag{6.8b}$$

The anti-Hermitian counterpart to Eq. 6.7c vanishes and thus we do not consider it here. We call this anti-Hermitian subset of equations, the ACSE. Formally, the ACSE is not exact because it can be satisfied by a wave function that does not satisfy the CSE (or the Schrödinger equation) [148, 20]. Model spin systems in which the ACSE possesses spurious solutions are discussed in Refs. [148, 247]. Practically, however, we find that the solution of

the ACSE converges to the FCI wave function for molecules treated on noiseless quantum simulators [65, 247, 258, 259, 260]. Because of this agreement with FCI, we apply only the ACSE part of the CSE in the Results section.

6.3.3 Pauli-Fierz Contracted Quantum Eigensolver

On modern quantum devices, the CQE algorithm measures the total residuals of Eqs. (6.7) for quantum states. Such a residual can then be used to guide a sequence of trial wave functions toward an *exact* eigenstate by iteratively applying a sequence of exponential transformations. Since our scheme is agnostic to the statistics of the system [247, 258, 259, 260, 261, 262], we apply it here to the PF Hamiltonian. To resolve its ground and excited states, we focus on a subset of the CQE algorithms, the ACSE, because it provides a simple and practical implementation on quantum hardware.

Our scheme is as follows: at iteration $(n+1)$ the wave function results from an exponential transformation of the wave function at iteration (n) [287]:

$$|\Psi^{(n+1)}\rangle = \exp(\eta_B \hat{B}^{(n)}) \exp(\eta_A \hat{A}^{(n)}) \, |\Psi^{(n)}\rangle \,, \tag{6.9}$$

where

$$\hat{A}^{(n)} = \sum_{ik,jl} A^{(n)}_{ik,jl} \hat{\Gamma}^{ij}_{kl} \quad \text{and} \quad \hat{B}^{(n)} = \sum_{i,j} B^{(n)}_{ij} \hat{\Delta}^{i}_{j} \,. \tag{6.10}$$

Here $\hat{A}^{(n)}$ and $\hat{B}^{(n)}$ are the anti-Hermitian fermionic and mixed operators, respectively. The parameters η_A and η_B can be interpreted as learning rates of the algorithm and can be set equal to simplify the optimization procedure. Faster convergence, however, is achieved when both learning rates are optimized independently.

Notice that if the unitary $e^{\eta_A \hat{A}^{(n)}}$ is applied to a (normalized) wave function $|\Psi^{(n)}\rangle$, the total energy of the transformed state is (in leading order of η_A): $\mathcal{E}_{n+1} = \mathcal{E}_n + \eta_A \, \langle \Psi^{(n)}| \, [\hat{H}_{\mathrm{PF}}, \hat{A}^{(n)}] \, |\Psi^{(n)}\rangle +$

$\mathcal{O}(\eta_A^2)$ where $\mathcal{E}_n = \langle\Psi^{(n)}|\,\hat{H}_{\mathrm{PF}}\,|\Psi^{(n)}\rangle$. As a result, the anti-Hermitian portion of the CSE, seen in Eqs. (6.8), can be used as a residual to find the optimal operator at each step, and the anti-Hermitian parameters can be updated as follows:

$$A^{(n)} = \langle\Psi^{(n)}|\,[\hat{\Gamma}, \hat{H}_{\mathrm{PF}}]\,|\Psi^{(n)}\rangle \tag{6.11a}$$

$$B^{(n)} = \langle\Psi^{(n)}|\,[\hat{\Delta}, \hat{H}_{\mathrm{PF}}]\,|\Psi^{(n)}\rangle\,. \tag{6.11b}$$

Measurement of the fermionic residual can be done through an approximate method that only requires the measurement of two-body operators, instead of the three-body operators needed for the exact residual, by measuring,

$$A^{(n)}_{ik,jl} = \frac{1}{2i\delta}\left(\langle+_n|\,\hat{\Gamma}^{ij}_{kl}\,|+_n\rangle - \langle-_n|\,\hat{\Gamma}^{ij}_{kl}\,|-_n\rangle\right) + \mathcal{O}(\delta^2) \tag{6.12}$$

where $|\pm_n\rangle = e^{\pm i\delta\hat{H}_{\mathrm{PF}}}\,|\Psi^{(n)}\rangle$ [65]. Tomography of the *exact* mixed particle residuals $B^{(n)}_{ij}$, on the other hand, only requires measurement of two-body fermionic operators. Thus the number of measurements for both the fermionic and mixed residuals scale as $\mathcal{O}(r^4)$, where r is the number of orbitals. However, utilizing anti-/symmetries of the reduced density matrix as well as techniques like clique covering of Pauli words considerably lowers the scaling as many of the mixed residual terms qubit-wise commute with the fermionic terms [291].

It is worth emphasizing the key differences between our algorithm and VQE-based approaches, adapted to the many-body problem. ADAPT-VQE, for instance, iteratively builds a variational ansatz for the wave function by selecting from a predefined pool of operators [292]. The ansatz is often described as being a form of coupled cluster, but the stationarity condition of the ansatz does not produce the coupled cluster equations [243]. In fact, the ansatz is a subset of the ACSE ansatz with its stationarity generating a subset of the ACSE [251, 20]. The ADAPT-VQE algorithm's key feature is its operator selection process: (*i*) in each step the operator with the largest gradient is added to the left end of the ansatz,

accompanied by a new variational parameter and (*ii*) all parameters are then re-optimized and the process is repeated until the gradient vector falls below a specified threshold ε [292]. TETRIS-ADAPT-VQE, a recent improvement of the method, also includes at each step the operator with the largest gradient, that is not supported by the qubits already present in the ansatz [293].

The main differences of the ADAPT-VQE algorithm from the CQE are (1) its reliance upon a predefined pool of operators and (2) its reoptimization of all variational parameters at each iteration [65, 258, 259, 260, 261, 262, 247]. First, the CQE works with a potentially infinite pool of operators at each iteration with the pool being defined by the residual matrix of the CSE (or ACSE) [259, 247]. The CQE can either use the entire pool at each iteration or a more limited pool like the ADAPT-VQE, as in the recently proposed shadow CSE ansatz [294] inspired by shadow tomography. Second, unlike the ADAPT-VQE in which all parameters must be optimized to satisfy the global variational principle, the optimal operator in the CQE is selected at each iteration in the context of a *local* optimization method such that reoptimization of the parameters from previous iterations is unnecessary; e.g., in gradient descent, the optimal operator is the gradient of the CSE (or ACSE) ansatz [68]. The CQE is able to optimize only the parameters at a given iteration because such a local optimization in the CSE ansatz is sufficient to imply the CSE and hence, the Schrödinger equation at the minimum. [148, 246].

6.4 Results

We first discuss the predicted results from the ACSE, QED-CC, and QED-FCI for the rectangular conformation of H_4, as it is distorted into and out of the square geometry. The coupled cluster methods are named such that QED-CCSD-n refers to coupled-cluster with single and double fermionic cluster terms combined with bosonic and mixed cluster terms containing up to n bosonic creation operators [51]. In line with this convention, we will write

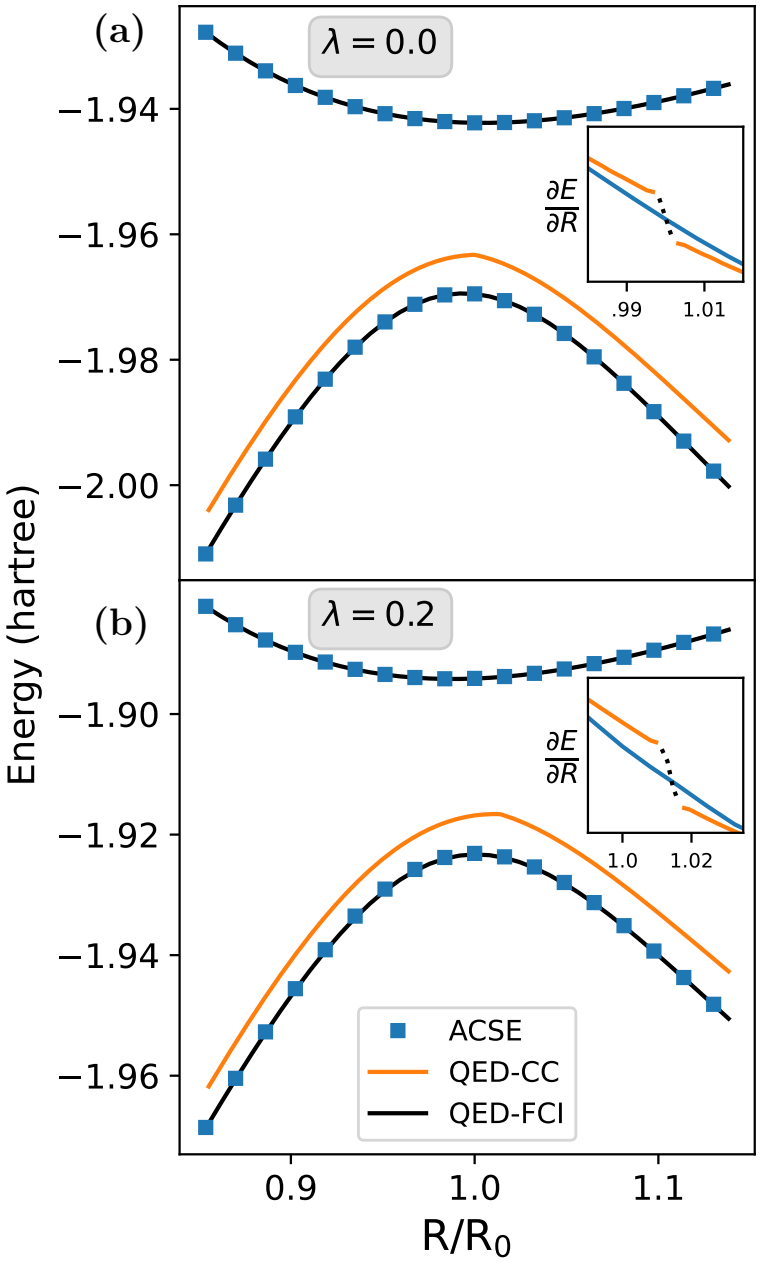

Figure 6.1: Comparison of energies from QED-CC and the ACSE in the deformation of rectangular H_4 coupled to a cavity mode. $R_0 = 1.23$ Å refers to the length of the constant x-axis of H_4, while R is the variable z-axis length. λ refers to the coupling strength in the Pauli-Fierz Hamiltonian oriented along the z-axis. The embedded figures show the gradients of the potential energy surfaces produced by the ACSE and CC near the cusp. The level of theory for each method is ACSE-1, QED-CCSD-1, and QED-FCI-1.

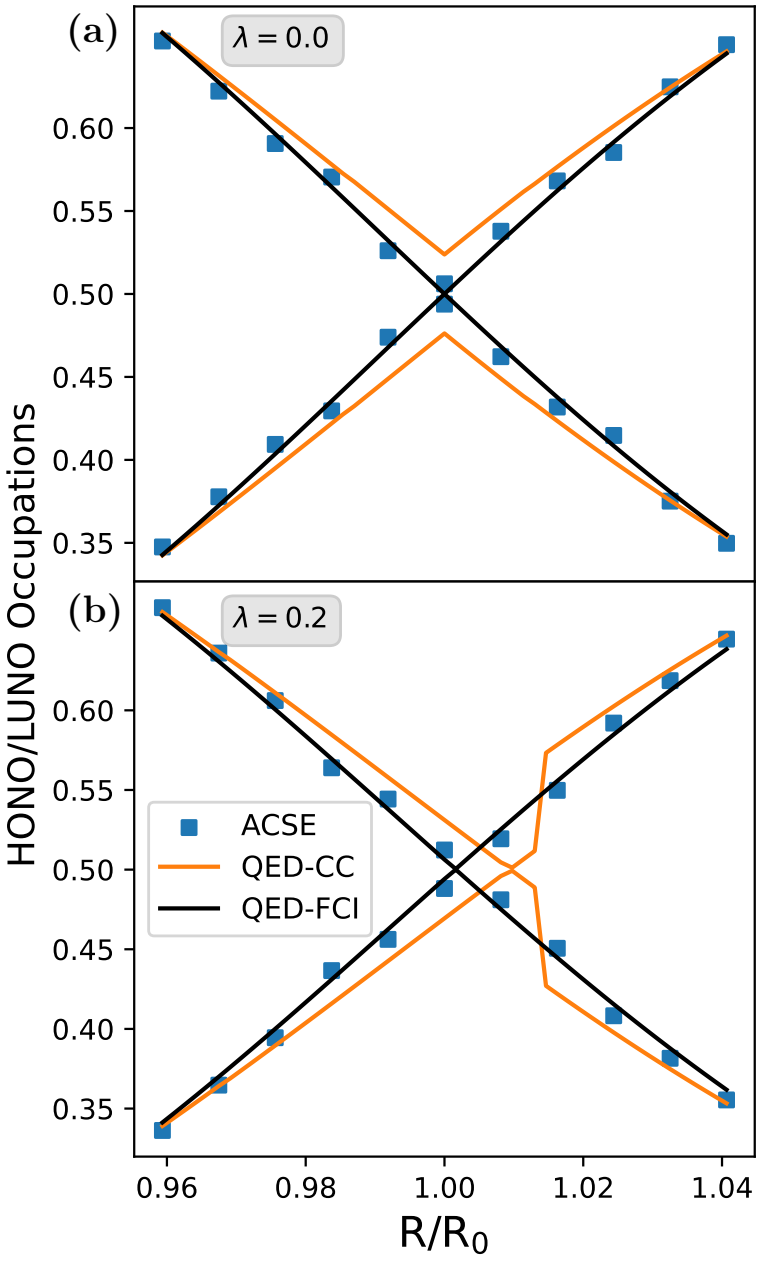

Figure 6.2: HONO and LUNO orbital occupations from QED-CC and the ACSE in the deformation of H_4 coupled to a cavity mode. $R_0 = 1.23$ Å refers to the length of the constant x-axis of H_4, while R is the variable z-axis length. λ refers to the coupling strength in the Pauli-Fierz Hamiltonian oriented along the z-axis. The level of theory for each method is ACSE-1, QED-CCSD-1, and QED-FCI-1.

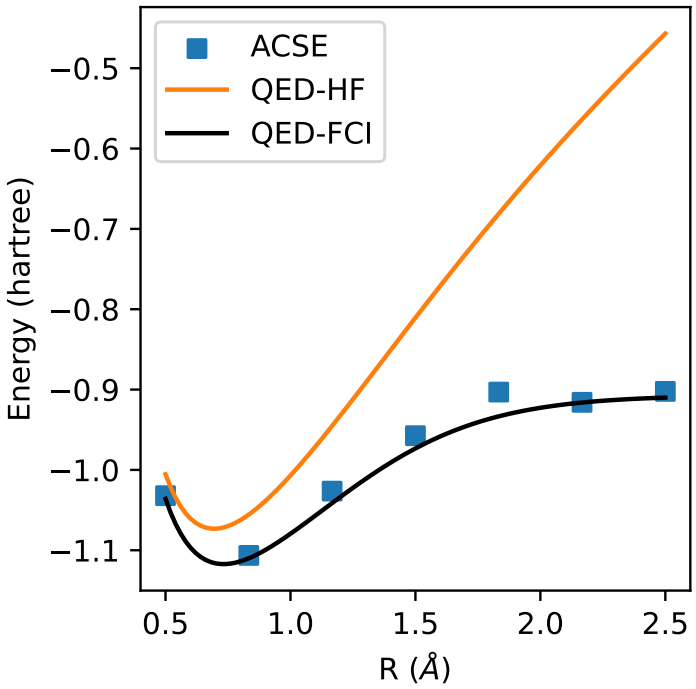

Figure 6.3: Dissociation Curve of H_2 coupled to a bosonic bath on an IBM Quantum Device. The coupling strength was set to $\lambda = .2$. Measurement was preformed on `ibm_cleveland` using 4096 shot per circuit. The level of theory for each method is ACSE-1 and QED-FCI-1.

ACSE-n and QED-FCI-n to refer to ACSE and QED-FCI methods that allow for up to n excitations in the bosonic degrees of freedom. Additionally, the ACSE presented above is meant for quantum devices, we have chosen to use a variational classical-computing version of UCC with single and double excitations (UCCSD), the popular VQE ansatz [295], without truncating the Baker–Campbell–Hausdorff expansion of the exponential. After comparing these methods, we will demonstrate the effectiveness of the ACSE algorithm on an IBM Quantum device for H_2 coupled to a bosonic bath. All results will use the Slater-type orbital (STO-3G) basis set.

Figure 6.1 shows the ground and first excited-state energies for rectangular H_4 as the molecule is distorted into and out of its square conformation (or from the D_{2h} symmetry group into the D_{4h} group) at several different coupling strengths. The CC results in the

Figure 6.1**a** with $\lambda = 0.0$ show a cusp in the energy due to the transition between the restricted Hartree-Fock (RHF) reference A_gB_{3u} and A_gB_{1u} conformations [296, 297, 298, 299], this cusp results in a discontinuity in the derivative of the potential energy surface for CC as seen in the embedded figure. The ACSE, however, starting from the same single-reference Hartree-Fock determinant, is able to resolve the energy to well below chemical accuracy and appropriately mix the different symmetry states. In particular, at the square conformation (the most difficult point to converge) the ACSE reaches chemical accuracy in 20 iterations. Additionally, the ACSE is able to recover the first excited state without any modification to the algorithm when given a singly excited configuration from the RHF reference state as an initial guess. We also found that simultaneously resolving the excited and ground states [276, 238] works well but requires an increased number of iterations to resolve both states to the same level of accuracy as a single-state method.

As the dipole coupling along the z-axis is increased, the energy of the A_gB_{3u} determinant increases faster than the A_gB_{1u} determinant's energy causing QED-HF to incorrectly predict a peak further into the compressed region. This effect arises because, while both determinants see an increase in energy due to a dipole self-energy (DSE) term of Eq. (6.6), only the determinant aligned with the dipole moment (A_gB_{1u}) is able to reap the benefits of the energetically favorable exchange-like integral term that appears in the Hartree-Fock treatment of the DSE [44]. This shift in character makes QED-HF a poor initial guess for CC; therefore, the CC calculations are seeded with several reference states of different symmetries, with the lowest resulting energy kept for the Figure. The CC results are still fairly inaccurate, and now the peak of the CC energy is shifted away from the FCI peak energy. Additionally, the cusp occurs after the peak energy for coupled cluster and is shifted further into the elongated region ($R>R_0$), as can be seen in the embedded figure. The ACSE, on the other hand, captures better-than-chemically-accurate results regardless of the coupling strength for both the ground and excited states, resolving the square conformation to

chemical accuracy in ≈ 80 iterations. This demonstrates the ACSE's ability to treat static correlation and handle strong cavity effects correctly.

Figure 6.2 shows the frontier (highest and lowest) natural orbital occupations (HONO and LUNO, respectively) for H_4 as the molecule is deformed. The results in the no-coupling limit demonstrate the single-reference limitations of coupled cluster which is unable to predict the orbital degeneracy. The ACSE, as expected from the highly accurate energy curves, is able to properly mix the two determinants. In the strongly coupled region, we begin to see the cause of the shifted peak in Figure 6.1. In fact, the coupling makes it energetically possible for CC to retain the A_gB_{3u} configuration until after the orbital degeneracy where the energy peaks. This degeneracy is predicted after the actual FCI orbital degeneracy as first reported by Paldus [297]. The CC result then spontaneously jumps to the A_gB_{1u} configuration causing the discontinuity seen in the energy. Thus the coupling is able to separate the orbital degeneracy from the configurational degeneracy that frustrates single-reference CC methods.

Finally, Figure 6.3 shows the dissociation curve of H_2 when it is strongly coupled to a bosonic bath (i.e., $\lambda = .2$). The ACSE results are obtained on the 127-qubit `ibm_cleveland` device which uses the Eagle r3 processor. The system is mapped to three qubits; two of these qubits model the fermionic degrees of freedom in the CI STO-3G basis using the 2^2=4 configurations for a binary mapping, while the final qubit is devoted to modeling a truncated bosonic bath using a binary mapping for the zero and one population states. Utilizing the Qiskit estimator function for obtaining density matrix elements, we are able to take advantage of the built-in zero noise extrapolation, gate/measurement twirling, and clique covering algorithms [300]. The result is a significant increase in accuracy from QED-HF, with a mean absolute error of $\approx$11 millihartrees from QED-FCI-1. Additionally, the ACSE is able to obtain these energies in fewer than 5 iterations from the QED-HF reference state, demonstrating that the unitary ACSE ansatz is a practical algorithm for resolving

polaritonic ground states on NISQ hardware.

6.5 Conclusions

In conclusion, we have presented a novel, formally exact, polaritonic contracted quantum eigensolver capable of resolving eigenstates of cavity-modified systems, even in the presence of strong correlations. Our approach employs an iterative unitary ansatz derived from the contracted Schrödinger equation that can be implemented on modern quantum devices. Its high accuracy is demonstrated by its numerical performance when modeling the Pauli-Fierz Hamiltonian on the deformed rectangular H_4 coupled to a cavity mode, and its current feasibility on NISQ hardware is showcased by computing the dissociation curve of H_2 strongly coupled to a bosonic bath. The results of this research reveal the broad applicability of contracted quantum eigensolvers and their striking agnostic statistical nature, which ensures their applicability to arbitrary quantum systems.

These developments suggest many interesting research directions. Leveraging the ACSE's accurate treatment of multi-reference character, more physically realistic multimode Pauli-Fierz Hamiltonians could be investigated as these extra degrees of freedom can drastically change the behavior of the system [301, 286]. Additionally, the ACSE has been shown to resolve conical intersections [302], so it could easily be extended to discover cavity-induced conical intersections, a promising avenue for novel synthetic chemistry [303, 304, 51, 234]. As the ACSE accurately predicts energies in both the weak and strong coupling regimes, it could also be utilized to study the ultra-high coupling regimes found in nanoplasmonic systems like picocavities that are used for manipulating intramolecular bonds [305, 306]. Finally, the ACSE's adept handling of bosonic statistics could be employed on the study of dipolar or mixtures of Bose gases, where fascinating states of matter can emerge, such as supersolidity [307].

BIBLIOGRAPHY

[1] J. C. Slater. "Note on Hartree's Method". In: *Physical Review* 35.2 (Jan. 15, 1930), pp. 210–211. DOI: 10.1103/PhysRev.35.210.2.

[2] A. J. Coleman and I. Absar. "Reduced Hamiltonian Orbitals. III. Unitarily Invariant Decomposition of Hermitian Operators". In: *International Journal of Quantum Chemistry* 18.5 (1980), pp. 1279–1307. ISSN: 1097-461X. DOI: 10.1002/qua.560180513.

[3] David A. Mazziotti. "Contracted Schrodinger equation: Determining quantum energies and two-particle density matrices without wave functions". In: *Physical Review A* 57.6 (June 1998), pp. 4219–4234. DOI: 10.1103/PhysRevA.57.4219.

[4] D. R. Hartree. "The Wave Mechanics of an Atom with a Non-Coulomb Central Field. Part II. Some Results and Discussion". In: *Mathematical Proceedings of the Cambridge Philosophical Society* 24.1 (Jan. 1928), pp. 111–132. ISSN: 1469-8064, 0305-0041. DOI: 10.1017/S0305004100011920.

[5] V. Fock. ""Selfconsistent field" mit Austausch für Natrium". In: *Zeitschrift für Physik* 62.11 (Nov. 1, 1930), pp. 795–805. ISSN: 0044-3328. DOI: 10.1007/BF01330439.

[6] Douglas Rayner Hartree and W. Hartree. "Self-Consistent Field, with Exchange, for Beryllium". In: *Proceedings of the Royal Society of London. Series A - Mathematical and Physical Sciences* 150.869 (Jan. 1997), pp. 9–33. DOI: 10.1098/rspa.1935.0085.

[7] Fukashi Sasaki. "Eigenvalues of Fermion Density Matrices". In: *Physical Review* 138.5B (June 1965), B1338–B1342. DOI: 10.1103/PhysRev.138.B1338.

[8] C. N. Yang. "Concept of Off-Diagonal Long-Range Order and the Quantum Phases of Liquid He and of Superconductors". In: *Reviews of Modern Physics* 34.4 (Oct. 1962), pp. 694–704. DOI: 10.1103/RevModPhys.34.694.

[9] Shiva Safaei and David A. Mazziotti. "Quantum signature of exciton condensation". In: *Physical Review B* 98.4 (July 2018), p. 045122. DOI: 10.1103/PhysRevB.98.045122.

[10] LeeAnn M. Sager, Shiva Safaei, and David A. Mazziotti. "Potential coexistence of exciton and fermion-pair condensations". In: *Physical Review B* 101.8 (Feb. 2020), p. 081107. DOI: 10.1103/PhysRevB.101.081107.

[11] LeeAnn M. Sager and David A. Mazziotti. "Cooper-pair condensates with nonclassical long-range order on quantum devices". en. In: *Physical Review Research* 4.1 (Jan. 2022), p. 013003. ISSN: 2643-1564. DOI: 10.1103/PhysRevResearch.4.013003.

[12] LeeAnn M. Sager, Anna O. Schouten, and David A. Mazziotti. "Beginnings of exciton condensation in coronene analog of graphene double layer". In: *The Journal of Chemical Physics* 156.15 (Apr. 2022). Publisher: American Institute of Physics, p. 154702. ISSN: 0021-9606. DOI: 10.1063/5.0084564.

[13] Anna O. Schouten. "Exciton-Condensate-Like Amplification of Energy Transport in Light Harvesting". In: *PRX Energy* 2.2 (2023). DOI: 10.1103/PRXEnergy.2.023002.

[14] Anna O. Schouten. "Exciton-Condensate-Like Energy Transport in Light-Harvesting Complex 2". In: *PRX Energy* 4.1 (2025). DOI: 10.1103/PRXEnergy.4.013004.

[15] Marco Rosina. "Reduced Density Matrices with Applications to Physical and Chemical Systems". In: *Queen's Papers on Pure and Applied Mathematics* 11 (1968). Ed. by John Coleman and R.M. Erdahl.

[16] A. J. Coleman. "Structure of Fermion Density Matrices". In: *Reviews of Modern Physics* 35.3 (July 1963), pp. 668–686. DOI: 10.1103/RevModPhys.35.668.

[17] Ernest Davidson. *Reduced Density Matrices in Quantum Chemistry*. Vol. 6. New York, NY, USA: Academic Press, 1976. 126 pp.

[18] A.J. Coleman and V.I. Yukalov. *Reduced Density Matrices: Coulson's Challenge*. New York, NY, USA: Springer-Verlag, 2000.

[19] David A. Mazziotti. "Realization of Quantum Chemistry without Wave Functions through First-Order Semidefinite Programming". In: *Physical Review Letters* 93.21 (Nov. 2004), p. 213001. DOI: 10.1103/PhysRevLett.93.213001.

[20] D. A. Mazziotti. "Anti-Hermitian part of the contracted Schrödinger equation for the direct calculation of two-electron reduced density matrices". In: *Phys. Rev. A* 75.2 (2007), p. 022505. ISSN: 1050-2947. DOI: 10.1103/physreva.75.022505.

[21] D. A. Mazziotti. "Multireference many-electron correlation energies from two-electron reduced density matrices computed by solving the anti-Hermitian contracted Schrödinger equation". In: *Phys. Rev. A* 76.5 (2007), p. 052502. ISSN: 1050-2947. DOI: 10.1103/physreva.76.052502.

[22] P. J. Flory. "Phase Changes in Proteins and Polypeptides". In: *Journal of Polymer Science* 49.151 (1961), pp. 105–128. ISSN: 1542-6238. DOI: 10.1002/pol.1961.1204915106.

[23] Pilong Li et al. "Phase Transitions in the Assembly of Multivalent Signalling Proteins". In: *Nature* 483.7389 (Mar. 2012), pp. 336–340. ISSN: 1476-4687. DOI: 10.1038/nature10879.

[24] Thomas C. T. Michaels et al. "Amyloid Formation as a Protein Phase Transition". In: *Nature Reviews Physics* 5.7 (July 2023), pp. 379–397. ISSN: 2522-5820. DOI: 10.1038/s42254-023-00598-9.

[25] Masatoshi Imada, Atsushi Fujimori, and Yoshinori Tokura. "Metal-Insulator Transitions". In: *Reviews of Modern Physics* 70.4 (Oct. 1, 1998), pp. 1039–1263. DOI: 10.1103/RevModPhys.70.1039.

[26] Nikhil Shukla et al. "A Steep-Slope Transistor Based on Abrupt Electronic Phase Transition". In: *Nature Communications* 6.1 (Aug. 7, 2015), p. 7812. ISSN: 2041-1723. DOI: 10.1038/ncomms8812.

[27] Dmitriy Tsarev et al. "Phase Transitions, Collective Emotions and Decision-Making Problem in Heterogeneous Social Systems". In: *Scientific Reports* 9.1 (Dec. 2, 2019), p. 18039. ISSN: 2045-2322. DOI: 10.1038/s41598-019-54296-7.

[28] Josiah Gibbs. "Graphical Methods in the Thermodyanamics of Fluids". In: *Transactions of the Connecticut Academy* II (May 1873), pp. 309–342.

[29] Subir Sachdev. *Quantum Phase Transitions*. 2nd. Cambridge, UK: Cambridge University Press, 2011. ISBN: 978-0-521-51468-2.

[30] David Mazziotti. "Complete reconstruction of reduced density matrices". In: *Chemical Physical Letters* 326.3-4 (2000), pp. 212–218.

[31] Alexandra Raeber and David A. Mazziotti. "Large eigenvalue of the cumulant part of the two-electron reduced density matrix as a measure of off-diagonal long-range order". In: *Physical Review A* 92.5 (Nov. 2015), p. 052502. DOI: 10.1103/PhysRevA.92.052502.

[32] Massimo Olivucci and Adalgisa Sinicropi. "I - Computational Photochemistry". In: *Theoretical and Computational Chemistry*. Ed. by M. Olivucci. Vol. 16. Computational Photochemistry. Elsevier, Jan. 1, 2005, pp. 1–33. DOI: 10.1016/S1380-7323(05)80018-4.

[33] Sebastian Mai and Leticia González. "Molecular Photochemistry: Recent Developments in Theory". In: *Angewandte Chemie International Edition* 59.39 (2020), pp. 16832–16846. ISSN: 1521-3773. DOI: 10.1002/anie.201916381.

[34] James K. McCusker. "Electronic Structure in the Transition Metal Block and Its Implications for Light Harvesting". In: *Science* 363.6426 (Feb. 2019), pp. 484–488. DOI: 10.1126/science.aav9104.

[35] Yoshikazu Yamaguchi et al. "Electronic Structure, Spectroscopy, and Photochemistry of Group 8 Metallocenes". In: *Coordination Chemistry Reviews*. A Special Issue Highlighting the Many Aspects of the Electronic Spectrosocpy of Inorganic Compounds 251.3 (Feb. 1, 2007), pp. 515–524. ISSN: 0010-8545. DOI: 10.1016/j.ccr.2006.02.028.

[36] J. J. Hopfield. "Theory of the Contribution of Excitons to the Complex Dielectric Constant of Crystals". In: *Physical Review* 112.5 (Dec. 1, 1958), pp. 1555–1567. DOI: 10.1103/PhysRev.112.1555.

[37] Markus Kowalewski, Kochise Bennett, and Shaul Mukamel. "Non-Adiabatic Dynamics of Molecules in Optical Cavities". In: *The Journal of Chemical Physics* 144.5 (Feb. 5, 2016), p. 054309. ISSN: 0021-9606. DOI: 10.1063/1.4941053.

[38] Javier Galego, Francisco J. Garcia-Vidal, and Johannes Feist. "Suppressing Photochemical Reactions with Quantized Light Fields". In: *Nature Communications* 7.1 (Dec. 12, 2016), p. 13841. ISSN: 2041-1723. DOI: 10.1038/ncomms13841.

[39] E.T. Jaynes and F.W. Cummings. "Comparison of Quantum and Semiclassical Radiation Theories with Application to the Beam Maser". In: *Proceedings of the IEEE* 51.1 (Jan. 1963), pp. 89–109. ISSN: 1558-2256. DOI: 10.1109/PROC.1963.1664.

[40] M. Tavis and F. Cummings. "Approximate Solutions for an N-Molecule-Radiation-Field Hamiltonian". In: *Phys. Rev.* 188.2 (Dec. 1969), p. 692. DOI: 10.1103/PhysRev.188.692.

[41] M. Tavis and F. Cummings. "Exact Solution for an N-Molecule—Radiation-Field Hamiltonian". In: *Phys. Rev.* 170.2 (June 1968), p. 379. DOI: 10.1103/PhysRev.170.379.

[42] M. Babiker, Rodney Loudon, and George William Series. "Derivation of the Power-Zienau-Woolley Hamiltonian in Quantum Electrodynamics by Gauge Transformation". In: *Proc. R. Soc. Lond. A* 385.1789 (Jan. 1983), p. 439. DOI: 10.1098/rspa.1983.0022.

[43] I. V. Tokatly. "Time-Dependent Density Functional Theory for Many-Electron Systems Interacting with Cavity Photons". In: *Phys. Rev. Lett.* 110.23 (June 2013), p. 233001. DOI: 10.1103/PhysRevLett.110.233001.

[44] J. Foley IV, J. McTague, and A. DePrince III. "Ab Initio Methods for Polariton Chemistry". In: *Chem. Phys. Rev.* 4.4 (Oct. 2023), p. 041301. ISSN: 2688-4070. DOI: 10.1063/5.0167243.

[45] A. Mandal et al. "Theoretical Advances in Polariton Chemistry and Molecular Cavity Quantum Electrodynamics". In: *Chem. Rev.* 123.16 (2023), p. 9786. DOI: 10.1021/acs.chemrev.2c00855.

[46] M. Ruggenthaler, F. Mackenroth, and D. Bauer. "Time-Dependent Kohn-Sham Approach to Quantum Electrodynamics". In: *Phys. Rev. A* 84.4 (Oct. 2011), p. 042107. DOI: 10.1103/PhysRevA.84.042107.

[47] M. Ruggenthaler et al. "Quantum-Electrodynamical Density-Functional Theory: Bridging Quantum Optics and Electronic-Structure Theory". In: *Phys. Rev. A* 90.1 (July 2014), p. 012508. DOI: 10.1103/PhysRevA.90.012508.

[48] N. Vu et al. "Enhanced Diastereocontrol via Strong Light–Matter Interactions in an Optical Cavity". In: *J. Phys. Chem. A* 126.49 (Dec. 2022), p. 9303. ISSN: 1089-5639. DOI: 10.1021/acs.jpca.2c07134.

[49] F. Pavošević and A. Rubio. "Wavefunction Embedding for Molecular Polaritons". In: *J. Chem. Phys.* 157.9 (Sept. 2022), p. 094101. ISSN: 0021-9606. DOI: 10.1063/5.0095552.

[50] M. Liebenthal, N. Vu, and A. DePrince III. "Assessing the Effects of Orbital Relaxation and the Coherent-State Transformation in Quantum Electrodynamics Density Functional and Coupled-Cluster Theories". In: *J. Phys. Chem. A* 127.24 (June 2023), p. 5264. ISSN: 1089-5639. DOI: 10.1021/acs.jpca.3c01842.

[51] T. S. Haugland et al. "Coupled Cluster Theory for Molecular Polaritons: Changing Ground and Excited States". In: *Phys. Rev. X* 10 (4 Dec. 2020), p. 041043. DOI: 10.1103/PhysRevX.10.041043.

[52] F. Pavošević and J. Flick. "Polaritonic Unitary Coupled Cluster for Quantum Computations". In: *J. Phys. Chem. Lett.* 12.37 (2021), p. 9100. DOI: 10.1021/acs.jpclett.1c02659.

[53] Joel D. Mallory and A. Eugene DePrince. "Reduced-Density-Matrix-Based Ab Initio Cavity Quantum Electrodynamics". In: *Physical Review A* 106.5 (Nov. 2022), p. 053710. DOI: 10.1103/PhysRevA.106.053710.

[54] Lov K. Grover. "A Fast Quantum Mechanical Algorithm for Database Search". In: *Proceedings of the Twenty-Eighth Annual ACM Symposium on Theory of Computing*. STOC '96. New York, NY, USA: Association for Computing Machinery, July 1, 1996, pp. 212–219. ISBN: 978-0-89791-785-8. DOI: 10.1145/237814.237866.

[55] Peter W. Shor. "Polynomial-Time Algorithms for Prime Factorization and Discrete Logarithms on a Quantum Computer". In: *SIAM Review* 41.2 (Jan. 1999), pp. 303–332. ISSN: 0036-1445. DOI: 10.1137/S0036144598347011.

[56] B. Lanyon et al. "Towards quantum chemistry on a quantum computer". In: *Nature Chem.* 2.2 (Feb. 2010), p. 106. ISSN: 1755-4349. DOI: 10.1038/nchem.483.

[57] P. Barkoutsos et al. “Quantum algorithms for electronic structure calculations: Particle-hole Hamiltonian and optimized wave-function expansions”. In: *Phys. Rev. A* 98 (2 Aug. 2018), p. 022322. DOI: 10.1103/PhysRevA.98.022322.

[58] A. Callison and N. Chancellor. “Hybrid quantum-classical algorithms in the noisy intermediate-scale quantum era and beyond”. In: *Phys. Rev. A* 106 (1 July 2022), p. 010101. DOI: 10.1103/PhysRevA.106.010101.

[59] Jared D. Weidman et al. “Quantum Computing and Chemistry”. In: *Cell Reports Physical Science* 5.9 (Sept. 18, 2024). ISSN: 2666-3864. DOI: 10.1016/j.xcrp.2024.102105.

[60] Alberto Peruzzo et al. “A variational eigenvalue solver on a photonic quantum processor”. en. In: *Nature Communications* 5.1 (July 2014), p. 4213. ISSN: 2041-1723. DOI: 10.1038/ncomms5213.

[61] A. Anand et al. “A quantum computing view on unitary coupled cluster theory”. In: *Chem. Soc. Rev.* 51 (5 2022), p. 1659. DOI: 10.1039/D1CS00932J.

[62] G. Chan, M. Kállay, and J. Gauss. “State-of-the-Art Density Matrix Renormalization Group and Coupled Cluster Theory Studies of the Nitrogen Binding Curve”. In: *J. Chem. Phys.* 121.13 (Oct. 2004), p. 6110. ISSN: 0021-9606. DOI: 10.1063/1.1783212.

[63] T. Van Voorhis and M. Head-Gordon. “Benchmark Variational Coupled Cluster Doubles Results”. In: *J. Chem. Phys.* 113.20 (Nov. 2000), p. 8873. ISSN: 0021-9606. DOI: 10.1063/1.1319643.

[64] C. L. Benavides-Riveros, N. N. Lathiotakis, and M. A. L. Marques. “Towards a formal definition of static and dynamic electronic correlations”. In: *Phys. Chem. Chem. Phys.* 19 (20 2017), p. 12655. DOI: 10.1039/C7CP01137G.

[65] Scott E. Smart and D. A. Mazziotti. "Quantum Solver of Contracted Eigenvalue Equations for Scalable Molecular Simulations on Quantum Computing Devices". In: *Phys. Rev. Lett.* 126 (7 Feb. 2021), p. 070504. DOI: 10.1103/PhysRevLett.126.070504.

[66] Scott Smart, J. Boyn, and D. Mazziotti. "Resolving correlated states of benzyne with an error-mitigated contracted quantum eigensolver". In: *Phys. Rev. A* 105 (2 Feb. 2022), p. 022405. DOI: 10.1103/PhysRevA.105.022405.

[67] Scott Smart and D. A. Mazziotti. *Verifiably Exact Solution of the Electronic Schrödinger Equation on Quantum Devices*. 2023. arXiv: 2303.00758 [quant-ph].

[68] Scott E. Smart and David A. Mazziotti. "Accelerated Convergence of Contracted Quantum Eigensolvers through a Quasi-Second-Order, Locally Parameterized Optimization". In: *Journal of Chemical Theory and Computation* 18.9 (2022), pp. 5286–5296. ISSN: 1549-9618. DOI: 10.1021/acs.jctc.2c00446.

[69] L.D. Landau and E.M. Lifshitz. "The intersection of electron terms". In: *Quantum Mechanics: Non-relativistic Theory*. 2nd. Vol. 3. Institute of Physical Problems USSR: Pergamon, 1965, Pg 297.

[70] Dmitrii L. Maslov and Andrey V. Chubukov. "Nonanalytic paramagnetic response of itinerant fermions away and near a ferromagnetic quantum phase transition". In: *Physical Review B* 79.7 (Feb. 2009), p. 075112. DOI: 10.1103/PhysRevB.79.075112.

[71] D. Bitko, T. F. Rosenbaum, and G. Aeppli. "Quantum Critical Behavior for a Model Magnet". In: *Physical Review Letters* 77.5 (July 1996), pp. 940–943. DOI: 10.1103/PhysRevLett.77.940.

[72] Jinsong Zhang et al. "Topology-Driven Magnetic Quantum Phase Transition in Topological Insulators". In: *Science* 339.6127 (Mar. 2013), pp. 1582–1586. DOI: 10.1126/science.1230905.

[73] A. Maiani et al. "Topological superconductivity in semiconductor–superconductor–magnetic-insulator heterostructures". In: *Physical Review B* 103.10 (Mar. 2021), p. 104508. DOI: 10.1103/PhysRevB.103.104508.

[74] John P. Perdew, Kieron Burke, and Matthias Ernzerhof. "Generalized Gradient Approximation Made Simple". In: *Physical Review Letters* 77.18 (Oct. 1996), pp. 3865–3868. DOI: 10.1103/PhysRevLett.77.3865.

[75] S. L. Sondhi et al. "Continuous quantum phase transitions". In: *Reviews of Modern Physics* 69.1 (Jan. 1997), pp. 315–333. DOI: 10.1103/RevModPhys.69.315.

[76] K. A. Schreiber et al. "Electron–electron interactions and the paired-to-nematic quantum phase transition in the second Landau level". en. In: *Nature Communications* 9.1 (June 2018), p. 2400. ISSN: 2041-1723. DOI: 10.1038/s41467-018-04879-1.

[77] Pierre Nataf et al. "Rashba Cavity QED: A Route Towards the Superradiant Quantum Phase Transition". In: *Physical Review Letters* 123.20 (Nov. 2019), p. 207402. DOI: 10.1103/PhysRevLett.123.207402.

[78] Hilbert von Lohneysen. "Non-Fermi-liquid behavior in the heavy-fermion system $CeCu_{6-x}Au_x$". In: *J. Phys. Condens. Matter* 8 (1998), pp. 9689–9706.

[79] W. Knafo et al. "Antiferromagnetic criticality at a heavy-fermion quantum phase transition". en. In: *Nature Physics* 5.10 (Oct. 2009), pp. 753–757. ISSN: 1745-2481. DOI: 10.1038/nphys1374.

[80] F. Ronning et al. "Electronic in-plane symmetry breaking at field-tuned quantum criticality in $CeRhIn_5$". en. In: *Nature* 548.7667 (Aug. 2017), pp. 313–317. ISSN: 1476-4687. DOI: 10.1038/nature23315.

[81] Matthew P. A. Fisher. "Quantum phase transitions in disordered two-dimensional superconductors". In: *Physical Review Letters* 65.7 (Aug. 1990), pp. 923–926. DOI: 10.1103/PhysRevLett.65.923.

[82] Elbio Dagotto. "Correlated electrons in high-temperature superconductors". In: *Reviews of Modern Physics* 66.3 (July 1994), pp. 763–840. DOI: 10.1103/RevModPhys.66.763.

[83] M. B. Maple. "High-temperature superconductivity". en. In: *Journal of Magnetism and Magnetic Materials*. International Conference on Magnetism 177-181 (Jan. 1998), pp. 18–30. ISSN: 0304-8853. DOI: 10.1016/S0304-8853(97)00999-2.

[84] J. Orenstein and A. J. Millis. "Advances in the Physics of High-Temperature Superconductivity". In: *Science* 288.5465 (Apr. 2000), pp. 468–474. DOI: 10.1126/science.288.5465.468.

[85] Subir Sachdev. "Quantum Criticality: Competing Ground States in Low Dimensions". In: *Science* 288.5465 (Apr. 2000), pp. 475–480. DOI: 10.1126/science.288.5465.475.

[86] Parvis Soltan-Panahi et al. "Quantum phase transition to unconventional multi-orbital superfluidity in optical lattices". en. In: *Nature Physics* 8.1 (Jan. 2012), pp. 71–75. ISSN: 1745-2481. DOI: 10.1038/nphys2128.

[87] P. Holmvall et al. "Broken translational symmetry at edges of high-temperature superconductors". en. In: *Nature Communications* 9.1 (June 2018), p. 2190. ISSN: 2041-1723. DOI: 10.1038/s41467-018-04531-y.

[88] Matthew P. A. Fisher et al. "Boson localization and the superfluid-insulator transition". In: *Physical Review B* 40.1 (July 1989), pp. 546–570. DOI: 10.1103/PhysRevB.40.546.

[89] Markus Greiner et al. "Quantum phase transition from a superfluid to a Mott insulator in a gas of ultracold atoms". en. In: *Nature* 415.6867 (Jan. 2002), pp. 39–44. ISSN: 1476-4687. DOI: 10.1038/415039a.

[90] R. Islam et al. "Onset of a quantum phase transition with a trapped ion quantum simulator". en. In: *Nature Communications* 2.1 (July 2011), p. 377. ISSN: 2041-1723. DOI: 10.1038/ncomms1374.

[91] J. Zhang et al. "Observation of a many-body dynamical phase transition with a 53-qubit quantum simulator". en. In: *Nature* 551.7682 (Nov. 2017), pp. 601–604. ISSN: 1476-4687. DOI: 10.1038/nature24654.

[92] M.-L. Cai et al. "Observation of a quantum phase transition in the quantum Rabi model with a single trapped ion". en. In: *Nature Communications* 12.1 (Feb. 2021), p. 1126. ISSN: 2041-1723. DOI: 10.1038/s41467-021-21425-8.

[93] Sepehr Ebadi et al. "Quantum phases of matter on a 256-atom programmable quantum simulator". en. In: *Nature* 595.7866 (July 2021), pp. 227–232. ISSN: 1476-4687. DOI: 10.1038/s41586-021-03582-4.

[94] L. Demkó et al. "Disorder Promotes Ferromagnetism: Rounding of the Quantum Phase Transition in $Sr_{1x}Ca_xRuO_3$". In: *Physical Review Letters* 108.18 (May 2012), p. 185701. DOI: 10.1103/PhysRevLett.108.185701.

[95] Ying Xing et al. "Ising Superconductivity and Quantum Phase Transition in Macro-Size Monolayer $NbSe_2$". In: *Nano Letters* 17.11 (Nov. 2017), pp. 6802–6807. ISSN: 1530-6984. DOI: 10.1021/acs.nanolett.7b03026.

[96] Yu Saito, Tsutomu Nojima, and Yoshihiro Iwasa. "Quantum phase transitions in highly crystalline two-dimensional superconductors". en. In: *Nature Communications* 9.1 (Feb. 2018), p. 778. ISSN: 2041-1723. DOI: 10.1038/s41467-018-03275-z.

[97] *IBM Quantum*. 2021.

[98] Richard P. Feynman. "Simulating physics with computers". en. In: *International Journal of Theoretical Physics* 21.6 (June 1982), pp. 467–488. ISSN: 1572-9575. DOI: 10.1007/BF02650179.

[99] Ruichao Ma et al. “A dissipatively stabilized Mott insulator of photons”. en. In: *Nature* 566.7742 (Feb. 2019), pp. 51–57. ISSN: 1476-4687. DOI: 10.1038/s41586-019-0897-9.

[100] LeeAnn. M. Sager, Scott. E. Smart, and D. A. Mazziotti. “Preparation of an Exciton Condensate of Photons on a 53-Qubit Quantum Computer”. In: *Physical Review Research* 2.4 (Nov. 2020), p. 043205. ISSN: 2643-1564. DOI: 10.1103/PhysRevResearch.2.043205.

[101] LeeAnn M. Sager and David A. Mazziotti. “Superconductivity and Non-Classical Long-Range Order on a Quantum Computer”. In: *arXiv:2102.08960 [physics, physics:quant-ph]* (June 2021).

[102] Adam Smith et al. “Crossing a topological phase transition with a quantum computer”. In: *arXiv:1910.05351 [cond-mat, physics:quant-ph]* (Sept. 2020).

[103] Scott E. Smart and David A. Mazziotti. “Efficient two-electron ansatz for benchmarking quantum chemistry on a quantum computer”. In: *Physical Review Research* 2.2 (Apr. 2020), p. 023048. DOI: 10.1103/PhysRevResearch.2.023048.

[104] S. E. Smart, D. I. Schuster, and D. A. Mazziotti. “Experimental data from a quantum computer verifies the generalized Pauli exclusion principle”. en. In: *Communications Physics* 2.1 (Jan. 2019), pp. 1–6. ISSN: 2399-3650. DOI: 10.1038/s42005-019-0110-3.

[105] R. M. Erdahl and B. Jin. “The lower bound method for reduced density matrices”. en. In: *Journal of Molecular Structure: THEOCHEM* 527.1 (Aug. 2000), pp. 207–220. ISSN: 0166-1280. DOI: 10.1016/S0166-1280(00)00494-2.

[106] Gergely Gidofalvi and D. A. Mazziotti. “Computation of quantum phase transitions by reduced-density-matrix mechanics”. In: *Physical Review A* 74.1 (July 2006), p. 012501. DOI: 10.1103/PhysRevA.74.012501.

[107] Christine A. Schwerdtfeger and David A. Mazziotti. "Convex-set description of quantum phase transitions in the transverse Ising model using reduced-density-matrix theory". In: *The Journal of Chemical Physics* 130.22 (June 2009), p. 224102. ISSN: 0021-9606. DOI: 10.1063/1.3143403.

[108] V. Zauner et al. "Symmetry Breaking and the Geometry of Reduced Density Matrices". In: *New Journal of Physics* 18.11 (Nov. 2016), p. 113033. ISSN: 1367-2630. DOI: 10.1088/1367-2630/18/11/113033.

[109] L.-A. Wu, M. S. Sarandy, and D. A. Lidar. "Quantum Phase Transitions and Bipartite Entanglement". In: *Physical Review Letters* 93.25 (Dec. 2004). Publisher: American Physical Society, p. 250404. DOI: 10.1103/PhysRevLett.93.250404.

[110] H. J. Lipkin, N. Meshkov, and A. J. Glick. "Validity of many-body approximation methods for a solvable model: (I). Exact solutions and perturbation theory". en. In: *Nuclear Physics* 62.2 (Feb. 1965), pp. 188–198. ISSN: 0029-5582. DOI: 10.1016/0029-5582(65)90862-X.

[111] C. D. Wilen et al. "Correlated charge noise and relaxation errors in superconducting qubits". en. In: *Nature* 594.7863 (June 2021), pp. 369–373. ISSN: 1476-4687. DOI: 10.1038/s41586-021-03557-5.

[112] Jeff R. Hammond and David A. Mazziotti. "Variational two-electron reduced-density-matrix theory: Partial 3-positivity conditions for N-representability". In: *Physical Review A* 71.6 (June 2005), p. 062503. DOI: 10.1103/PhysRevA.71.062503.

[113] Jacob M. Wahlen-Strothman et al. "Merging symmetry projection methods with coupled cluster theory: Lessons from the Lipkin model Hamiltonian". In: *The Journal of Chemical Physics* 146.5 (Feb. 2017), p. 054110. ISSN: 0021-9606. DOI: 10.1063/1.4974989.

[114] Kenneth Robbins and Peter J. Love. "Benchmarking near-term quantum devices with the variational quantum eigensolver and the Lipkin-Meshkov-Glick model". In: *Physical Review A* 104.2 (Aug. 2021), p. 022412. DOI: 10.1103/PhysRevA.104.022412.

[115] Julien Vidal, Guillaume Palacios, and Rémy Mosseri. "Entanglement in a second-order quantum phase transition". In: *Physical Review A* 69.2 (Feb. 2004), p. 022107. DOI: 10.1103/PhysRevA.69.022107.

[116] Román Orús, Sébastien Dusuel, and Julien Vidal. "Equivalence of Critical Scaling Laws for Many-Body Entanglement in the Lipkin-Meshkov-Glick Model". In: *Physical Review Letters* 101.2 (July 2008), p. 025701. DOI: 10.1103/PhysRevLett.101.025701.

[117] Octavio Castaños et al. "Classical and quantum phase transitions in the Lipkin-Meshkov-Glick model". In: *Physical Review B* 74.10 (Sept. 2006), p. 104118. DOI: 10.1103/PhysRevB.74.104118.

[118] Pedro Ribeiro, Julien Vidal, and Rémy Mosseri. "Thermodynamical Limit of the Lipkin-Meshkov-Glick Model". In: *Physical Review Letters* 99.5 (Aug. 2007), p. 050402. DOI: 10.1103/PhysRevLett.99.050402.

[119] W. D. Heiss, F. G. Scholtz, and H. B. Geyer. "The large N behaviour of the Lipkin model and exceptional points". en. In: *Journal of Physics A: Mathematical and General* 38.9 (Feb. 2005), pp. 1843–1851. ISSN: 0305-4470. DOI: 10.1088/0305-4470/38/9/002.

[120] Scott E. Smart and David A. Mazziotti. "Quantum-classical hybrid algorithm using an error-mitigating N-representability condition to compute the Mott metal-insulator transition". In: *Physical Review A* 100.2 (Aug. 2019), p. 022517. DOI: 10.1103/PhysRevA.100.022517.

[121] A. John Coleman. "Kummer variety, geometry of N-representability, and phase transitions". In: *Physical Review A* 66.2 (Aug. 2002), p. 022503. DOI: 10.1103/PhysRevA.66.022503.

[122] D. A. Mazziotti. "Quantum Chemistry without Wave Functions: Two-Electron Reduced Density Matrices". In: *Acc. Chem. Res.* 39.3 (Mar. 2006), p. 207. ISSN: 0001-4842. DOI: 10.1021/ar050029d.

[123] M. Rosina. In: *Reduced Density Matrices with Applications to Physical and Chemical Systems*. Ed. by A. Coleman and R. Erdahl. Queen's papers in pure and applied mathematics, 1968.

[124] D. A. Mazziotti. "Contracted Schrödinger Equation: Determining quantum energies and two-particle density matrices without wave functions". In: *Phys. Rev. A* 57 (6 June 1998), p. 4219. DOI: 10.1103/PhysRevA.57.4219.

[125] David G. Tempel and Alán Aspuru-Guzik. "Quantum Computing Without Wavefunctions: Time-Dependent Density Functional Theory for Universal Quantum Computation". en. In: *Scientific Reports* 2.1 (May 2012), p. 391. ISSN: 2045-2322. DOI: 10.1038/srep00391.

[126] K. Yasuda. "Uniqueness of the solution of the contracted Schrödinger equation". In: *Phys. Rev. A* 65.5 (2002), p. 052121. ISSN: 1050. DOI: 10.1103/physreva.65.052121.

[127] D. B. Stout. "Spontaneous symmetry breaking in a solvable nuclear model". en. In: *Nuclear Physics A* 567.3 (Jan. 1994), pp. 553–575. ISSN: 0375-9474. DOI: 10.1016/0375-9474(94)90024-8.

[128] Sébastien Dusuel and Julien Vidal. "Finite-Size Scaling Exponents of the Lipkin-Meshkov-Glick Model". In: *Physical Review Letters* 93.23 (Dec. 2004), p. 237204. DOI: 10.1103/PhysRevLett.93.237204.

[129] Michael A. Nielsen and Isaac L. Chuang. *Quantum Computation and Quantum Information*. 10th. Cambridge University Press, 2010. ISBN: 978-1-107-00217-3.

[130] Heieke Kamerlingh Onnes. "Investigations into the properties of substances at low temperatures, which have led, amongst other things, to the preparation of liquid helium". In: Dec. 1913.

[131] P. Kapitza. "Viscosity of Liquid Helium below the λ-Point". en. In: *Nature* 141.3558 (Jan. 1938), pp. 74–74. ISSN: 1476-4687. DOI: 10.1038/141074a0.

[132] Sean A. Hartnoll, Christopher P. Herzog, and Gary T. Horowitz. "Building a Holographic Superconductor". In: *Physical Review Letters* 101.3 (July 2008), p. 031601. DOI: 10.1103/PhysRevLett.101.031601.

[133] Philip W. Anderson. "Twenty-five Years of High-Temperature Superconductivity – A Personal Review". en. In: *Journal of Physics: Conference Series* 449 (July 2013), p. 012001. ISSN: 1742-6596. DOI: 10.1088/1742-6596/449/1/012001.

[134] Cheng Chen et al. "Atomic line defects and zero-energy end states in monolayer Fe(Te,Se) high-temperature superconductors". en. In: *Nature Physics* 16.5 (May 2020), pp. 536–540. ISSN: 1745-2481. DOI: 10.1038/s41567-020-0813-0.

[135] Zihan Zhang et al. "Design Principles for High-Temperature Superconductors with a Hydrogen-Based Alloy Backbone at Moderate Pressure". In: *Physical Review Letters* 128.4 (Jan. 2022), p. 047001. DOI: 10.1103/PhysRevLett.128.047001.

[136] V. Bouchiat et al. "Quantum coherence with a single Cooper pair". en. In: *Physica Scripta* 1998.T76 (Jan. 1998), p. 165. ISSN: 1402-4896. DOI: 10.1238/Physica.Topical.076a00165.

[137] Y. Nakamura, Yu A. Pashkin, and J. S. Tsai. "Coherent control of macroscopic quantum states in a single-Cooper-pair box". en. In: *Nature* 398.6730 (Apr. 1999), pp. 786–788. ISSN: 1476-4687. DOI: 10.1038/19718.

[138] A. Yu Kitaev. "Fault-tolerant quantum computation by anyons". In: *Annals of Physics* 303.1 (Jan. 2003), pp. 2–30. ISSN: 00034916. DOI: 10.1016/S0003-4916(02)00018-0.

[139] Jay D. Sau et al. "Generic New Platform for Topological Quantum Computation Using Semiconductor Heterostructures". In: *Physical Review Letters* 104.4 (Jan. 2010), p. 040502. DOI: 10.1103/PhysRevLett.104.040502.

[140] Sébastien Dusuel et al. "Robustness of a Perturbed Topological Phase". In: *Physical Review Letters* 106.10 (Mar. 2011), p. 107203. DOI: 10.1103/PhysRevLett.106.107203.

[141] L. V. Keldysh. "Coherent states of excitons". en. In: *Physics-Uspekhi* 60.11 (Nov. 2017), p. 1180. ISSN: 1063-7869. DOI: 10.3367/UFNe.2017.10.038227.

[142] D. V. Fil and S. I. Shevchenko. "Electron-hole Superconductivity (Review)". In: *Low Temperature Physics* 44.9 (Sept. 2018), pp. 867–909. ISSN: 1063-777X. DOI: 10.1063/1.5052674.

[143] Anna O. Schouten, LeeAnn M. Sager, and David A. Mazziotti. "Exciton Condensation in Molecular-Scale van der Waals Stacks". In: *The Journal of Physical Chemistry Letters* 12.40 (Oct. 2021), pp. 9906–9911. DOI: 10.1021/acs.jpclett.1c02368.

[144] S. E. Muraviev and O. A. Rumyantsev. "Exciton and fermion-pair condensation at non-zero temperature". en. In: *Journal of Physics: Condensed Matter* 34.14 (Feb. 2022), p. 145402. ISSN: 0953-8984. DOI: 10.1088/1361-648X/ac4c63.

[145] LeeAnn M. Sager and David A. Mazziotti. "Simultaneous fermion and exciton condensations from a model Hamiltonian". In: *Physical Review B* 105.3 (Jan. 2022), p. 035143. DOI: 10.1103/PhysRevB.105.035143.

[146] J. Bardeen, L. N. Cooper, and J. R. Schrieffer. "Theory of Superconductivity". In: *Physical Review* 108.5 (Dec. 1957), pp. 1175–1204. DOI: 10.1103/PhysRev.108.1175.

[147] N. Meshkov, A. J. Glick, and H. J. Lipkin. "Validity of many-body approximation methods for a solvable model: (II). Linearization procedures". en. In: *Nuclear Physics* 62.2 (Feb. 1965), pp. 199–210. ISSN: 0029-5582. DOI: 10.1016/0029-5582(65)90863-1.

[148] D. A. Mazziotti. "Exactness of wave functions from two-body exponential transformations in many-body quantum theory". In: *Phys. Rev. A* 69 (1 Jan. 2004), p. 012507. DOI: 10.1103/PhysRevA.69.012507.

[149] Gang Chen and J.-Q. Liang. "Unconventional quantum phase transition in the finite-size Lipkin–Meshkov–Glick model". en. In: *New Journal of Physics* 8.12 (Dec. 2006), pp. 297–297. ISSN: 1367-2630. DOI: 10.1088/1367-2630/8/12/297.

[150] Qian Wang and Francisco Pérez-Bernal. "Characterizing the Lipkin-Meshkov-Glick model excited-state quantum phase transition using dynamical and statistical properties of the diagonal entropy". In: *Physical Review E* 103.3 (Mar. 2021), p. 032109. DOI: 10.1103/PhysRevE.103.032109.

[151] A. J. Coleman. "Structure of Fermion Density Matrices. II. Antisymmetrized Geminal Powers". In: *Journal of Mathematical Physics* 6.9 (Sept. 1965), pp. 1425–1431. ISSN: 0022-2488. DOI: 10.1063/1.1704794.

[152] Claude Garrod and Mitja Rosina. "Particle-Hole Matrix: Its Connection with the Symmetries and Collective Features of the Ground State". In: *Journal of Mathematical Physics* 10.10 (Oct. 1969), pp. 1855–1861. ISSN: 0022-2488. DOI: 10.1063/1.1664770.

[153] Bose. "Plancks Gesetz und Lichtquantenhypothese". de. In: *Zeitschrift für Physik* 26.1 (Dec. 1924), pp. 178–181. ISSN: 0044-3328. DOI: 10.1007/BF01327326.

[154] P. R. Surjan. "An Introduction to the Theory of Geminals". In: *Correlation and Localization*. Berlin, Heidelberg: Springer, 1999, pp. 63–88.

[155] F. London. “On the Bose-Einstein Condensation”. In: *Physical Review* 54.11 (Dec. 1938), pp. 947–954. DOI: 10.1103/PhysRev.54.947.

[156] Laszlo Tisza. “The Theory of Liquid Helium”. In: *Physical Review* 72.9 (Nov. 1947), pp. 838–854. DOI: 10.1103/PhysRev.72.838.

[157] David A. Mazziotti. “Large-Scale Semidefinite Programming for Many-Electron Quantum Mechanics”. In: *Physical Review Letters* 106.8 (Feb. 2011), p. 083001. DOI: 10.1103/PhysRevLett.106.083001.

[158] Ji-Yao Chen et al. “Geometry of reduced density matrices for symmetry-protected topological phases”. In: *Physical Review A* 93.1 (Jan. 2016), p. 012309. DOI: 10.1103/PhysRevA.93.012309.

[159] LeeAnn M. Sager and David A. Mazziotti. “Entangled phase of simultaneous fermion and exciton condensations realized”. In: *Physical Review B* 105.12 (Mar. 2022), p. L121105. DOI: 10.1103/PhysRevB.105.L121105.

[160] Shlomi Bouscher et al. “Enhanced Cooper-Pair Injection into a Semiconductor Structure by Resonant Tunneling”. In: *Physical Review Letters* 128.12 (Mar. 2022). Publisher: American Physical Society, p. 127701. DOI: 10.1103/PhysRevLett.128.127701.

[161] D. J. Thouless et al. “Quantized Hall Conductance in a Two-Dimensional Periodic Potential”. In: *Physical Review Letters* 49.6 (Aug. 1982), pp. 405–408. DOI: 10.1103/PhysRevLett.49.405.

[162] F. D. M. Haldane. “Model for a Quantum Hall Effect without Landau Levels: Condensed-Matter Realization of the ”Parity Anomaly””. In: *Physical Review Letters* 61.18 (Oct. 1988), pp. 2015–2018. DOI: 10.1103/PhysRevLett.61.2015.

[163] P. St-Jean et al. “Lasing in topological edge states of a one-dimensional lattice”. In: *Nature Photonics* 11.10 (Oct. 2017), pp. 651–656. ISSN: 1749-4893. DOI: 10.1038/s41566-017-0006-2.

[164] Miguel A. Bandres et al. “Topological insulator laser: Experiments”. In: *Science* 359.6381 (Mar. 2018), eaar4005. DOI: 10.1126/science.aar4005.

[165] Zeng-Kai Shao et al. “A high-performance topological bulk laser based on band-inversion-induced reflection”. In: *Nature Nanotechnology* 15.1 (Jan. 2020), pp. 67–72. ISSN: 1748-3395. DOI: 10.1038/s41565-019-0584-x.

[166] Yongquan Zeng et al. “Electrically pumped topological laser with valley edge modes”. In: *Nature* 578.7794 (Feb. 2020), pp. 246–250. ISSN: 1476-4687. DOI: 10.1038/s41586-020-1981-x.

[167] Tristan H. Harder et al. “Coherent Topological Polariton Laser”. In: *ACS Photonics* 8.5 (May 2021), pp. 1377–1384. DOI: 10.1021/acsphotonics.0c01958.

[168] Jingyi Tian et al. “Perovskite quantum dot one-dimensional topological laser”. In: *Nature Communications* 14.1 (Mar. 2023), p. 1433. ISSN: 2041-1723. DOI: 10.1038/s41467-023-36963-6.

[169] Alexei Kitaev. “Anyons in an exactly solved model and beyond”. In: *Annals of Physics*. January Special Issue 321.1 (Jan. 2006), pp. 2–111. ISSN: 0003-4916. DOI: 10.1016/j.aop.2005.10.005.

[170] Michael Freedman, Chetan Nayak, and Kirill Shtengel. “Extended Hubbard Model with Ring Exchange: A Route to a Non-Abelian Topological Phase”. In: *Physical Review Letters* 94.6 (Feb. 2005), p. 066401. DOI: 10.1103/PhysRevLett.94.066401.

[171] Paul Fendley and Eduardo Fradkin. “Realizing non-Abelian statistics in time-reversal-invariant systems”. In: *Physical Review B* 72.2 (July 2005), p. 024412. DOI: 10.1103/PhysRevB.72.024412.

[172] R. B. Laughlin. "Quantized Hall conductivity in two dimensions". In: *Physical Review B* 23.10 (May 1981), pp. 5632–5633. DOI: 10.1103/PhysRevB.23.5632.

[173] A. H. MacDonald. "Edge states in the fractional-quantum-Hall-effect regime". In: *Physical Review Letters* 64.2 (Jan. 1990), pp. 220–223. DOI: 10.1103/PhysRevLett.64.220.

[174] Sankar Das Sarma, Michael Freedman, and Chetan Nayak. "Topologically Protected Qubits from a Possible Non-Abelian Fractional Quantum Hall State". In: *Physical Review Letters* 94.16 (Apr. 2005), p. 166802. DOI: 10.1103/PhysRevLett.94.166802.

[175] Maissam Barkeshli and Xiao-Gang Wen. "Anyon Condensation and Continuous Topological Phase Transitions in Non-Abelian Fractional Quantum Hall States". In: *Physical Review Letters* 105.21 (Nov. 2010), p. 216804. DOI: 10.1103/PhysRevLett.105.216804.

[176] Eddy Ardonne and Kareljan Schoutens. "New Class of Non-Abelian Spin-Singlet Quantum Hall States". In: *Physical Review Letters* 82.25 (June 1999), pp. 5096–5099. DOI: 10.1103/PhysRevLett.82.5096.

[177] T. Senthil, J. B. Marston, and Matthew P. A. Fisher. "Spin quantum Hall effect in unconventional superconductors". In: *Physical Review B* 60.6 (Aug. 1999), pp. 4245–4254. DOI: 10.1103/PhysRevB.60.4245.

[178] Samuel Warren, LeeAnn M. Sager-Smith, and David A. Mazziotti. "Quantum simulation of quantum phase transitions using the convex geometry of reduced density matrices". In: *Physical Review A* 106.1 (July 2022), p. 012434. DOI: 10.1103/PhysRevA.106.012434.

[179] Valentin Zauner-Stauber and Frank Verstraete. "Symmetry Breaking and Convex Set Phase Diagrams for the q-state Potts Model". In: *New Journal of Physics* 18.11 (Nov. 2016), p. 113033. ISSN: 1367-2630. DOI: 10.1088/1367-2630/18/11/113033.

[180] Per-Olov Löwdin. "Quantum Theory of Many-Particle Systems. I. Physical Interpretations by Means of Density Matrices, Natural Spin-Orbitals, and Convergence Problems in the Method of Configurational Interaction". In: *Physical Review* 97.6 (Mar. 1955), pp. 1474–1489. DOI: 10.1103/PhysRev.97.1474.

[181] Per-Olov Löwdin. "Quantum Theory of Many-Particle Systems. II. Study of the Ordinary Hartree-Fock Approximation". In: *Physical Review* 97.6 (Mar. 1955), pp. 1490–1508. DOI: 10.1103/PhysRev.97.1490.

[182] A. J. Coleman. "The structure of fermion density matrices. III. Long-range order". In: *Journal of Low Temperature Physics* 74.1 (Jan. 1989), pp. 1–17. ISSN: 1573-7357. DOI: 10.1007/BF00681750.

[183] Tamás Juhász and David A. Mazziotti. "The cumulant two-particle reduced density matrix as a measure of electron correlation and entanglement". In: *The Journal of Chemical Physics* 125.17 (Nov. 2006), p. 174105. ISSN: 0021-9606. DOI: 10.1063/1.2378768.

[184] John E. Harriman. "Reduced-density-matrix cumulants and correlation". In: *Physical Review A* 75.3 (Mar. 2007), p. 032513. DOI: 10.1103/PhysRevA.75.032513.

[185] D. R. Alcoba et al. "On the measure of electron correlation and entanglement in quantum chemistry based on the cumulant of the second-order reduced density matrix". In: *The Journal of Chemical Physics* 133.14 (Oct. 2010), p. 144104. ISSN: 0021-9606. DOI: 10.1063/1.3503766.

[186] Eloy Ramos-Cordoba, Pedro Salvador, and Eduard Matito. "Separation of dynamic and nondynamic correlation". In: *Physical Chemistry Chemical Physics* 18.34 (Aug. 2016), pp. 24015–24023. ISSN: 1463-9084. DOI: 10.1039/C6CP03072F.

[187] W. P. Su, J. R. Schrieffer, and A. J. Heeger. "Solitons in Polyacetylene". In: *Physical Review Letters* 42.25 (June 1979), pp. 1698–1701. DOI: 10.1103/PhysRevLett.42.1698.

[188] Alexei Kitaev. "Unpaired Majorana fermions in quantum wires". In: *Physics-Uspekhi* 44.10 (Oct. 2001), pp. 131–136. ISSN: 1468-4780. DOI: 10.1070/1063-7869/44/10S/S29.

[189] Wei Chen et al. "Correlation length, universality classes, and scaling laws associated with topological phase transitions". In: *Physical Review B* 95.7 (Feb. 2017), p. 075116. DOI: 10.1103/PhysRevB.95.075116.

[190] David A Mazziotti. "Approximate solution for electron correlation through the use of Schwinger probes". en. In: *Chemical Physics Letters* 289.5 (June 1998), pp. 419–427. ISSN: 0009-2614. DOI: 10.1016/S0009-2614(98)00470-9.

[191] Marco Bianucci and Mauro Bologna. "About the foundation of the Kubo generalized cumulants theory: a revisited and corrected approach". In: *Journal of Statistical Mechanics: Theory and Experiment* 2020.4 (Apr. 2020), p. 043405. ISSN: 1742-5468. DOI: 10.1088/1742-5468/ab7755.

[192] Julie T. Skolnik and David A. Mazziotti. "Cumulant reduced density matrices as measures of statistical dependence and entanglement between electronic quantum domains with application to photosynthetic light harvesting". In: *Physical Review A* 88.3 (Sept. 2013), p. 032517. DOI: 10.1103/PhysRevA.88.032517.

[193] Olivia Werba et al. "Signature of van der Waals interactions in the cumulant density matrix". In: *Physical Chemistry Chemical Physics* 21.43 (Nov. 2019), pp. 23900–23905. ISSN: 1463-9084. DOI: 10.1039/C9CP03361K.

[194] Anna O. Schouten, LeeAnn M. Sager-Smith, and David A. Mazziotti. "Large cumulant eigenvalue as a signature of exciton condensation". In: *Physical Review B* 105.24 (June 2022), p. 245151. DOI: 10.1103/PhysRevB.105.245151.

[195] Stefan Donsa et al. "Nonequilibrium correlation dynamics in the one-dimensional Fermi-Hubbard model: A testbed for the two-particle reduced density matrix theory". In: *Physical Review Research* 5.3 (July 2023), p. 033022. DOI: 10.1103/PhysRevResearch.5.033022.

[196] Ettore Majorana. "Teoria simmetrica dell'elettrone e del positrone". In: *Il Nuovo Cimento (1924-1942)* 14.4 (Apr. 1937), pp. 171–184. ISSN: 1827-6121. DOI: 10.1007/BF02961314.

[197] J. Ziman. *Electrons and Phonons: The Theory of Transport Phenomena in Solids*. Oxford University Press, Feb. 2001. ISBN: 9780198507796. DOI: 10.1093/acprof:oso/9780198507796.001.0001.

[198] H. Fröhlich. "Electrons in lattice fields". In: *Adv. Phys.* 3.11 (1954), p. 325. DOI: 10.1080/00018735400101213.

[199] F. J. Garcia-Vidal, C. Ciuti, and T. W. Ebbesen. "Manipulating matter by strong coupling to vacuum fields". In: *Science* 373.6551 (2021), eabd0336. DOI: 10.1126/science.abd0336.

[200] T. W. Ebbesen. "Hybrid Light–Matter States in a Molecular and Material Science Perspective". In: *Acc. Chem. Res* 49.11 (2016), p. 2403. DOI: 10.1021/acs.accounts.6b00295.

[201] R. Ribeiro et al. "Polariton Chemistry: Controlling Molecular Dynamics with Optical Cavities". In: *Chem. Sci.* 9.30 (2018), p. 6325. DOI: 10.1039/C8SC01043A.

[202] A. Thomas et al. “Ground-State Chemical Reactivity under Vibrational Coupling to the Vacuum Electromagnetic Field”. In: *Angew. Chem. Int. Ed.* 55.38 (2016), p. 11462. DOI: https://doi.org/10.1002/anie.201605504.

[203] S. Mondal and A. Lunghi. “Spin-phonon decoherence in solid-state paramagnetic defects from first principles”. In: *npj Comput. Mater.* 9.1 (July 2023), p. 120. ISSN: 2057-3960. DOI: 10.1038/s41524-023-01082-9.

[204] K. Jahnke et al. “Electron–phonon processes of the silicon-vacancy centre in diamond”. In: *New J. Phys.* 17.4 (Apr. 2015), p. 043011. DOI: 10.1088/1367-2630/17/4/043011.

[205] T. D. Ladd et al. “Quantum computers”. In: *Nature* 464.7285 (Mar. 2010), p. 45. ISSN: 1476-4687. DOI: 10.1038/nature08812.

[206] J. Bloch et al. “Strongly correlated electron–photon systems”. In: *Nature* 606.7912 (June 2022), p. 41. ISSN: 1476-4687. DOI: 10.1038/s41586-022-04726-w.

[207] J. Campos-Gonzalez-Angulo, R. Ribeiro, and J. Yuen-Zhou. “Resonant Catalysis of Thermally Activated Chemical Reactions with Vibrational Polaritons”. In: *Nat. Commun.* 10.1 (Oct. 2019), p. 4685. ISSN: 2041-1723. DOI: 10.1038/s41467-019-12636-1.

[208] S. Kéna-Cohen and J. Yuen-Zhou. “Polariton Chemistry: Action in the Dark”. In: *ACS Cent. Sci.* 5.3 (Mar. 2019), p. 386. ISSN: 2374-7943. DOI: 10.1021/acscentsci.9b00219.

[209] M. Du and J. Yuen-Zhou. “Catalysis by Dark States in Vibropolaritonic Chemistry”. In: *Phys. Rev. Lett.* 128.9 (Feb. 2022), p. 096001. DOI: 10.1103/PhysRevLett.128.096001.

[210] M. Farhat et al. “Bifacial Schottky-Junction Plasmonic-Based Solar Cell”. In: *Energy Technol.* 8.5 (2020), p. 1901280. ISSN: 2194-4296. DOI: 10.1002/ente.201901280.

[211] A. Imamoglu et al. "Nonequilibrium Condensates and Lasers without Inversion: Exciton-polariton Lasers". In: *Phys. Rev. A* 53.6 (June 1996), p. 4250. DOI: 10.1103/PhysRevA.53.4250.

[212] H. Deng et al. "Polariton Lasing vs. Photon Lasing in a Semiconductor Microcavity". In: *Proc. Natl. Acad. Sci. U.S.A.* 100.26 (Dec. 2003), p. 15318. DOI: 10.1073/pnas.2634328100.

[213] S. Kim et al. "Coherent Polariton Laser". In: *Phys. Rev. X* 6.1 (Mar. 2016), p. 011026. DOI: 10.1103/PhysRevX.6.011026.

[214] M. Leng et al. "Optically Pumped Polaritons in Perovskite Light-Emitting Diodes". In: *ACS Photonics* 10.5 (May 2023), p. 1349. DOI: 10.1021/acsphotonics.2c01999.

[215] F. Giustino. "Electron-phonon interactions from first principles". In: *Rev. Mod. Phys.* 89 (1 Feb. 2017), p. 015003. DOI: 10.1103/RevModPhys.89.015003.

[216] H. Walther et al. "Cavity quantum electrodynamics". In: *Rep. Prog. Phys.* 69.5 (2006), p. 1325. DOI: 10.1088/0034-4885/69/5/R02.

[217] J. Levinsen et al. "Spectroscopic Signatures of Quantum Many-Body Correlations in Polariton Microcavities". In: *Phys. Rev. Lett.* 123 (26 Dec. 2019), p. 266401. DOI: 10.1103/PhysRevLett.123.266401.

[218] L. Tan et al. "Bose Polaron Interactions in a Cavity-Coupled Monolayer Semiconductor". In: *Phys. Rev. X* 13 (3 Sept. 2023), p. 031036. DOI: 10.1103/PhysRevX.13.031036.

[219] H. Spohn. *Dynamics of Charged Particles and their Radiation Field*. Cambridge University Press, 2004. DOI: 10.1017/CBO9780511535178.

[220] M. Schuler et al. "The vacua of dipolar cavity quantum electrodynamics". In: *SciPost Phys.* 9 (2020), p. 066. DOI: 10.21468/SciPostPhys.9.5.066.

[221] M. Hertzog et al. "Strong light–matter interactions: a new direction within chemistry". In: *Chem. Soc. Rev.* 48 (3 2019), p. 937. DOI: 10.1039/C8CS00193F.

[222] M. Ruggenthaler, D. Sidler, and A. Rubio. "Understanding Polaritonic Chemistry from Ab Initio Quantum Electrodynamics". In: *Chem. Rev.* 123.19 (2023), p. 11191. DOI: 10.1021/acs.chemrev.2c00788.

[223] J. Flick et al. "Ab Initio Optimized Effective Potentials for Real Molecules in Optical Cavities: Photon Contributions to the Molecular Ground State". In: *ACS Photonics* 5.3 (Mar. 2018), p. 992. DOI: 10.1021/acsphotonics.7b01279.

[224] X. Gonze, D. C. Allan, and M. P. Teter. "Dielectric tensor, effective charges, and phonons in α-quartz by variational density-functional perturbation theory". In: *Phys. Rev. Lett.* 68 (24 June 1992), p. 3603. DOI: 10.1103/PhysRevLett.68.3603.

[225] T. Sohier, M. Calandra, and F. Mauri. "Two-dimensional Fröhlich interaction in transition-metal dichalcogenide monolayers: Theoretical modeling and first-principles calculations". In: *Phys. Rev. B* 94 (8 Aug. 2016), p. 085415. DOI: 10.1103/PhysRevB.94.085415.

[226] D. Juraschek and P. Narang. "Highly Confined Phonon Polaritons in Monolayers of Perovskite Oxides". In: *Nano Letters* 21.12 (June 2021), p. 5098. ISSN: 1530-6984. DOI: 10.1021/acs.nanolett.1c01002.

[227] M. Ruggenthaler et al. "From a quantum-electrodynamical light–matter description to novel spectroscopies". In: *Nat. Rev. Chem.* 2.3 (Mar. 2018), p. 0118. ISSN: 2397-3358. DOI: 10.1038/s41570-018-0118.

[228] D. Welakuh and P. Narang. "Tunable Nonlinearity and Efficient Harmonic Generation from a Strongly Coupled Light–Matter System". In: *ACS Photonics* 10.2 (Feb. 2023), p. 383. DOI: 10.1021/acsphotonics.2c00966.

[229] A. Marini. "Equilibrium and out-of-equilibrium realistic phonon self-energy free from overscreening". In: *Phys. Rev. B* 107 (2 Jan. 2023), p. 024305. DOI: 10.1103/PhysRevB.107.024305.

[230] G. Stefanucci, R. van Leeuwen, and E. Perfetto. "In and Out-of-Equilibrium Ab Initio Theory of Electrons and Phonons". In: *Phys. Rev. X* 13 (3 Sept. 2023), p. 031026. DOI: 10.1103/PhysRevX.13.031026.

[231] J. Čížek. "On the Correlation Problem in Atomic and Molecular Systems. Calculation of Wavefunction Components in Ursell-Type Expansion Using Quantum-Field Theoretical Methods". In: *J. Chem. Phys.* 45.11 (May 1966), p. 4256. ISSN: 0021-9606. DOI: 10.1063/1.1727484.

[232] H. Kümmel. "Origins of the Coupled Cluster Method". In: *Theoret. Chim. Acta* 80.2 (Mar. 1991), p. 81. ISSN: 1432-2234. DOI: 10.1007/BF01119615.

[233] A. White et al. "A coupled cluster framework for electrons and phonons". In: *J. Chem. Phys.* 153.22 (Dec. 2020), p. 224112. ISSN: 0021-9606. DOI: 10.1063/5.0033132.

[234] U. Mordovina et al. "Polaritonic Coupled-Cluster Theory". In: *Phys. Rev. Res.* 2.2 (June 2020), p. 023262. DOI: 10.1103/PhysRevResearch.2.023262.

[235] M. Liebenthal, N. Vu, and A. DePrince III. "Equation-of-Motion Cavity Quantum Electrodynamics Coupled-Cluster Theory for Electron Attachment". In: *J. Chem. Phys.* 156.5 (Feb. 2022), p. 054105. ISSN: 0021-9606. DOI: 10.1063/5.0078795.

[236] F. Pavošević, I. Tavernelli, and A. Rubio. "Spin-Flip Unitary Coupled Cluster Method: Toward Accurate Description of Strong Electron Correlation on Quantum Computers". In: *J. Phys. Chem. Lett.* 14.35 (2023), p. 7876. DOI: 10.1021/acs.jpclett.3c01935.

[237] M. Denner et al. “A hybrid quantum-classical method for electron-phonon systems”. In: *Commun. Phys.* 6.1 (Aug. 2023), p. 233. ISSN: 2399-3650. DOI: 10.1038/s42005-023-01353-3.

[238] C. L. Benavides-Riveros et al. “Excitations of Quantum Many-Body Systems via Purified Ensembles: A Unitary-Coupled-Cluster-Based Approach”. In: *Phys. Rev. Lett.* 129 (6 Aug. 2022), p. 066401. DOI: 10.1103/PhysRevLett.129.066401.

[239] H. R. Grimsley et al. “Is the Trotterized UCCSD Ansatz Chemically Well-Defined?” In: *J. Chem. Theory Comput.* 16.1 (2020), p. 1. DOI: 10.1021/acs.jctc.9b01083.

[240] D. A. Mazziotti. “Contracted Schrödinger Equation: Determining Quantum Energies and Two-Particle Density Matrices without Wave Functions”. In: *Phys. Rev. A* 57.6 (June 1998), p. 4219. DOI: 10.1103/PhysRevA.57.4219.

[241] F. Colmenero and C. Valdemoro. “Approximating q-order reduced density matrices in terms of the lower-order ones. II. Applications”. In: *Phys. Rev. A* 47.2 (1993), p. 979. ISSN: 1050-2947. DOI: 10.1103/physreva.47.979.

[242] H. Nakatsuji and K. Yasuda. “Direct Determination of the Quantum-Mechanical Density Matrix Using the Density Equation”. In: *Phys. Rev. Lett.* 76.7 (1996), p. 1039. ISSN: 0031-9007. DOI: 10.1103/physrevlett.76.1039.

[243] D. A. Mazziotti. “Comparison of contracted Schrödinger and coupled-cluster theories”. In: *Phys. Rev. A* 60.6 (1999), p. 4396. ISSN: 1050-2947. DOI: 10.1103/physreva.60.4396.

[244] D. Mukherjee and W. Kutzelnigg. “Irreducible Brillouin conditions and contracted Schrödinger equations for n-electron systems. I. The equations satisfied by the density cumulants”. In: *J. Chem. Phys.* 114.5 (2001), p. 2047. ISSN: 0021-9606. DOI: 10.1063/1.1337058.

[245] D. A. Mazziotti. "Variational method for solving the contracted Schrödinger equation through a projection of the N-particle power method onto the two-particle space". In: *J. Chem. Phys.* 116.4 (2002), pp. 1239–1249. ISSN: 0021-9606. DOI: 10.1063/1.1430257.

[246] D. A. Mazziotti. "Exact two-body expansion of the many-particle wave function". In: *Phys. Rev. A* 102.3 (2020), p. 030802. ISSN: 2469-9926. DOI: 10.1103/physreva.102.030802.

[247] Scott E. Smart and D. A. Mazziotti. "Verifiably exact solution of the electronic Schrödinger equation on quantum devices". In: *Phys. Rev. A* 109.2 (2024), p. 022802. ISSN: 2469-9926. DOI: 10.1103/physreva.109.022802.

[248] L. Cohen and C. Frishberg. "Hierarchy Equations for Reduced Density Matrices". In: *Phys. Rev. A* 13.3 (Mar. 1976), p. 927. DOI: 10.1103/PhysRevA.13.927.

[249] H. Nakatsuji. "Equation for the Direct Determination of the Density Matrix". In: *Phys. Rev. A* 14.1 (July 1976), p. 41. DOI: 10.1103/PhysRevA.14.41.

[250] C. Valdemoro et al. "The contracted Schrödinger equation methodology: study of the third-order correlation effects". In: *Theor. Chem. Account.* 118.3 (Sept. 2007), p. 503. ISSN: 1432-2234. DOI: 10.1007/s00214-007-0337-z.

[251] D. A. Mazziotti. "Anti-Hermitian Contracted Schrödinger Equation: Direct Determination of the Two-Electron Reduced Density Matrices of Many-Electron Molecules". In: *Phys. Rev. Lett.* 97.14 (2006), p. 143002. ISSN: 0031-9007. DOI: 10.1103/physrevlett.97.143002.

[252] J. W. Snyder and D. A. Mazziotti. "Photoexcited conversion of gauche-1,3-butadiene to bicyclobutane via a conical intersection: Energies and reduced density matrices from the anti-Hermitian contracted Schrödinger equation". In: *J. Chem. Phys.* 135.2 (2011), p. 024107. ISSN: 0021-9606. DOI: 10.1063/1.3606466.

[253] G. Gidofalvi and D. A. Mazziotti. "Direct calculation of excited-state electronic energies and two-electron reduced density matrices from the anti-Hermitian contracted Schrödinger equation". In: *Phys. Rev. A* 80.2 (2009), p. 022507. ISSN: 1050-2947. DOI: 10.1103/physreva.80.022507.

[254] D. R. Alcoba et al. "Optimized Solution Procedure of the G-Particle-Hole Hypervirial Equation for Multiplets: Application to Doublet and Triplet States". In: *J. Phys. Chem. A* 115.12 (2011), p. 2599. ISSN: 1089-5639. DOI: 10.1021/jp109018t.

[255] J.-N. Boyn and D. A. Mazziotti. "Accurate singlet–triplet gaps in biradicals via the spin averaged anti-Hermitian contracted Schrödinger equation". In: *J. Chem. Phys.* 154.13 (2021), p. 134103. ISSN: 0021-9606. DOI: 10.1063/5.0045007.

[256] D. A. Mazziotti. "Contracted Schrödinger Equation". In: *Reduced-Density-Matrix Mechanics: With Application to Many-Electron Atoms and Molecules*. John Wiley & Sons, Ltd, 2007. Chap. 8, pp. 165–203. ISBN: 9780470106600. DOI: https://doi.org/10.1002/9780470106600.ch8.

[257] D. A. Mazziotti. "Two-Electron Reduced Density Matrix as the Basic Variable in Many-Electron Quantum Chemistry and Physics". In: *Chem. Rev.* 112.1 (Jan. 2012), pp. 244–262. ISSN: 0009-2665. DOI: 10.1021/cr2000493.

[258] J.-N. Boyn et al. "Quantum-classical hybrid algorithm for the simulation of all-electron correlation". In: *J. Chem. Phys.* 155.24 (2021), p. 244106. ISSN: 0021-9606. DOI: 10.1063/5.0074842.

[259] Scott E. Smart, J.-N. Boyn, and D. A. Mazziotti. "Resolving correlated states of benzyne with an error-mitigated contracted quantum eigensolver". In: *Phys. Rev. A* 105.2 (2022), p. 022405. ISSN: 2469-9926. DOI: 10.1103/physreva.105.022405.

[260] Scott E. Smart and D. A. Mazziotti. "Many-fermion simulation from the contracted quantum eigensolver without fermionic encoding of the wave function". In: *Phys. Rev. A* 105.6 (2022), p. 062424. ISSN: 2469-9926. DOI: 10.1103/physreva.105.062424.

[261] Y. Wang and D. A. Mazziotti. "Electronic excited states from a variance-based contracted quantum eigensolver". In: *Phys. Rev. A* 108.2 (2023), p. 022814. ISSN: 2469-9926. DOI: 10.1103/physreva.108.022814.

[262] Y. Wang, L. M. Smith, and D. A. Mazziotti. "Quantum simulation of bosons with the contracted quantum eigensolver". In: *New J. Phys.* 25.10 (2023), p. 103005.

[263] I. G. Lang and Y. A. Firsov. "Kinetic Theory of Semiconductors with Low Mobility". In: *Sov. Phys. JETP* 16 (Jan. 1963), p. 1301.

[264] J. Schrieffer and P. Wolff. "Relation between the Anderson and Kondo Hamiltonians". In: *Phys. Rev.* 149 (2 Sept. 1966), p. 491. DOI: 10.1103/PhysRev.149.491.

[265] Z. Hu, R. Xia, and S. Kais. "A quantum algorithm for evolving open quantum dynamics on quantum computing devices". In: *Sci. Rep.* 10.1 (Feb. 2020), p. 3301. ISSN: 2045-2322. DOI: 10.1038/s41598-020-60321-x.

[266] Y. Wang et al. "Simulating Open Quantum System Dynamics on NISQ Computers with Generalized Quantum Master Equations". In: *J. Chem. Theory Comput.* 19.15 (2023), p. 4851. DOI: 10.1021/acs.jctc.3c00316.

[267] M. Motta et al. "Determining eigenstates and thermal states on a quantum computer using quantum imaginary time evolution". In: *Nat. Phys.* 16.2 (Feb. 2020), p. 205. ISSN: 1745-2481. DOI: 10.1038/s41567-019-0704-4.

[268] S. McArdle et al. "Variational ansatz-based quantum simulation of imaginary time evolution". In: *npj Quantum Inf.* 5.1 (Sept. 2019), p. 75. ISSN: 2056-6387. DOI: 10.1038/s41534-019-0187-2.

[269] E. Jaynes and F. Cummings. "Comparison of quantum and semiclassical radiation theories with application to the beam maser". In: *Proceedings of the IEEE* 51.1 (1963), p. 89. DOI: 10.1109/PROC.1963.1664.

[270] M. Blaha et al. "Beyond the Tavis-Cummings model: Revisiting cavity QED with ensembles of quantum emitters". In: *Phys. Rev. A* 105 (1 Jan. 2022), p. 013719. DOI: 10.1103/PhysRevA.105.013719.

[271] O. Castaños et al. "Analytic approximation of the Tavis-Cummings ground state via projected states". In: *Phys. Scr.* 80.5 (Oct. 2009), p. 055401. DOI: 10.1088/0031-8949/80/05/055401.

[272] T. Gera and K. Sebastian. "Effects of disorder on polaritonic and dark states in a cavity using the disordered Tavis–Cummings model". In: *J. Chem. Phys.* 156.19 (May 2022), p. 194304. ISSN: 0021-9606. DOI: 10.1063/5.0086027.

[273] D. De Bernardis et al. "Magnetic-field-induced cavity protection for intersubband polaritons". In: *Phys. Rev. B* 106 (22 Dec. 2022), p. 224206. DOI: 10.1103/PhysRevB.106.224206.

[274] Y. Todorov and C. Sirtori. "Intersubband polaritons in the electrical dipole gauge". In: *Phys. Rev. B* 85 (4 Jan. 2012), p. 045304. DOI: 10.1103/PhysRevB.85.045304.

[275] A. Köhn and A. Tajti. "Can Coupled-Cluster Theory Treat Conical Intersections?" In: *J. Chem. Phys.* 127.4 (July 2007), p. 044105. ISSN: 0021-9606. DOI: 10.1063/1.2755681.

[276] C. L. Benavides-Riveros et al. "Quantum simulation of excited states from parallel contracted quantum eigensolvers". In: *New J. Phys.* 26.3 (Mar. 2024), p. 033020. DOI: 10.1088/1367-2630/ad2d1d.

[277] J. Fregoni, F. J. Garcia-Vidal, and J. Feist. "Theoretical Challenges in Polaritonic Chemistry". In: *ACS Photonics* 9.4 (2022), p. 1096. DOI: 10.1021/acsphotonics.1c01749.

[278] T. Schwartz et al. "Reversible Switching of Ultrastrong Light-Molecule Coupling". In: *Phys. Rev. Lett.* 106 (19 May 2011), p. 196405. DOI: 10.1103/PhysRevLett.106.196405.

[279] M. Kowalewski, K. Bennett, and S. Mukamel. "Cavity Femtochemistry: Manipulating Nonadiabatic Dynamics at Avoided Crossings". In: *J. Phys. Chem. Lett.* 7.11 (2016), p. 2050. DOI: 10.1021/acs.jpclett.6b00864.

[280] A. Berghuis et al. "Enhanced Delayed Fluorescence in Tetracene Crystals by Strong Light-Matter Coupling". In: *Adv. Funct. Mater.* 29.36 (2019), p. 1901317. DOI: https://doi.org/10.1002/adfm.201901317.

[281] L. Mauro et al. "Charge-transfer chemical reactions in nanofluidic Fabry-Pérot cavities". In: *Phys. Rev. B* 103 (16 Apr. 2021), p. 165412. DOI: 10.1103/PhysRevB.103.165412.

[282] A. Mandal and P. Huo. "Investigating New Reactivities Enabled by Polariton Photochemistry". In: *J. Phys. Chem. Lett.* 10.18 (2019), p. 5519. DOI: 10.1021/acs.jpclett.9b01599.

[283] P. Forn-Díaz et al. "Ultrastrong coupling regimes of light-matter interaction". In: *Rev. Mod. Phys.* 91 (2 June 2019), p. 025005. DOI: 10.1103/RevModPhys.91.025005.

[284] S. Beltrán-Romero et al. "Cavity-induced switching between Bell-state textures in a quantum dot". In: *Phys. Rev. B* 108 (19 Nov. 2023), p. 195409. DOI: 10.1103/PhysRevB.108.195409.

[285] F. Schlawin, D. Kennes, and M. Sentef. "Cavity quantum materials". In: *Appl. Phys. Rev.* 9.1 (Feb. 2022), p. 011312. ISSN: 1931-9401. DOI: 10.1063/5.0083825.

[286] F. Buchholz et al. "Light–Matter Hybrid-Orbital-Based First-Principles Methods: The Influence of Polariton Statistics". In: *J. Chem. Theory Comput.* 16.9 (Sept. 2020), p. 5601. ISSN: 1549-9618. DOI: 10.1021/acs.jctc.0c00469.

[287] S. Warren et al. "Exact Ansatz of Fermion-Boson Systems for a Quantum Device". In: *Phys. Rev. Lett.* 133 (8 Aug. 2024), p. 080202. DOI: 10.1103/PhysRevLett.133.080202.

[288] J. Cobos et al. "Noise-Aware Variational Eigensolvers: A Dissipative Route for Lattice Gauge Theories". In: *PRX Quantum* 5 (3 Aug. 2024), p. 030340. DOI: 10.1103/PRXQuantum.5.030340.

[289] P. Mukhopadhyay, T. Stetina, and N. Wiebe. "Quantum Simulation of the First-Quantized Pauli-Fierz Hamiltonian". In: *PRX Quantum* 5 (1 Mar. 2024), p. 010345. DOI: 10.1103/PRXQuantum.5.010345.

[290] T. Haugland et al. "Intermolecular Interactions in Optical Cavities: An Ab Initio QED Study". In: *J. Chem. Phys.* 154.9 (Mar. 2021), p. 094113. ISSN: 0021-9606. DOI: 10.1063/5.0039256.

[291] V. Verteletskyi, T. Yen, and A. F. Izmaylov. "Measurement Optimization in the Variational Quantum Eigensolver Using a Minimum Clique Cover". In: *J. Chem. Phys.* 152.12 (Mar. 2020), p. 124114. ISSN: 0021-9606. DOI: 10.1063/1.5141458.

[292] H. R. Grimsley et al. "An adaptive variational algorithm for exact molecular simulations on a quantum computer". In: *Nat. Comm.* 10.1 (July 2019), p. 3007. ISSN: 2041-1723. DOI: 10.1038/s41467-019-10988-2.

[293] P. Anastasiou et al. "TETRIS-ADAPT-VQE: An adaptive algorithm that yields shallower, denser circuit Ansätze". In: *Phys. Rev. Res.* 6 (1 Mar. 2024), p. 013254. DOI: 10.1103/PhysRevResearch.6.013254.

[294] Yuchen Wang, Irma Avdic, and David A Mazziotti. "Shadow Ansatz for the Many-Fermion Wave Function in Scalable Molecular Simulations on Quantum Computing Devices". In: *arXiv* (2024). DOI: 10.48550/arxiv.2408.11026. eprint: 2408.11026.

[295] G. Harsha, T. Shiozaki, and G. Scuseria. "On the Difference between Variational and Unitary Coupled Cluster Theories". In: *J. Chem. Phys.* 148.4 (Jan. 2018), p. 044107. ISSN: 0021-9606. DOI: 10.1063/1.5011033.

[296] K. Jankowski and J. Paldus. "Applicability of Coupled-Pair Theories to Quasidegenerate Electronic States: A Model Study". In: *Int. J. Quantum Chem.* 18.5 (1980), p. 1243. ISSN: 1097-461X. DOI: 10.1002/qua.560180511.

[297] J. Paldus et al. "Application of Hilbert-space coupled-cluster theory to simple $(H_2)_2$ model systems: Planar models". In: *Phys. Rev. A* 47.4 (Apr. 1993), p. 2738. DOI: 10.1103/PhysRevA.47.2738.

[298] A. Marie, F. Kossoski, and P.-F. Loos. "Variational Coupled Cluster for Ground and Excited States". In: *J. Chem. Phys.* 155.10 (Sept. 2021), p. 104105. ISSN: 0021-9606. DOI: 10.1063/5.0060698.

[299] J. Robinson and P. Knowles. "Benchmark Quasi-Variational Coupled Cluster Calculations of Multiple Bond Breaking". In: *J. Chem. Theory Comput.* 8.8 (Aug. 2012), p. 2653. ISSN: 1549-9618. DOI: 10.1021/ct300416b.

[300] A. Javadi-Abhari et al. *Quantum computing with Qiskit*. 2024. DOI: 10.48550/arXiv.2405.08810. arXiv: 2405.08810 [quant-ph].

[301] E. Fischer and P. Saalfrank. "Cavity-Induced Non-Adiabatic Dynamics and Spectroscopy of Molecular Rovibrational Polaritons Studied by Multi-Mode Quantum Models". In: *J. Chem. Phys.* 157.3 (July 2022), p. 034305. ISSN: 0021-9606. DOI: 10.1063/5.0098006.

[302] Y. Wang and D. A. Mazziotti. "Quantum simulation of conical intersections". In: *Phys. Chem. Chem. Phys.* 26 (15 2024), p. 11491. DOI: 10.1039/D4CP00391H.

[303] P. Demekhin and L. Cederbaum. "Light-Induced Conical Intersections in Polyatomic Molecules: General Theory, Strategies of Exploitation, and Application". In: *J. Chem. Phys.* 139.15 (Oct. 2013), p. 154314. ISSN: 0021. DOI: 10.1063/1.4826172.

[304] C. Fábri, G. Halász, and Á. Vibók. "Probing Light-Induced Conical Intersections by Monitoring Multidimensional Polaritonic Surfaces". In: *J. Phys. Chem. Lett.* 13.5 (Feb. 2022), p. 1172. DOI: 10.1021/acs.jpclett.1c03465.

[305] J. Flick, N. Rivera, and P. Narang. "Strong light-matter coupling in quantum chemistry and quantum photonics". In: *Nanophotonics* 7.9 (2018), p. 1479. DOI: doi:10.1515/nanoph-2018-0067.

[306] E. Cortés et al. "Challenges in Plasmonic Catalysis". In: *ACS Nano* 14.12 (Dec. 2020), p. 16202. ISSN: 1936-0851. DOI: 10.1021/acsnano.0c08773.

[307] A. Recati and S. Stringari. "Supersolidity in ultracold dipolar gases". In: *Nat. Rev. Phys.* 5.12 (Dec. 2023), p. 735. ISSN: 2522-5820. DOI: 10.1038/s42254-023-00648-2.